TUM School of Engineering and Design
Technische Universität München

Numerical Investigation of Dynamic Stall on a Retreating Helicopter Blade

Yin Ruan

Vollständiger Abdruck der von der TUM School of Engineering and Design der Technischen Universität München zur Erlangung eines

Doktors der Ingenieurwissenschaften (Dr.-Ing.)

genehmigten Dissertation.

Vorsitzende(r):
Prof. Dr. mont. habil. Dr. h. c. Ewald Werner

Prüfer der Dissertation:
1. Prof. Dr.-Ing. Manfred Hajek
2. apl. Prof. Dr.-Ing. Christian W. M. Breitsamter

Die Dissertation wurde am 02.12.2021 bei der Technischen Universität München eingereicht und durch die TUM School of Engineering and Design am 03.03.2022 angenommen.

Contents

Nomenclature and Acronyms

α	Angle of attack, $^\circ$
$\dot{\alpha}$, $\ddot{\alpha}$	The rate change of angle of attack, and the second order of time derivative of angle of attack respectively, $\dot{\alpha} = \mathrm{d}\alpha/\mathrm{d}t$ and $\ddot{\alpha} = \mathrm{d}^2\alpha/\mathrm{d}t^2$
α_{mean}, α_0	An airfoil's mean value of angle of attack in a harmonic pitching motion, $^\circ$
α_{amp}	An airfoil's amplitude of angle of attack in a harmonic pitching motion, $^\circ$
α_{eff}, α_E	The effective angle of attack of an airfoil in a harmonic pitching motion, $^\circ$
α_i	The induced angle of attack, defined as the induced velocity over free stream velocity, $= U_i/U_\infty$
A	area of a control region, m^2
AR	Aspect ratio of a blade, defined as the ratio of radius square to the blade area, for rectangular platform, $AR = R/c$
a	Sonic speed, m/s
$a_{swell}*$	Non-dimensional acceleration of the swell structure
$\mathbf{a}$	Acceleration of a point, vector with components in x, y, z directions, m/s^2
$\mathbf{a}_s$	Acceleration of a point on surface wall, vector with components in x, y, z directions, m/s^2
${}^I\mathbf{a}$	Acceleration interpreted in the inertial coordinate system, vector with components in x, y, z directions, m/s^2
β	Compressibility correction coefficient, $= \sqrt{1 - M^2}$
C_c	Chord wise force coefficient of an airfoil or a blade section, defined as the ratio of sectional chord-wise force to the free-stream-based dynamic pressure and chord length, $= \frac{C_r}{0.5\rho U^2 c}$
c_{f_x}	The skin-friction coefficient in the chord-wise direction, defined as the ratio of skin shear stress to the free-stream-based dynamic pressure, $= \frac{\tau_w}{0.5\rho U^2}$
C_m, $C_{m,1/4}$	Moment coefficient of an airfoil or a blade section about its quarter chord, defined as the ratio of sectional moment to the freestream-based dynamic pressure and chord square, $= \frac{m}{0.5\rho U^2 c^2}$
C_{M_y}	Rotor pitching moment coefficient, defined as the ratio of half of the rotor's pitching moment to tip-velocity-based dynamic pressure, disk area and chord length, $= \frac{M_y}{\rho(\Omega R)^2(\pi R^2)c}$
C_{M_x}	Rotor rolling moment coefficient, defined as the ratio of half of the rotor's rolling moment to tip-velocity-based dynamic pressure, disk area and chord length, $= \frac{M_x}{rho(\Omega R)^2(\pi R^2)c}$
C_n	Normal force coefficient of an airfoil or a blade section, defined as the ratio of sectional normal force to the freestream-based dynamic pressure and chord length, $= \frac{N_r}{0.5\rho U^2 c}$

C_{n_α}	The slope of normal force coefficient of an airfoil with respect to angle of attack, $= \partial C_n / \partial \alpha$
C_n^I, C_n^c	Impulsive and circulatory part of normal force coefficient in lower-order aerodynamic models respectively
C_p	Pressure coefficient, defined as pressure over the freestream-based dynamic pressure and chord length, $= \frac{p-p_\infty}{0.5\rho U^2 c}$ $*$ for the hovering case, defined as pressure over the tip-speed-based dynamic pressure and chord length for the hovering case, $= \frac{p-p_\infty}{0.5\rho(\Omega R)^2 c}$
C_T	Thrust coefficient of a rotor, defined as the ratio of half of the thrust over tip-velocity-based dynamic pressure and disk area, $= \frac{T}{\rho(\Omega R)^2 \pi R^2}$
c	Chord length of the blade, m
f	frequency, Hz
f_s	Non-dimensional separation point based on Kirchhoff's theory
Γ	Circulation of a control region, defined as the counterclockwise line integral of the velocity over the boundary of the region or the area integral of the vorticity over the region, $= \oint_{\partial A} \vec{v} \cdot \mathrm{d}\vec{s}$ or $= \iint_A \omega_\perp \mathrm{d}A$, where $\omega_\perp$ is the vorticity perpendicular to the control area, m^2/s
Γ_{x+}	Circulation contributed by the vorticity in x direction with positive sign, $= \iint_A \omega_{x+} dA$, m^2/s
Γ_i	The circulation of a blade section in lower-order aerodynamic models, defined as the ratio of lift over air density and free-stream velocity, $= \frac{-L}{\rho V}$, m^2/s
H	Shape factor, defined as the momentum thickness over displacement thickness of the boundary layer for a two-dimensional flow.
H_{sep}	The critical value of shape factor, beyond which the flow is dominated by separation.
h	Placement of a blade section in z direction, m
η	Relaxatioin factor
η_γ	Stability effect factor of different components of $\partial\Gamma/\partial t$
θ	Pitch angle of a blade, $^\circ$
θ_0, θ_c, θ_s	Collective pitch angle, longitudinal cyclic pitch angle and lateral cyclic pitch angle respectively, $^\circ$
k	Reduced frequency, defined as the ratio of the time that a particle takes to pass half chord of an airfoil to the airfoil's oscillation period, $= \omega c/(2U)$
λ	Inflow ratio, defined as the ratio of the induced velocity over the blade tip velocity, $= u_i/(\Omega R)$
μ	(A rotor parameter) advance ratio, defined as the forward-flight velocity over blade tip speed, $= U_\infty/(\Omega R)$
$\mu^\dagger$	(A fluid parameter) viscosity of a fluid, $\mathrm{kg{\cdot}m^{-1} \cdot} s^{-1}$
M	Mach number, $= U/a$
M_∞	Free-stream Mach number, $= U_\infty/a$

Since it is very clear wether this symbol is used in a partial differential equation for aerodynamics or in an equation for flight dynamics, the conventional note for advance ratio and the viscosity is adopted without any modification and shall not arouse ambiguity.

ν	Molecular viscosity, $= \mu/\rho$, m^2/s
ρ	Density of the air, $\mathrm{kg{\cdot}m/s^2}$
R	Radius of a rotor, m
Re	Reynolds number, defined as the inertial force over viscous force, $= \frac{UL_{ref}}{\nu}$
Re_c	Chord-length-based Reynolds number, $= \frac{Uc}{\nu}$
r	Radial position on a blade, m
r/R	Non-dimensional radial position on a blade
$\mathscr{T}$	Airfoil type
t	Time, s
U, V	Velocity, m/s
U_∞, V_∞	Free-stream velocity, m/s
U_{tip}	Blade tip speed, m/s
$\mathbf{u}$	Velocity of a point in the fluid, vector with components in x, y, z directions, m/s
V_{ne}	Never exceed velocity of a flight envelope, m/s
$w_{3/4}$	Downwash at third quarter chord of an airfoil, m/s
$\bar{x}_{ac}$	An airfoil's non-dimensional position of aerodynamic center
x/c	Non-dimensional chord length
x_ξ	Weighted average position of the vorticity change rate field, $= \iint \dot{\omega} x \mathrm{d}S / \iint \dot{\omega} \mathrm{d}S$
Ψ, Ψ_b	Azimuth angle of a blade, $^\circ$
Ω	Rotational speed of a rotor, rad/s
ωt	Phase of a harmonic motion, rad
ω	Vorticity of a point in fluid, vector with components in x, y, z direction, $= \vec{\nabla} \times \mathrm{u}$, s^{-1}

2D, 3DR	2-dimensional, 3-dimensional and rotational
BEM	Blade element method
CAMRAD	Comprehensive analysis model of rotorcraft aerodynamics and dynamics
CFD	Computational fluid dynamics
CTC	Cycle to cycle
CSD	Computational structure dynamics
DDES	Delayed detached eddy simulation
DSV	Dynamic stall vortex
ILES	Implicit large eddy simulation
LE, LEV	Leading edge, leading edge vortex
NTSB	National transportation Safety Board (of USA)
PIV	Particle image velocimetry
SA-model	Spalart-Allmaras turbulence model
SI	Shock induced seperation
SST-model	Shear stress transport turbulence model
TE, TEV	Trailing edge, trailing edge vortex
URANS	Unsteady Reynolds average Naiver-Stokes
UTTAS	Utility Tactical Transport Aerial System

List of Figures

List of Tables

Acknowledgements

I would like to thank my supervisor, Prof. Dr. -Ing. Hajek, and the colleagues who are selflessly helping me whenever I encountered a problem in research or in life. To all my friends, family members and passersby, thanks for supporting me and companying me walking through the mists and shadows in my life. This research was funded by the China Scholarship Council and the chair of helicopter technology, TUM.

Abstract

Dynamic stall is a phenomenon on the retreating blade of a helicopter which can lead to excessive control loads or even result in safety issues. Research with numerical simulation and experiment on dynamic stall has been carried out mainly on pitching airfoils, and has helped people understanding the phenomena to a great extend. However, the research of dynamic stall on rotating blades is insufficient. The differences between the dynamic stall events on a rotating blade and on a pitching airfoil are yet to make clear, so is the mechanism behind them.

In order to elucidate the characteristic of dynamic stall on a rotating blade, and investigate the mechanism that results in these differences, I performed a numerical simulation of a single rotating blade with the NACA 0012 airfoil, 0 twist, and a rectangular platform. The collective and cyclic controls are estimated by an un-coupled simulation using CAMRAD II so that the incidence is large enough to trigger dynamic stall and in the mean time, the period-averaged longitudinal and lateral moment have the minimum absolute values. The numerical simulation was carried out with careful verifications of the grid strategy and the grid convergence. The main contents of the dissertation include:

1. The simulation result with Spalart-Allmaras turbulence model (SA model) is carefully examined in aspects of force coefficients, vortex structures, leading-edge/tip vortex interaction and separation locations.

2. The force coefficients and vortex structures at the quasi-symmetric plane of the dynamic stall vortex, at radial location $r/R = 0.898$ are compared with a 2D simulation that has the same pitching harmonics and reduced frequency.

3. The comparison of the simulation results with SA model and $k - \omega$ turbulence model are also presented, including the net thrust coefficient and rolling moment, sectional force coefficients, as well as the vortex cores on the blade at selected azimuth angles.

4. The vorticity transport analysis was for the first time implemented on the vortex system on the rotating blade and the 2d airfoil to clarify how rotation influences the vortex system.

5. The possible ways to improve lower-order models are proposed based on the numerical investigation.

The most important findings of the numerical investigation include:

1. The interaction of the leading edge vortex with the tip vortex dominates the post-stall stage. And a newly noticed outward moving swell structure, originating inboard is observed to have a great impact on the load in the post-stall stage.

2. Different from normal helicopter blades, the current case only shows separations starting from the leading edge.

3. The vorticity transport analysis shows that the Coriolis acceleration has a stabilisation effect throughout the dynamic stall process, and the combined effect of the span-wise convection and vorticity tilting is an "unstable" source before the occurrence of dynamic stall.

4. The Coriolis acceleration's stabilisation effect is due to the creation of a vorticity "sink" by appropriate distributions of span-wise velocity gradient in z direction; this mechanism suggests passive and active means of control method for dynamic stall on rotating blades.

1 Problem Statement

1.1 Dynamic Stall and Helicopters

SINCE the first controllable helicopter made its maiden flight, understanding and prediction of the unsteady aerodynamic loads on the rotor blade has been one of the important tasks in helicopter industry. Among these loads, the one that a blade in the 3rd quadrant experiences, can cause severe increase in blade control link load, torsional stresses as well as oscillatory torsional loading due to dynamic stall, all of which can greatly reduce the fatigue life of rotor mechanical components. An example of such control link load surge can be seen in the manoeuvre flight of UH-60A [1], when in order to avoid terrain obstacles doing UTTAS (Utility Tactical Transport Aerial System) pull-up (the vehicle starting from maximum level flight speed, starts to nose pitch up with 1.75g normal acceleration for 2.5s, and lose minimum airspeed), the blade pitch rate can reach up-to 14.7 deg/sec and the dynamic stall occurring on the blade for several revolutions results in more than twice the pitch link load of a level flight.

This phenomenon, dynamic stall can also result in flight accident if not properly handled. On a Friday in December 1998, a pilot encountered retreating blade stall while flying Bell 47G2 at 100 mph in Helendale, CA [2]. The shaking of the helicopter was reported as an unbalanced washing machine. The rpm began to decay and when the pilot reduced the power and stabilised the air speed to around 60 mph, the shaking stopped. He further reported that the lift was unable to maintain and hence it entered an autorotation over a hilly terrain. The National transportation Safety Board (NTSB) determined the cause of the accident to be exceeding of the V_{ne}(never exceeding velocity) for the Bell 47G2 helicopter, 100 mph, following by inappropriate procedure to recover from main rotor retreating blade stall. This V_{ne} for a specific helicopter represents the important role that dynamic stall plays, and indicates the barrier in the route of seeking faster flying helicopters.

Yet this phenomenon is till now not well thorough understood due to its complexity in the onset mechanism and the three dimensional features of the flow field. Semi-empirical models, such as Beddose-Leishman model [3], ONERA mode [4] and other thereupon-based revised models [5–9], were established, demonstrated through 2d airfoil experiment results and implemented on full-rotor environment (e.g. CAMRAD II [10]) to trim and predict loads. The Research [11] that compared the simulation result in full-rotor environment and flight data, concluded that Beddose-Leishman, ONERA BH, ONERA Edlin, Johnson, Boeing models can predict the stall locations fairly well, yet all unable to yield the correct magnitude of pitching moment peaks during dynamic stall. A recent research from ONERA [12] also showed discrepancy of model predicted loads from the experiment data, despite the well predicted azimuth angles, at which stall

Figure 1.1: Illustration of the movement of a blade section (highlighted in blue) on a forward-flying NH-90 Sea Lion helicopter. [13]

occurs. The imprecision of the models manifest that there is still a distance to go before we comprehend the phenomenon on the retreating blade of a helicopter.

1.2 Dynamic Stall: the phenomenon

THE optimum operation condition of an airfoil profile is that the flow passes around it smoothly, and there is no separation at any position. When the flow is observed with smoke streaks, the streak-represented stream lines should pass the airfoil smoothly, without any disturbance or deflection over the upper surface of the airfoil. Usually the lift produced by the airfoil increases linearly with the angle of attack. But this rule does not hold when the flow begins to separate. At a certain value, when the flow shows separation over a large portion of the upper region of the airfoil, or the stream lines deflect and become discontinuous to a great extend in this region, the lift produced by the airfoil drops dramatically. The stall takes place.

Dynamic stall is the stall event that takes place on a periodically pitching airfoil. When a helicopter enters its forward flight, the asymmetric flow conditions on the forward side and retreating side require that cyclic controls should be implemented to maintain an equilibrium state of a helicopter: hence the blade is pitching down in the forward regime and pitching up in the retreating half revolution. And due to the ability of flap – either around a hinge or by bending with elasticity of the blade, the tip moves up and down in every revolution, as shown in Figure 1.1. The motion makes the stall event on the blade significantly different from the one that occurs on a stationary airfoil or wing.

1.2.1 Dynamic Stall of a pitching airfoil

Dynamic stall on an oscillating blade section is pretty well understood with the help of experiments and discussions in early years [15–26]. Not all the early literature is listed above, since it was then a heated topic and various of experiments, joint-research were conducted, and some of the contents were repetitive. This literature was reviewed profoundly by McCroskey [27] and Carr [28]. In Figure 1.2, **(a)** shows a typical force

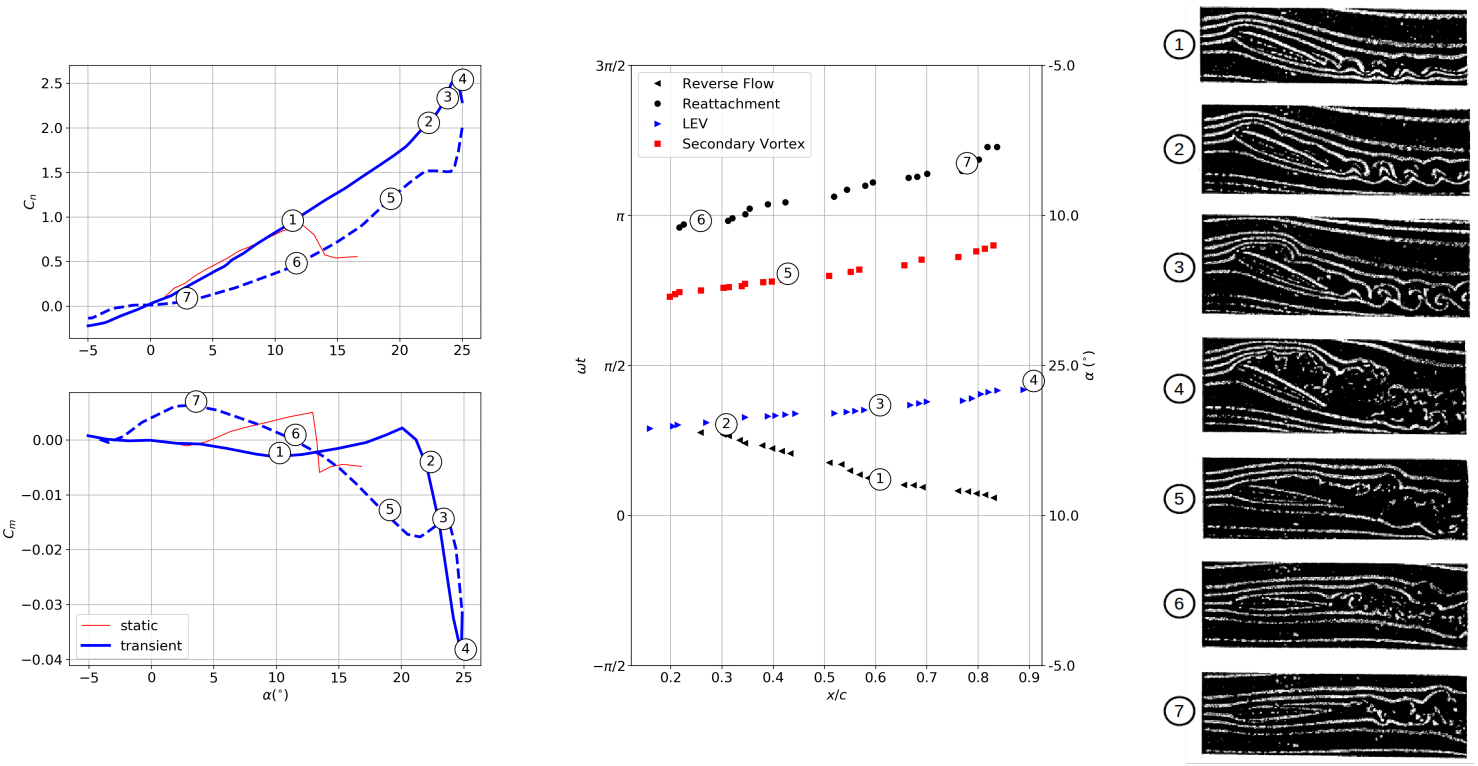

(a) **(b)** **(c)**

Figure 1.2: Dynamic stall on a pitching NACA 0012 airfoil, reproduced with the permission by Gerontakos [14].**(a)** Dynamic loads of the oscillating NACA 0012 airfoil, $\alpha(t) = 10^\circ + 15^\circ \sin(\omega t)$, reduced frequency $k = 0.1$. **(b)** Dynamic stall associated boundary layer events: flow reversal, reattachment, LEV and secondary vortex positions with respect to the phase ωt. **(c)** Smoke flow visualisation pictures of selected phases: prior to, during and post stall.

hysteresis of a pitching NACA 0012 airfoil at low Mach number ($M < 0.1$) with the pitching scenario $\alpha(t) = 10° + 15° \sin(\omega t)$. Here the reduced frequency $k = \omega_s c/(2U_\infty) = 0.1$, where U_∞ is the free-stream velocity and c is the chord length of the airfoil. **(b)** shows the boundary layer events come along with the motion and **(c)** shows the smoke flow visualisation of selected phases. The events indicated by the numbers are consistent in three subplots. The dynamic stall process can be categorised into 4 main stages:

(1) **"Overshoot" of the normal force coefficient.** The airfoil pitches up and the angle of attack exceeds that of the static stall angle, the flow is still attached and the separation point is at around $x/c = 0.6$ as shown in (1).

(2) **Stall onset.** The break down of leading edge separation bubbled arouses the growing of a leading edge vortex(LEV). In this phase, the normal force coefficient continues to grow with a slightly larger $C_{n\alpha}(\partial C_n/\partial\alpha)$, while the moment coefficient begins to drop, as shown in (2). As the pitch angle increases further, the LEV grows larger and the minimum pressure on the upper surface of the airfoil moves aftwards, as shown in (3).

(3) **Detachment of dynamic stall vortex.** At a certain pitch angle, the LEV is shed from the leading-edge and the flow over the upper surface becomes completely separated, as shown in (4). Then the C_n decreases and C_m recovers. In this phase after the pitch angle enters its decreasing scenario, a secondary or even tertiary LEV manifests itself on the upper surface, resulting the fluctuation of C_n and C_m, similar to consequence of the first LEV, as the vortex transported downstream, as shown in (5).

(4) **Re-attachment of flow.** The pitch angle continues to decrease and at a certain point the flow begins to reattach, as shown in (6). And after a while, the flow becomes totally attached to the upper surface of the airfoil.

The mechanism of the primary dynamic stall vortex(DSV) formation and detachment was first reviewed by Reynolds et al. [29], and was comprehensively reviewed later by Doligalski et al. [30]. Reynolds et al. [29] used potential theory and vortex/image theory to explain this phenomenon. They pointed out the vorticity is accumulated at the leading edge of a pitching airfoil due to the high adverse pressure gradient, and it is strong enough with an vortex/image system to resist the external free stream, hence attached and even moving upstream on the airfoil. And the detachment of the vortex is explained as a result of the break of the balance between the outer flow forces and the inner viscous effect. Based on more experiment observations [31–36], Doligalski et al. [30] categorised the **eruption of the dynamic stall vortex** (during the previously mentioned stages (2) and (3)) into 4 main stages:

(a) **Recirculation and eruption.** An sharp adverse pressure gradient region appears on the leading edge of a pitching airfoil. At high Re_c a "spike-like" boundary layer response consequently leads to a narrow-band eruption of the surface layer. A thin plume containing significant levels of vorticity leaves the surface rapidly. This

process is also described by other researchers as "**the bursting of a leading edge separation bubble**".

(b) **Primary vortex rollup.** This eruption of the plume moves farther away and forms the primary dynamic stall vortex.

(c) **Vortex-induced eruption and viscous-inviscid interaction.** This departing primary vortex induced a surface separation, or a second plume of eddy. The consequent viscous-inviscid interaction provokes the ejection of vorticity into the main stream. This process is believed to cut off the primary vortex from its the source of vorticity.

(d) **Wrap-up and Detachment** Finally the erupted plume wraps around the primary stall vortex and quickly detaches from the surface.

This phenomenon is dependent on aerodynamic parameters (compressibility effect as a consequence of free-stream Mach number M_∞, Reynolds number Re, airfoil shape $\mathscr{T}_{Airfoil}$) and the motion parameters (average angle of attack α_{mean}, reduced frequency k, pitching amplitude α_{amp}). We can express the force coefficients curves of the pitching airfoil C_x (representing either normal force coefficient C_n, moment coefficient C_m or chord-wise force coefficient C_c) as:

$$C_x = \mathfrak{F}(\mathscr{T}_{Airfoil}, k, \alpha_{mean}, \alpha_{amp}, M_\infty, Re). \tag{1.1}$$

Dependent on the maximum incidence angle $\alpha_{\max}$, oscillating airfoils can be categorised into four regimes, namely no stall, stall onset, light stall and deep stall. The light stall of an oscillating airfoil is characterised by a relatively small scale of the vertical viscous zone, which is on the order of the airfoil thickness, and the scale is generally less than the static stall. The stall behaviour is closely related to the boundary layer separation characteristics, namely leading edge separation, trailing edge separation. This type of stall is very sensitive to $\mathscr{T}_{Airfoil}$, M_∞, k, α_{mean} and α_{amp}. While deep stall is characterised by a relatively larger viscous zone, which is on the order of the airfoil chord, and manifests the passage of vortex structures on the upper surface of the airfoil. Figure 1.2 is a typical example of a deep stall case, since the smoke flow visualisation show a large viscous zone.

$\mathscr{T}_{Airfoil}$ is the parameter that refer to either different airfoil profiles, (e.g. NACA 0012, NLR-1, Sikorsky SC-1095, etc.) or any modification of the leading edge of a typical airfoil profile. McCroskey [15] figured out that with moderated sharp leading edge, the airfoil tends to stall with an abrupt leading-edge separation, contrary to the other blunt-nose airfoils, which tend to experience a gradual, trailing-edge-separation aroused stall. And it has a relatively stronger influence on the light stall cases than the deep stall cases [16], since deep stall cases are dominant by the large vortex passage.

Reduced frequency k represents the ratio of flow transportation time $(c/2)/U_\infty$ to the oscillation period measurement $1/\omega_s$, with the former term representing the time needed for the convection through half of the airfoil chord. Extending Sommerfeld's statement of conservation of vorticity [37], Wu [38] suggested that half of the solid angular velocity

$\omega = \Omega_s/2$ can be treated indistinguishable from the vorticity of the fluid, or in other words, the rotating body in fluids is another source of vorticity besides the viscous boundary shear layer. As a result, the increase of k means a stronger leading edge vortex, hence a larger $C_{n,\max}$, no matter a light stall or a deep stall. However, for airfoils with sharp leading edge (e.g. VR-7 airfoil, typical of leading edge separation in light stall), the increase of k results in a lighter moment stall, while for airfoils with blunt-nose (e.g. NACA 0012 airfoil, typical of trailing edge stall in light stall), the increase of k results in a stronger moment stall [27]. For both types of airfoils in deep stall, since the vortex passage dominates the process, the larger k means a stronger and larger leading edge vortex, and hence a stronger moment stall. This parameter determines also the time when the leading edge vortex begins to shed, for example, a critical k_{cr} may exist for a certain type of airfoil pitching with a certain amplitude α_1 and a mean incidence α_0, beyond which, the leading edge vortex only detaches in the down-ward pitching phase.

α_{mean} and α_{amp} determine the $\alpha_{\max}$, hence they determine whether the stall process is a light stall or a deep stall. On the other hand, if together with k, the combinations selected that has a similar $\alpha(t)$ history of a cycle for some portion where $\alpha(t)$ is larger than the static stall angle, show almost identical force coefficients hysteresis throughout the stall events [27]. This holds true for deep stall, [27] but current literature doesn't support the pitch rate analogy for light stall events.

The effect of compressibility M_∞ is reported by Patrick [39], with the wind tunnel experiments on a Bell helicopter airfoil (most likely Bell/Worthmann FX 69-H-098 Airfoil), to result in two different behaviours of dynamic stall. For $M_\infty \leq 0.4$, the leading edge separation is governed by an abrupt break down of the turbulence boundary layer, while for $M_\infty \geq 0.5$, the flow breaks down after the formation of a λ-shock over the airfoil, namely shock-induced stall. Within the lower-Mach range, the gestation period decreases as M_∞ increases, and the growth of stall vortex is cut-off due to the presence of supersonic flow as the incidence becomes larger. Within the higher-Mach-number range, multiple normal shocks form and coalesce into a stronger shock wave over a small spatial extend at the leading edge area, and the normal force travels downstream, growing in strength as $\alpha(t)$ increases, but not immediately followed by separation. In this Mach range, increasing k delays the shock-induced stall onset, as that of the incompressible flow. Early research [40, 41] noted that increasing M_∞ results in an earlier stall. Nevertheless Patrick stated that this is a static effect, since for the same k, the stall penetration, $\alpha_{ds} - \alpha_{ss}$, remains constant as M_∞ increases. Carr [42] mentioned the overshoot of force and pressure decreases as M_∞ increases, nonetheless Patrick found that the ratio $|\Delta C_p/C_{p,min}|$ increases with increasing M_∞. Patrick's experiment, together with the interferometric investigation [41], confirms that the shock-induced separation is more inline with a jet/gust of air than a concentrated vortex.

The effect of Reynoldsnumber $Re = U_\infty c/\nu$ is believed to be a weak factor at low Mach numbers, but its role is unclear for large Mach conditions [27, 40]. Since it is an important parameter that determines the transition of the flow, this may acts like a strip at the leading edge of the pitching airfoil. McAlister's experiment [17] shows that for pitching NACA 0012 airfoil with strip's:

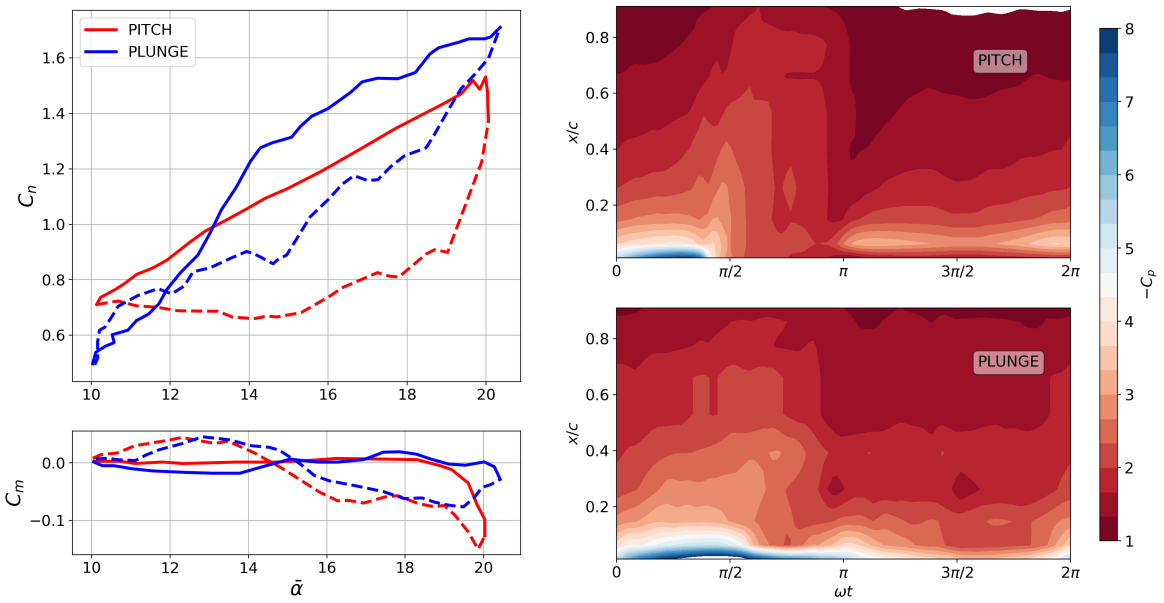

Figure 1.3: Comparison of Dynamic Stall event on an airfoil that plunges with the equivalent pitching motion, reproduced from Carta [44].**(a)** Dynamic loads of the oscillating Sikorsky SC1095 airfoil with a mean angle of attack $\alpha_{mean} = 15°$, subject to a free stream $U_\infty = 30.5$m/s. Plunge equivalent pitching amplitude $\bar{\alpha}_{amp} = 5.02°$, frequency f, cps(cycle per second)$= 8.31$, reduced frequency $k = 0.131$. Pitching amplitude $\alpha_{amp} = 5°$, frequency $f, cps = 8.31$, reduced frequency $k = 0.123$ **(b)** The corresponding pressure coefficients on the upper surface of the airfoil in plunge and pitch motion. The dashed lines represent downward pitching or upward heaving.

(1) The moment stall is sooner for all k;

(2) Its $C_{n,\max}$ is smaller when $k < 0.1$, and its $|C_{m,\min}|$ is smaller when $k < 0.05$;

(3) The phase when $C_{n,\max}$, $C_{m,\min}$ is reached is postponed for all k.

Gupta [43]showed that higher Reynolds ($Re = 1 \times 10^6$) have the same trend as the trip. However as summarised, the difference, comparing with that results from other factors, is small in low Mach range ($Ma \leq 0.1$), yet few research has done for higher Mach range.

1.2.2 Dynamic Stall of a plunging airfoil

On the other hand, the flap corresponded plunge-heave motion of the blade section can be analogous to the pitching case, using the concept of effective angle of attack α_{eff}. When the airfoil moves downwards, or plunges, with a velocity $-\dot{h}$, the effective angle of attack of the airfoil, subject to a free-stream velocity U_∞ with an angle of attack α_0, can be written as:

$$\alpha_{eff} = \alpha_0 + \arctan \frac{\dot{h}}{U_\infty}. \tag{1.2}$$

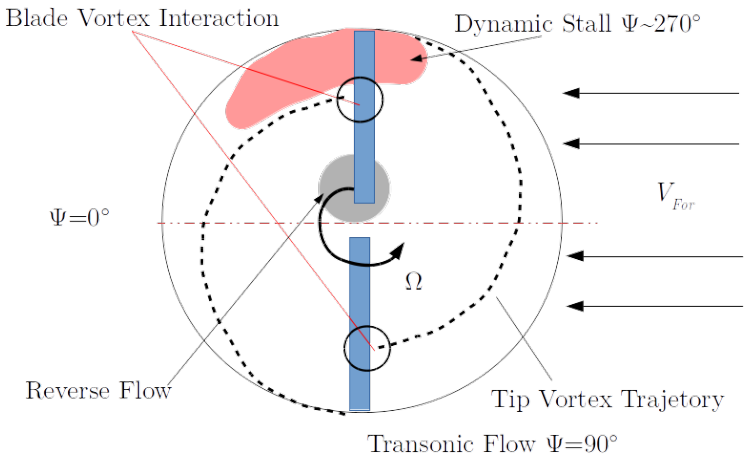

Figure 1.4: Schematic plot of the flow phenomena on a helicopter rotor

For small angles, arctan can be eliminated from the equation. However, plunge-heave motion is still different from its equivalent pitching motion. Figure 1.3 shows the force coefficients and pressure coefficients of an airfoil with plunge-heave motion and equivalent pitch motion. According to Carta [44], for the plunge case, there is no orderly downstream propagation of the stall vortex. Moreover, the slope of C_N of a plunge case shows a larger value comparing to the equivalent pitch case, while the shape and value of both C_N and C_M of a plunge case vary significantly depending on the equivalent pitch amplitude α_{amp} and the mean incidence angle α_{mean}. These differences are believed to be a result of major different mechanisms of the stall flow breakdown for plunge and pitch cases.

Some researchers explain that the difference is attributed to pitch-induced camber effect $\partial z/\partial x = (x_p - x)\dot{\alpha}\cos\alpha$, which varies along with the angular velocity [45, 46]. Or starting from the analogy of $\alpha(t)$ as is mentioned in previous section, the match of pitch rate $\dot{\alpha}(t)$ is also important for dynamic stall cases. By differentiating equation 1.2, the equivalent pitch rate:

$$\dot{\alpha}_{eff} = \frac{\ddot{h}/U_\infty}{1 + (\dot{h}/U_\infty)^2} \leq \frac{\ddot{h}}{U_\infty}. \tag{1.3}$$

This also explains why a huge difference exists. Since before the onset of dynamic stall, the effective pitching rate $\dot{\alpha}_{eff}(t)$ begins to deviate from the pitching case.

1.3 Dynamic Stall on helicopter blades: the three-dimensional effect

Dynamic Stall takes place in the fourth quadrant of the rotor revolution when the incidence angle increases. The flow condition of a rotor blade section is nevertheless more complex than what is shown in the previous section. Most importantly, the

varying free stream velocity and forces on a non-inertial coordinate system, namely the centrifugal force $F_{centrifugal}$ and the Coriolis force F_{Cor}. Using the azimuth definition shown in Figure 1.4, for the blade section at a non-dimensional radial location r/R, the free stream velocity in-plain with this airfoil is:

$$U_\infty = (r/R)\Omega R + \mu\Omega R \sin\Psi. \tag{1.4}$$

where μ is the advance ratio of a helicopter, defined as the ratio of forward flight speed to blade tip speed, $\mu = V_{Forward}/(\Omega R)$. It varies as the azimuth angle changes. In the mean time, for a trimmed helicopter with collective pitch θ_0, longitudinal cyclic control θ_c and lateral cyclic control θ_s, the incidence angle of the blade can be written as:

$$\theta(\Psi) = \theta_0 + \theta_1 \sin(\Psi + \varphi). \tag{1.5}$$

where $\theta_1 = \sqrt{\theta_s^2 + \theta_c^2}$, and $\varphi = \arctan(\theta_c/\theta_s)$. Hence the maximum incidence angle $\theta_{\max}$ and the maximum free stream flow $U_{\infty,\max}$ has a phase lag φ, and for a helicopter in forward flight, $\varphi \in [\pi,\ 3\pi/2]$. Gharali [47] did a numerical simulation and showed that for such phase lag, the C_n is smaller and the dynamic stall vortex(DSV) is relatively weaker. At the time when the dynamic stall vortex grows, the instant velocity $U(t)$ is smaller than the average flow velocity U_{mean}, which results in a shorter trailing edge shear layer and inhibits the growth of the leading edge vortex. As a result, the dynamic load overshoot on the pitching airfoil is smaller. Recent research [48] also confirms the trend of the C_n and C_m curves: their hysteresis shrink as the phase angle φ increases.

Another out-of-plane velocity component, perpendicular the blade section is:

$$U_r = \mu\Omega R \cos\Psi. \tag{1.6}$$

It is positive when the flow direction is towards the blade tip, and negative when towards the blade root. This component creates the well-known yawing effect, or sweep effect. St. Hilaire et al. [19] did experiment on a pitching swept wing, and find that sweep tends to delay the onset of dynamic stall and to reduce C_n, C_m's rate of change as stall begins. And the magnitude of the hysteresis loops are also reduced to some extend. However, experimental research hasn't touched the harmonic varying U_r. Wen [49] did numerical research concerning the "dynamic sweep" effect on a pitching blade section, and the implicit large eddy simulation (ILES) simulation indicated a weaker trailing edge vortex in the presence of yawing effect. And the dynamic vortex sheds with a higher frequency comparing to the baseline case. Similar to the in-plane varying free stream velocity, the phase difference of the dynamic sweep is also a key factor that influences the vortex field on the airfoil. Yet little research has covered this area.

Most importantly, fixing the coordinate on the blade section means the usage of a non-inertial coordinate system, hence the flow thereupon experiences the centrifugal force, which is pointing towards the blade tip; and because it's also a rotating system, the flow experiences the Coriolis force, $F_{Cor} = -\oint 2\rho(\vec{\Omega} \times \vec{U_r})d\mathscr{V}$, with a direction perpendicular to the stream velocity on the blade section. Note that this velocity is a summation of the chord-wise and radial-wise relative velocity. A natural question arises when comparing

the flow condition on a helicopter blade with that of an airfoil: **What role do these two factors play in the dynamic stall event of a retreating blade?**

A search on the dynamic stall events on a two-dimensional blade section with artificial centrifugal force term in the governing equation [49] can not address the full picture of the rotating characteristics. Indeed, any two-dimensional numerical investigation, or non-rotating experiment can hardly uncover the role played by these two forces. Neither does the investigation of the effect of the radial flow [50] on a rotating blade explain comprehensively, since radial flow itself is a consequence of the centrifugal force.

Moreover, as shown in Figure 1.4, the phenomena on a multiple-bladed rotor include also the interaction of the blade and the wake, especially the blade and the tip vortex of the previous blade. Other factors such as transonic flow/supersonic flow at advancing side near $\Psi = 90°$ and reverse flow in the root region at retreating side can also result in different kinds of dynamic stalls. Ref. [52, 53] show that vortex can also lead to leading edge separation on a pitching airfoil, and is also related to the leading edge separation on the succeeded rotating blade, the latter of which is rather a combination of blade vortex interaction (BVI) and the rotating effect. In order to answer the question raised above, we have to eliminate the possibility of BVI induced dynamic stall.

Modern helicopters that seek a high Figure of Merit require the twist of the blade, a high advance ratio require a special swept tip design. And excellent performance in multiple types of tasks requires combinations of airfoil profiles as well as plant forms. These abundant parameters entangle with the aforementioned varying free stream and forces in a non-inertial coordinate, which makes it even harder to answer the question stated above, let alone establish a full picture of dynamic stall on a helicopter rotor.

1.4 Modelling of dynamic stall on helicopter blades: Lower Order Models

ENGINEERING is an art of trade-off of accuracy and efficiency. This also true for rotorcrafts in their design process: the evaluation of considerable amount of design parameters through CFD simulations is impossible; even after the design is fixed, the searching for trim conditions with full coupling of computational fluid dynamics (CFD) and computational structure dynamics (CSD) is not efficient enough. As a result, the lower order models, both aerodynamic and dynamic models that have a reduced accuracy but a relatively high efficiency are adopted in engineering. We hence introduce the lower order aerodynamic models that are used to assess the loads on helicopter blades. The flow chart of an efficient and accurate aerodynamic model for comprehensive analysis is sketched in Figure 1.5. We do not distinguish here inflow model and wake model, since the inflow is usually influenced by the wake, and the term "wake model" is also a method to predict inflow field.

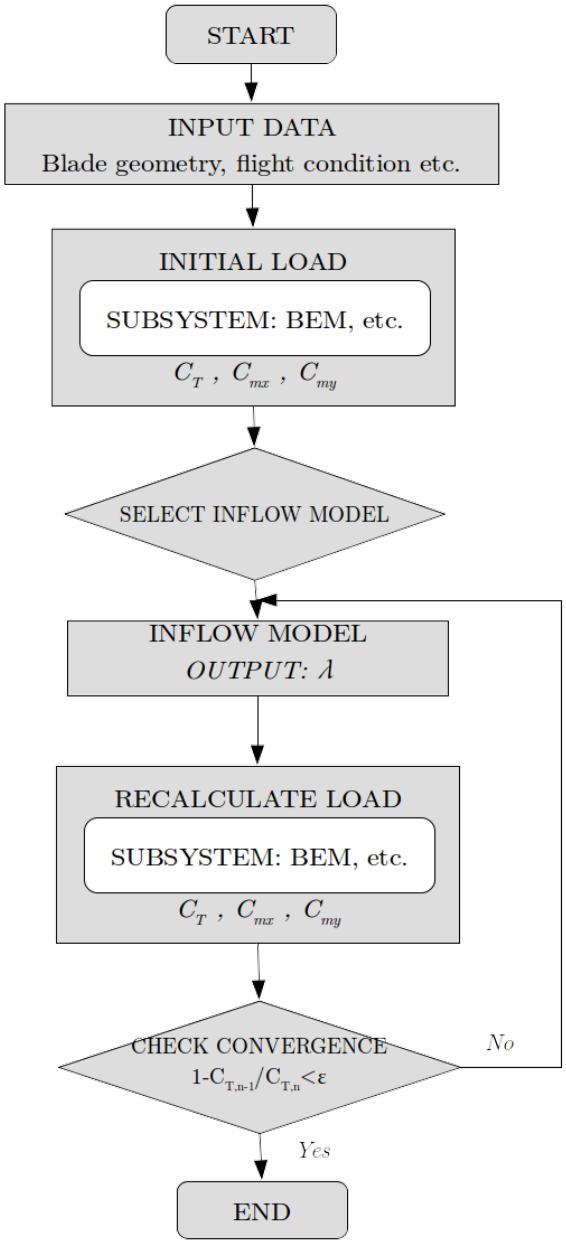

Figure 1.5: General flow chart of aerodynamic modelling for rotorcrafts.

1.4.1 Basic ideas for modelling aerodynamic loads on helicopter blades

Blade-Element Theory

The blade element theory (BET) approach, or blade element method(BEM), is based on the assumption that **each blade section acts as a two-dimensional airfoil to produce aerodynamic forces**, and various types of corrections, both theoretical and

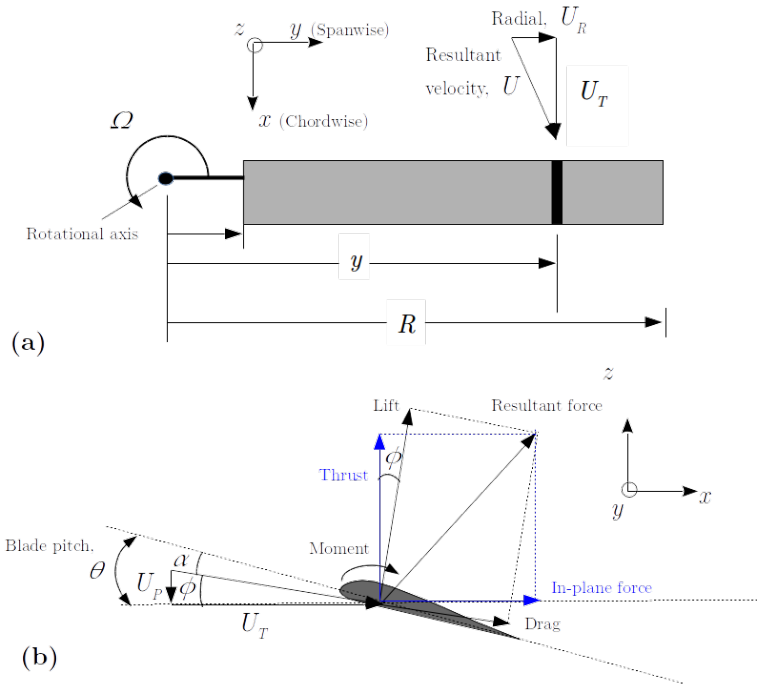

Figure 1.6: Aerodynamic environment at a typical blade element, **(a)**: Top view of the blade; **(b)** blade element level.

empirical, are used for three-dimensional effects [63]. As sketched in Figure 1.6, the influence of the rotor wake, the well-know finite aspect wing effect and other aerodynamic influences are assumed to be contained in an inflow angle ϕ, at a blade section. The induced flow from the rotor wake, blade motions (e.g. pitching, flapping, lead-lag), elastic bending, and torsional deformations, as well as from perturbations by air-frame components.

Induced velocity field

A primary aerodynamic problem in hovers and forward flights is to determine the nonuniform distribution of induced velocity, or the inflow over the rotor disk and its effect on the sectional air-loads. The inflow models including linear models [54], dynamic inflow model [55,56], prescribed wake model [57], free wake model [58] and more advanced wake models are reviewed in detail by Chen et.al. [59]. The simplest linear inflow models assume linear distributions of the form:

$$\lambda_i(r, \Psi_b) = \lambda_0(1 + k_x r \cos \Psi_b + k_y r \sin \Psi_b) \tag{1.7}$$

where λ_0 is the inflow at the center of the rotor as given by the momentum theory and where the weighting factor k_x and k_y represent a spatial distribution distortion of the inflow. The blade azimuth angle Ψ_b is defined as sketched in Figure 1.4, $\Psi_b = 0$ when the blade points downstream, and $\Psi_b = \pi/2$ on the advancing side.

1.4.2 Modelling of 2-dimensional dynamic stall

Unsteady aerodynamic modelling of attached flow considering compressibility and vary free-stream velocity

The modelling of unsteady aerodynamic forces on an airfoil begins as early as 1930s when Theodorsen [60] derived the expression of the force on a plate under arbitrary motions (free from separation) in frequency domain. And later Duhamel integral was introduced by Van der Wall et. al. [61] to express the circulatory change of the force due to the change of angle of attack, free stream velocity or other aerodynamic parameters in time domain. For an airfoil pitching at its 1/4 chord, the normal force coefficient, following Jones [62], can be expressed as:

$$\begin{aligned} C_n(t) &= C_n^c(t) + C_n^I(t) \\ &= \frac{2\pi}{V}\left[(V\alpha + \frac{\dot{\alpha}c}{2})(s=0)\phi_W(s) + \int_0^s \frac{\mathrm{d}(V\alpha + \dot{\alpha}c/2)}{\mathrm{d}\sigma}(\sigma)\phi_W(s-\sigma)\mathrm{d}\sigma\right] + \frac{\pi c}{2V^2}\left(\frac{\mathrm{d}(Vc)}{\mathrm{d}t} + \frac{\ddot{\alpha}c}{4}\right), \end{aligned} \tag{1.8}$$

where s is the distance traveled by the airfoil in semi-chords,

$$s = \frac{2}{c}\int_0^t V(t)\mathrm{d}t. \tag{1.9}$$

and $\phi_W(s)$ is the Wagner function, which is usually presented approximately, according to Jones [63] as a exponential series with 4 parameters:

$$\phi_W(s) = 1 - A_1 e^{-b_1 s} - A_2 e^{-b_2 s} \tag{1.10}$$

And the moment coefficient can be expressed as:

$$C_{m,1/4}(t) = C_n^c(t)(0.25 - \bar{x}_{ac}) - \frac{\pi}{8}(\frac{\dot{\alpha}c}{V}). \tag{1.11}$$

Jose et. al. [62] extended the model to compressible regime, considering a non-uniform free-stream velocity. The comparison of the model with CFD result showed a good agreement. The basic idea is also treat the normal force and moment to be composed of a circulatory part (the part which is associated with the circulation around the airfoil, or the effect of the wake, and is denoted as the superscript n) and the impulsive part (the part is associated with apparent mass effects, and is denoted as the superscript I). Using small perturbation theory, the normal force and moment at 1/4 chord can be modelled as:

$$\begin{aligned} C_n^c(t, M) = \frac{1}{V}\Big[&C_{n\alpha} w_{3/4}(\alpha_0, M_0, \dot{\alpha}_0)\phi_n^c(s, M) \\ &+ \int_0^s \left(\frac{\partial C_{n\alpha} w_{3/4}}{\partial \alpha}\frac{\mathrm{d}\alpha}{\mathrm{d}\sigma} + \frac{\partial C_{n\alpha} w_{3/4}}{\partial M}\frac{\mathrm{d}M}{\mathrm{d}\sigma} + \frac{\partial C_{n\alpha} w_{3/4}}{\partial \dot{\alpha}}\frac{\mathrm{d}\dot{\alpha}}{\mathrm{d}\sigma}\right)(\sigma)\phi_n^c(s-\sigma)\mathrm{d}\sigma\Big], \end{aligned} \tag{1.12}$$

$$
\begin{aligned}
C_n^I(t) = &\int_0^s \frac{4}{M}\frac{\mathrm{d}\alpha}{\mathrm{d}\sigma}(\sigma)\phi_{n,\alpha}^I(s-\sigma,M)\mathrm{d}\sigma \\
&+ \int_0^s \frac{4\alpha}{M^2}\frac{\mathrm{d}M}{\mathrm{d}\sigma}(\sigma)\phi_{n,M}^I(s-\sigma,M)\mathrm{d}\sigma \\
&+ \int_0^s \frac{c}{aM^2}\frac{\mathrm{d}\dot{\alpha}}{\mathrm{d}\sigma}(\sigma)\phi_{n,\dot{\alpha}}^I(s-\sigma,M)\mathrm{d}\sigma
\end{aligned} \tag{1.13}
$$

$$
\begin{aligned}
C_{m,1/4}^c(t,M) = &C_n^c(t,M)(0.25-\bar{x}_{ac}(M)) \\
&- \frac{1}{M}\left[\frac{\pi\dot{\alpha}_0 c/a}{8\beta_0}\phi_m^c(s,M) + \int_0^s \left(\frac{\pi c/a}{8\beta}\frac{\mathrm{d}\dot{\alpha}}{\sigma} + \frac{\pi\dot{\alpha}cM/a}{8\beta^3}\frac{\mathrm{d}M}{\sigma}\right)(\sigma)\phi_m^c(s-\sigma,M)\mathrm{d}\sigma\right]
\end{aligned} \tag{1.14}
$$

$$
\begin{aligned}
C_{m,1/4}^I(t,M) = &-\int_0^s \frac{1}{M}\frac{\mathrm{d}\alpha}{\mathrm{d}\sigma}(\sigma)\phi_{m_\alpha}^I(s-\sigma,M)\mathrm{d}\sigma \\
&- \int_0^s \frac{\alpha}{M^2}\frac{\mathrm{d}M}{\mathrm{d}\sigma}(\sigma)\phi_{m_M}^I(s-\sigma,M)\mathrm{d}\sigma \\
&- \int_0^s \frac{7c}{12acM^2}\frac{\mathrm{d}\dot{\alpha}}{\mathrm{d}\sigma}(\sigma)\phi_{m_{\dot{\alpha}}}^I(s-\sigma,M)\mathrm{d}\sigma
\end{aligned} \tag{1.15}
$$

Here ϕ_n^c, ϕ_n^I, ϕ_m^c and ϕ_n^I are analogous circulatory lift response function, impulsive lift response function, circulatory moment response function and impulsive moment response function, respectively. $C_{n_\alpha}w_{3/4}$ can be written as:

$$
C_{n_\alpha}w_{3/4} = \frac{2\pi}{\beta}(\alpha V + \frac{\dot{\alpha}c}{2})
$$

for thing airfoil, with $C_{n_\alpha} = 2\pi/\beta$ as the static lift curve slope for compressible flow from Glauert rule. Moreover the analogous response functions and their exponential constant is shown to be:(with the constant are listed in Table 1.1.)

$$
\phi_n^c(s,M) = 1 - A_1 e^{-b_1\beta^2 s} - A_2 e^{-b_2\beta^2 s} \tag{1.16}
$$

$$
\begin{aligned}
&\phi_{n_\alpha}^I(s,M) = \exp(\frac{-s}{T_{n_\alpha}}),\ T_{n_\alpha} = \frac{4Mk}{2(1-M)+2\pi M^2\beta(A_1b_1+A_2b_2)} \\
&\phi_{n_M}^I(s,M) = \exp\frac{-s}{T_{n_M}},\ T_{n_M} = \frac{4Mk}{2(1-M)+2\pi M^2\beta^{-1}(A_1b_1+A_2b_2)} \\
&\phi_{n_{\dot{\alpha}}}^I(s,M) = \exp\frac{-s}{T_{n_{\dot{\alpha}}}},\ T_{n_{\dot{\alpha}}} = \frac{2Mk}{(1-M)+2\pi M^2\beta(A_1b_1+A_2b_2)}
\end{aligned} \tag{1.17}
$$

$$
\phi_m^c(s,M) = 1 - A_5 e^{-b_5\beta^2 s} \tag{1.18}
$$

Table 1.1: List of the constants of the approximated exponential series for the response function $\phi(s, M)$

A_1	A_2	b_1	b_2	A_3	A_4	b_3	b_4	A_5	b_5	k
0.3493	0.6507	0.0984	0.7759	1.5	-0.5	-0.5	0.25	1.0	5.0	0.75

$$
\begin{aligned}
\phi^I_{m_\alpha}(s,M) &= A_3 \exp(\frac{-s}{b_3 T_{m_\alpha}}) + A_4 \exp(\frac{-s}{b_4 T_{m_\alpha}}),\ T_{m_\alpha} = \frac{2Mk(A_3b_4 + A_4b_3)}{b_3b_4(1-M)} \\
\phi^I_{m_M}(s,M) &= A_3 \exp(\frac{-s}{b_3 T_{m_M}}) + A_4 \exp(\frac{-s}{b_4 T_{m_M}}),\ T_{m_M} = \frac{2Mk(A_3b_4 + A_4b_3)}{b_3b_4(1-M)} \\
\phi^I_{m_{\dot\alpha}}(s,M) &= \exp(\frac{-s}{T_{m_{\dot\alpha}}}),\ T_{n_{\dot\alpha}} = \frac{14Mk}{15(1-M) + 3\pi M^2 \beta(A_5 b_5)}
\end{aligned}
\tag{1.19}
$$

Extension to separation regime

A generally accepted and most widely used empirical model is proposed by Leishman [64, 65]. Trailing-edge (TE) separation due to its small scale, is highly relevant to the airfoil types, as is described in section 1.2.1. A reasonable modelling of the trailing edge separation can thus refer to the static aerodynamic characteristics of the airfoil. Leishman adopted the Kirchhoff model [66,67] using the concept of trailing-edge separation point f_s. This value represent the loss of circulation due to the TE separation and the movement of the aerodynamic center (x_{ac}). The normal, chord and moment force coefficients are then modelled as:

$$
C_n = C_{n_\alpha}(M) \left(\frac{1 + \sqrt{f_s}}{2} \right)^2 \tag{1.20}
$$

$$
f_s = \begin{cases} 1 - 0.3\exp[(\alpha - \alpha_1)/S_1] & \text{if } \alpha \le \alpha_1 \\ 0.04 + 0.66\exp[(\alpha_1 - \alpha)/S_2] & \text{if } \alpha > \alpha_1 \end{cases} \tag{1.21}
$$

$$
\frac{C_m}{C_n} = K_0 + K_1(1 - f_s) + K_2 \sin(\pi f_s^m) \tag{1.22}
$$

$$
C_c = \eta C_{n_\alpha} \alpha^2 \sqrt{f} \tag{1.23}
$$

One can also model the C_{n_α} as a function of both Reynolds and Mach number (Re, M). Based on the experiment data [68], a suggestion of the parameters for NACA0012 airfoil for Reynolds number $Re = 2.0 \times 10^6$ are listed in Tabel 1.2.

For the cases of unsteady airfoils, Leishman et al. [65] modelled a delayed effect of pressure distribution (C_n), boundary layer response(or separation point f_s) with first order differential equations.

$$
\begin{aligned}
&\frac{\mathrm{d}C'_n(t)}{\mathrm{d}t} = \frac{1}{T_p}(-C'_n(t) + C_n(t)) \\
&\text{where } C'_n(t) = C^c_n + C^I_n
\end{aligned}
\tag{1.24}
$$

Table 1.2: Recommended values for reconstruction of the aerodynamic coefficients for NACA 0012 airfoil, $Re = 2.0 \times 10^6$

M	C_{N_α} $(/^\circ)$	$\alpha_1(^\circ)$	S_1	S_2	$K_0(= 0.25 - x_{ac})$	K_1	K_2	m	η
0.3	0.1128	13.78	1.0	1.2	0.01	-0.128	0.04		
0.5	0.1183	9.76	0.8696	4.528				2	0.95
0.8	0.1573	6.88	0.1417	0.3177					

Table 1.3: Time constants for NACA 0012 airfoil suggested by Leishman [65]

Time constant	Description	Value
T_p	Leading edge pressure response	1.7
T_f	Separation point movement	3.0
T_v	Vortex dissipation	6.0
$T_v l$	Vortex convection time	7.5

$$\begin{aligned} &\frac{\mathrm{d}f_s''(t)}{\mathrm{d}t} = \frac{1}{T_f}(-f_s''(t) + f_s'(t)) \\ &\text{where } f_s'(t) = \mathfrak{F}\left(\alpha_E(t) = \frac{C_n(t)}{C_{n_\alpha}(M)}\right) \end{aligned} \tag{1.25}$$

$$\begin{aligned} &\frac{\mathrm{d}f_{s,M}(t)}{\mathrm{d}t} = \frac{2}{T_f}(-f_{s,M}(t) + f_s'(t)) \\ &\text{where } f'(t) = \mathfrak{F}\left(\alpha_E(t) = \frac{C_n(t)}{C_{n_\alpha}(M)}\right) \end{aligned} \tag{1.26}$$

And the normal force coefficient, moment coefficient and chord-wise force coefficient are then:

$$\begin{aligned} C_n^f(t) &= C_{n_\alpha}(M)\left(\frac{1+\sqrt{f_s''}}{2}\right)^2 \alpha_E \\ C_m^f(t) &= [K_0 + K_1(1 - f_{s,M}) + K_2(\pi f_{s,M}^m)]C_n^c + C_m^I + C_{m_0} \\ C_c^f(t) &= \eta C_{n_\alpha}\alpha_E^2\sqrt{f_s''} \end{aligned} \tag{1.27}$$

The leading-edge (LE) separation is determined by a critical normal force coefficient, C_{n_1}, depending on Mach number M. And when the criteria is reached, the vortex generated normal force is modelled as the rate change of circulation $\mathrm{d}\Gamma/\mathrm{d}t$, which is proportional to the rate of lost circulation C_v when the leading edge vortex is on the upper surface of the airfoil after LE separation occurs.

$$\frac{\mathrm{d}C_n^v(t)}{\mathrm{d}t} = \frac{1}{T_v}(-C_n^v(t) + \dot{C}_v(t)) \tag{1.28}$$

where

$$C_v = \begin{cases} C_n^c[1-(1+\sqrt{f_s''})^2/4] & \text{for } \tau_v \leq 2T_{vl} \\ 0 & \text{for } \tau_v > 2T_{vl} \end{cases} \tag{1.29}$$

As the LE separation occurs, $\tau_v = 0$ and when the LEV reaches the trailing edge, $\tau_v = T_{vl}$, the vortex passage generated moment is modelled as:

$$C_m^v = -0.25\left[1-\cos\left(\frac{\pi\tau_v}{T_{vl}}\right)\right]C_n^v. \tag{1.30}$$

As is noted in section 1.2.1, this the convection speed of the leading edge vortex is approximately 1/3∼1/2 of the free-stream velocity, and hence T_{vl} can be modelled according to the instant free-stream velocity. The time constants T_p, T_f, T_v, T_{vl} suggested by Leishman [65] are listed in Table 1.3.

1.5 The Questions

BASED on the introduction of the background, multiple questions are worth further investigation.

- What is the dynamic stall process on a rotating blade?
- **What are the differences between the 2-dimensional dynamic stall and the stall on the rotating blade?**
- How does"Rotating" affect the process of dynamic stall?
- **What role do Coriolis force and centrifugal force play in the stall process?**
- How to improve the loads prediction with the lower-order models on the rotating blade for dynamic stall cases?

In the next chapter, the literature that aims to answer these questions are analysed. The research that focuses on dynamic stall in a rotating system answers only part of the questions raised above. Some differences between the pitching airfoil and the rotating blade are noticed, but the mechanism hidden behind is not clarified. Especially the "Coriolis force influence on dynamic stall" is not answered at all. Some literature didn't touch dynamic stall sufficiently, but focused on aerodynamic phenomenon on rotating systems; or on the theoretical basis for explaining the complex vortex system. This literature is also reviewed in the next chapter and it serves as the stepping stone to further understand the dynamic stall phenomenon on the rotating system. The current work is based on the literature review and a numerical simulation is designed to answer these questions. The description of the numerical simulation is addressed at the beginning of the third chapter.

2 State of the Art: Three-dimensional Effect and Modelling

2.1 Stability of the leading-edge vortex on rotating blade

2.1.1 Spanwise flow

Since dynamic stall is closely related to the generation and shed of a vortex structure, and this dynamic stall vortex is mainly comprised of the leading-edge vortex (LEV), the stability of the LEV is hence a key point that determines the force curves and the fluid structure. Ellington [69] mentioned that the high lift on insect wings is due to the attachment of a LEV. Comparing to the high-incidence translating wings, the span-wise flow on insects' wings carries the vorticity away and delays the LEV detaching from the leading edge, which makes the LEV more stable. This is similar to the explanation of the stability of the vortex structure on a delta wing, proposed by Lee et al. [70]. They explained that the attached LEV was due to the balance of vorticity surface flux and the free-stream convection of the vorticity. The former refers the process of vorticity accumulated from the shear layer, and the latter results in the depletion of the vorticity in a third dimension comparing to a two-dimensional airfoil. Indeed, the yawing effect of a blade also means the presence of spanwise flow. Hilaire's experiment [19], as is shown in the previous chapter, showed a later stall for both lift and moment. This indicates a delay of the breach of the LEV from the leading-ledge, or in other words, the LEV is more "stable" on the swept pitching wing. Gardner et al. [71] experimentally investigated the sweep effect on a pitching wing, which used DSA-9A airfoil along the span and a positive twist to reduce the wind-tunnel wall effect. They showed that the lift stall was postponed for both forward and backward sweep, though the moment stall occurs earlier but milder. This indicates the leading-edge vortex stays longer on the pitching finite wing. Moreover, the effect of tip vortex that pinned the LEV at the leading edge is mentioned, while the topic of the stability of the LEV is not discussed.

Beem et al. [72] carried out an experiment in a water tunnel on a swept plunging wing, using swept translating motion to create strong span-wise flow on the plunging wing, they observed that the break-down and downwards convection of the vortex started at the same relative time for cases with different swept angles. Nonetheless Wong et al. [73] refuted the conclusion, and showed that the span-wise flow did contribute to the relative stability of the LEV on a flapping plate. Moreover, Beem's swept plunging wing experiment utilised direct force measurement, in contrast to the measurement of pressure on spanwise positions, and the force did show increase in the peak of the net force.

2.1.2 Other explanations: quasi-steady analogy, *Ro*, Coriolis Force

Garmman et al. [74] implemented ILES numerical simulations on a rotating plate and twisted translating plate, which have similar velocity vector and surface normal fields on the plate, and showed that the vortex structures showed limited similarity and the LEV is not maintained on the translating plate. They therefore concluded that the stability of the LEV cannot be explained using the quasi-steady analogy. Wojcik et al. [75] measured the vorticity flux of the leading-edge vortex on a rotating blade in a water tunnel, and concluded that the span-wise convection alone is not sufficient to balance the flux from leading-edge shear layer and addressed the importance of annihilation as a sink of vorticity flux, which is defined by Wojcik as the neutralisation of the oppositely-signed vortical structures.

Carr [76] investigated experimentally the effect of the aspect ratio AR on the evolving wing, and Lee et al. [77] investigated numerically the effect of Rossby number $Ro = r/c$ $(1 \sim 4)$, with r representing gyration radius and c representing chord length, as well as AR effect on the vortical structures on revolving wing. They found that the pure increasing of AR results in a larger averaged C_L along the span, and the increasing of Ro leads to the decreasing of LEV stability. Smith et al. [78] investigated numerically the Ro $(0.7 \sim 1.4)$ effect on the balance of the Coriolis force and centrifugal force, which is believed to be a pivotal factor that stabilises the LEV on revolving wings. The Ro and AR have the similar expressions, but Ro can represent a local radial (span-wise) location on a revolving wing, at the tip of the rotating wing, $Ro = AR$. However most of the research omits the interaction of tip vortex and the leading-edge vortex, when discussing the stability of LEV. These investigations focus mainly on low $Re(< 10^5)$ and small Ro, which is typical fluid properties for insects and small birds. Yet understanding how rotation augments the stability of leading edge vortex helps the comprehension of the rotation effect on dynamic stall.

A virtual experiment was performed by Jardin [79], in which a blade ($Re \sim 10^3$) was placed in a rotating flow and by alternatively adding Coriolis force and centrifugal force into the momentum equation of the Navier-Stokes equation. The lift coefficient of the blade was found to be affected drastically by Coriolis term, yet marginal by the centrifugal term. The vortex structure of each case were further examined [80], and the LEV on the outboard of the blade was found to be unstable and break down earlier for the cases for $Re > 750$ if the Coriolis term was eliminated. And hence the Coriolis force is believed to be the key factor for the stabilisation of the leading edge vortex. Wether or not this is valid for larger Reynolds number remains to be determined.

2.1.3 Theoreom: Vorticity dynamics

Reynolds [29] reviewed the unsteady separation and showed that for a two-dimensional airfoil subject to unsteady flow, the vorticity flux of a surface can be expressed as:

$$\underbrace{-\nu\frac{\partial \omega_z}{\partial y}}_{\text{Vorticity Flux}} = \underbrace{-\dot{U}_s}_{\text{Surface Acceleration}} \underbrace{-V_{tr}\omega_z}_{\text{Transpiration}} \underbrace{-\frac{1}{\rho}\frac{\partial p}{\partial x}}_{\text{Pressure Gradient}}. \tag{2.1}$$

where y is the normal direction of the surface curve, and x is along the surface. $\dot{U}_s$ is the surface acceleration along the x direction. The transpiration term is only considered when a porous region is in presence. Eq(2.1) implies that the vorticity flux contributed by the solid surface for a two-dimensional airfoil, is due to the acceleration of the surface and the pressure gradient. For an airfoil subject to a uniform free-stream velocity, the vorticity flux of the surface is the same as a uniform moving airfoil, since for both cases there is no acceleration. Wu and Wu [81] identified the vorticity flux in the vorticity transport equation, namely the total vorticity variation for a arbitrary material subdomain $\mathcal{D}$ bounded by $\partial\mathcal{D}$:

$$\begin{aligned}\frac{D}{Dt}\int_{\mathcal{D}}\boldsymbol{\omega}dV &= \int_{\mathcal{D}}(\boldsymbol{\omega}\cdot\boldsymbol{\nabla}\boldsymbol{u}+\frac{1}{\rho^2}\boldsymbol{\nabla}\rho\times\boldsymbol{\nabla}\phi)dV \\ &\quad+\int_{\partial\mathcal{D}}\boldsymbol{n}\times\boldsymbol{f}dS-\int_{\partial\mathcal{D}}\frac{1}{\rho}\boldsymbol{n}\times(\boldsymbol{\nabla}\times\boldsymbol{A})dS,\end{aligned} \tag{2.2}$$

where ϕ and $\boldsymbol{A}$ are compression and shear variables, respectively. The volume integral represents vorticity stretching/turning and the baroclinicity due to self-interaction of compressing process respectively. The first surface integral represents the effect of a nonconservative force, and the second surface integral contains the surface vorticity flux $\boldsymbol{\sigma}$:

$$\boldsymbol{\sigma}\equiv\frac{\mathbf{1}}{\boldsymbol{\rho}}\mathbf{n}\cdot\boldsymbol{\nabla}\boldsymbol{A} \tag{2.3}$$

They showed that this vorticity flux on the boundary can be expressed as:

$$\boldsymbol{\sigma}=\mathbf{n}\times(\mathbf{a}-\boldsymbol{f})+\frac{\mathbf{1}}{\boldsymbol{\rho}}\{\mathbf{n}\times\boldsymbol{\nabla}\boldsymbol{\phi}+(\mathbf{n}\times\boldsymbol{\nabla})\times\boldsymbol{A}\}\text{ on Boundary }\boldsymbol{\mathcal{B}} \tag{2.4}$$

They did further decompose these terms into four terms, representing the contributions of pressure gradient, the surface acceleration, and the non-uniformly distributed tangential vorticity or shear stress.

$$\begin{aligned}\boldsymbol{\sigma}=&\mathbf{n}\times\boldsymbol{\nabla}\boldsymbol{p} && \text{Pressure gradient}\\ &+\mathbf{n}\times\mathbf{a} && \text{Surface Acceleration}\\ &-(\mathbf{n}\times\boldsymbol{\tau_w})\cdot\mathbf{K}-\mathbf{n}(\mathbf{n}\cdot(\boldsymbol{\nabla}\times\boldsymbol{\tau_w})). && \text{Wall shear stress}\end{aligned}$$

where $\boldsymbol{K}$ is the surface tensor. Note that this surface vorticity flux is the extension from 2D Equation 2.1. For a 2D airfoil, $\boldsymbol{n}$, $\boldsymbol{K}$ and $\boldsymbol{\tau}$ are all in $\boldsymbol{xy}$ plane, hence $\boldsymbol{n}\times\boldsymbol{\tau_w}$ is in $\boldsymbol{z}$ direction, the dot product with $\boldsymbol{K}$ yielding $\mathbf{0}$; the second term of the wall shear stress gives a result, the component of which is in the $\boldsymbol{xy}$ plane, hence neither of them have any contribution to $\boldsymbol{\omega_z}$. This in turn, gives a preliminary insight into the three-dimensional effect, namely the shear stress in $\boldsymbol{yz}$ and $\boldsymbol{xz}$(due to the curvature of the surface) planes will have an effect on $\boldsymbol{\omega_z}$.

By evaluating the vorticity transport of a control volume, for example, a leading-edge vortex, one can identify the sources and sinks of the vortex system, and hence a framework is established, through which the physical mechanisms of the vorticity

system can be understood. The stability of the leading-edge vortex is such an example: through the analysis of the vorticity transport, the effect of span-wise flow, Coriolis force, centrifugal force and other effects can be better understood. Wojcik [75] considered a planar control region, and used Eq.(2.5) to identify different effects:

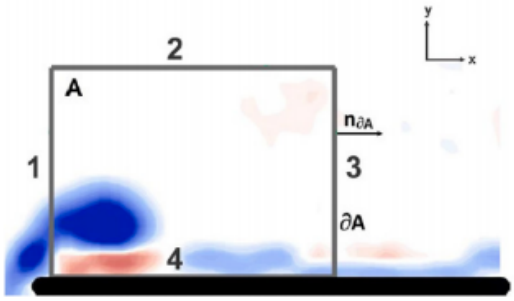

Figure 2.1: Control region for the vorticity transport analysis on a rotating and pitching flat plate by Buchholz [83], where A is the control region, and ∂A is the boundary of the region with *bound*4 aligned with the plate upper surface.

$$\frac{\mathrm{d}\Gamma}{\mathrm{d}t} = \iint_{A_z} u_z \frac{\partial \omega_z}{\partial x} \mathrm{d}A_z + \iint_{A_z} (\omega_y \frac{\partial u_z}{\partial y} + \omega_x \frac{\partial u_z}{\partial x}) \mathrm{d}A_z + \int_{L_y} u_x \omega_z \mathrm{d}L - \Phi \tag{2.5}$$

with the first term at right hand side(RHS) representing the span-wise convection of the vorticity, second term vortex tilting, third term the in-plane vortex convection, and final term the cancelation of oppositely-signed vorticity. The control region is the leading-edge vortex and no boundary flux is included. Panah et al [82] measured vorticity transport on a plunging plate, using Eq.(2.6):

$$\frac{\mathrm{d}\Gamma}{\mathrm{d}t} = \iint_{A} u_z \frac{\partial \omega_z}{\partial x} \mathrm{d}A + \iint_{A} (\omega_y \frac{\partial u_z}{\partial y} + \omega_x \frac{\partial u_z}{\partial x}) \mathrm{d}A - \oint_{\partial A} (\mathbf{u} \cdot \mathbf{n}_{\partial A}) \omega_z \mathrm{d}s + \frac{1}{\rho} \int_{bound4} \frac{\partial p}{\partial x} \mathrm{d}x \tag{2.6}$$

where *bound*4 is the wall boundary and ∂A is the boundary downstream of the control volume. In their research, the integration on *bound*4 shows strong positive vorticity, which includes also the secondary vortices, and hence did not necessarily explain the contribution of boundary vorticity flux to the leading edge vortex. Buchholz [83] derived the analysis equation on a non-inertial system that is subject to arbitrary rolling and pitching motion, see Eq.(2.7).

$$\begin{aligned} \frac{\mathrm{d}\Gamma}{\mathrm{d}t} \quad = \quad & \iint_{A} u_z \frac{\partial \omega_z}{\partial x} \mathrm{d}A + \iint_{A} (\omega_y \frac{\partial u_z}{\partial y} + \omega_x \frac{\partial u_z}{\partial x}) \mathrm{d}A - \oint_{\partial A} (\mathbf{u} \cdot \mathbf{n}_{\partial A}) \omega_z \mathrm{d}s + \nu \frac{1}{\rho} \int_{bound4} \frac{\partial \omega_z}{\partial y} \mathrm{d}x \\ & - \oint_{\partial A} 2\Omega_z (\mathbf{u} \cdot \mathbf{n}_{\partial A}) \mathrm{d}x - \iint_{A} (2\Omega_x \frac{\partial u_z}{\partial x} + 2\Omega_y \frac{\partial u_z}{\partial y}) \mathrm{d}A. \end{aligned} \tag{2.7}$$

The changes on a non-inertial reference frame is the artificial force, and the surface vorticity flux term Eq.(2.1) in the non-inertial frame is:

$$-\nu \frac{\partial \omega_z}{\partial y} = -\frac{1}{\rho} \frac{\partial p}{\partial x} - \dot{\Omega}_y r_z - \Omega_x \Omega_z r_z + (\Omega_y^2 + \Omega_z^2) r_x \tag{2.8}$$

with $[\Omega_x, \Omega_y, \Omega_z]^T$ representing the angular velocity under the non-inertial coordinate. Note that, except the general expression Eq.(2.4) derived by Wu and Wu, both Eq(2.1) and Eq.(2.8) deal with a flat plate. By comparing the Coriolis tilting terms with other fluxes, they concluded that the Coriolis force doesn't have a significant effect on circulation within the control region, which contradicts what Jardin [79, 80] suggests.

2.2 Three-dimensional effect on dynamic stall

2.2.1 Pitching Finite Wing

One cannot surpass the wing tip when a finite aspect wing/blade is considered. For non-rotating pitching finite wings, experiments observed LEV pinned at the leading edge by tip vortex. Piziali [84] measured the pressure distribution as well as the force hysteresis of different span-wise positions of a pitching finite wing. The data showed clear difference of the force hystereses at tip region from the counterpart inboard, at tip the dynamic stall force hystereses are smaller, and even lack of stall. Several consequent experimental investigations [85–87] using surface pressure distribution data, as well as smoke visualisation technique confirmed the findings of Piziali, and further demonstrates that the vortex structure on a finite wing is highly three-dimensional. Schreck [85] noted the span-wise load difference on the constant ramping finite wing. The dynamic stall vortex begins at the mid-span, and the separation of the wing begins when the vortex convection reaches the wing tip. Moreover, the vorticity in span-wise direction accumulated near the wing tip delays the vortex arching away from the tip, resulting in a "Ω-shaped" vortex structure. Conton [87] mentioned that the dynamic stall on an oscillating finite wing is characterised by an initial response of the mid-span. Once formed fully, the vorticity strength is strongest at mid-span, while its infuence was detectable at quarter chord throughout the span. The pressure distribution data also indicate the appearance of a Ω-shaped vortex. Szafruga et al. [88] used LDA technique measured the phase locked velocity at the tip area of an oscillating rectangular wing, and found a strong cross-flow even inboard at $y/c = 0.66$ (with $y/c = 0$ representing the wing tip), which has a magnitude comparable to the free stream velocity ($U_\infty = 18m/s$). Furthermore large magnitude of cross-flow was found at the tip region, confining in tip vortex, and in these regions with large cross-flow, there was no evidence of stall. Le Pape et al. [89] used combined LDV, PIV technique to provide insight on the interaction of tip vortex and the dynamic stall vortex. The dynamic stall separation that spreads from the inner part of the wing to the tip is "blocked" by the wing tip vortex, or the wing tip remains attached during the pitching motion. However they found that the swept effect can have a major influence on the interaction with the tufts visualisation.

2.2.2 Rotating Blade

There is not much literature on how the rotating environment affects the dynamic stall event. The articles that investigated dynamic stall in a three dimension and in rotating systems are reviewed as follows:

Bross et al. [90] performed an experiment on a wing going through pure pitching, pure rotating and combined pitching and rotating in a water channel. The wing is a pure rectangular plate with an aspect ratio $AR = 2$ and the pitching follows a ramp motion. They compared three dimensional vortical structures and sectional-wise properties of the plate doing these three types of motion. The rotation makes the LEV due to pitching remains closer to the plate surface, comparing to the pure pitching case. It is believed that this vortical structure is due to the effect of the unidirectional span-wise flow on the rotating plate, the unidirectional span-wise flux of vorticity and the large-magnitude downwash being shifted forward near the leading edge. They also noticed that the degradation of the tip vortex on a purely rotating case does not occur on the combined rotating/pitching case, and the trailing edge wake vortical structures are highly ordered during the pitching-up phase for the combined motion.

DiOttavio et al. [91] measured the span-wise flow on a teetering rotor in wind tunnel with particle image velocimetry (PIV). The blade is a rectangular, non-tapered blade, zero twist blade with NACA 0012 airfoil as blade section. They found that the dynamic stall is strong inboard while weaker outboard near the tip, suggesting the separation line moves towards the trailing edge as moving outboard, indicating deep stall inboard and light stall outboard. In addition, the radial flow profiles were repeatable near the surface while varies from cycle to cycle. The root mean square variation of the radial velocity suggests that the instability originates from the radial flow near the surface instead of from the outside flow. Raghav et al. [50] continued with the same experiment setup and dug further into the radial flow on the retreating blade. They came to a similar conclusion as DiOttavio et al. [91] that the radial velocity along the blade develops a sharp jet-like profile outward. The velocity profile was found to decrease in the peak velocity, and a decrease of the jet layer thickness as moving from mid-span outboard. Besides, the discrete vortical structures were discovered in the separated flow field near the blade upper surface. These vortical structures lifted off from the jet layer and carried away the roughly 30% of the vorticity in the shear layer, which is believed by Raghav et al. to be responsible for suppressing the growth of radial jet. Naghav et al. [92] investigated the effect of advance ratio μ on the life cycle of the dynamic stall on the retreating blade. They observed the dynamic stall being a result of the classical trailing edge separation, and increasing μ leads to earlier separation, which is consistent with lower Reynolds number and higher reduced freqency k. A larger μ can also shift the dynamic reattachment phase earlier. Furthermore, the vortex structure following separation appears elongated while pinned to the surface. It lifts off the blade surface and reaches maximum height at $\Psi = 270°$. The cycle to cycle (CTC) variation is also observed to maximise at this azimuth angle and then decrease. They observed significant radial flow in the separated flow regions from root to the tip, and supposed that this radial momentum transport could play an important role in the propagation of dynamic stall on a rotating blade. In addition, their experiment showed during reattachment process, there exists a locally separated zone near the leading edge, beyond which the flow is attached.

Mulleners et al. [93] implemented stereoscopic particle image velocimetry(sPIV) technique on a scaled full helicopter model in forward flight and identified the dynamic stall

events. The helicopter model had a 4-bladed rotor, with each blade having ONERA 7AD as airfoil profile, a parabolic tip, and a $-8.3°/R$ linear twist. They found out that the leading edge vortex is stretched from $r/R = 0.5$ and $r/R = 0.6$, and the vortex structure is spatially concentrated and close to the blade surface, contrary to 2D dynamic stall cases. In addition, they observed the interaction of the tip vortex and the dynamic stall vortex, which increases the three dimensionality.

Gardner [94] carried out a numerical simulation for a pitching airfoil (2D), a pitching finite wing, and a pitching while rotating blade , the reference radial location on which has the same harmonic pitch as the previous cases, in order to elucidate the rotating effect. The simulation suggests that the stall onset is postponed on a pitching non-rotating wing, and further postponed on the rotating blade. The overshoot of the moment coefficient is reduced on the pitching wing and further reduced on the rotating blade; whereas the overshoot of lift coefficient on the rotating blade is larger than the pitching wing, while both smaller than the 2D case.

Letzgus et al. [95] performed a numerical investigation on a 2-bladed model rotor with cyclic control. The blade uses DSA-9A airfoil, a $-9.3°/R$ linear twist and a parabolic shaped SPP8 blade tip. They compared three cases, two cases with low and high collective control without axial flow and one with high collective control, with axial flow. The simulation result shows that slight difference for the blade force hysteresis exists for further reducing the time step interval from $\Delta\Psi = 0.5°$. Two cases with high cyclic pitch show the stall events occurring first at radial location $r/R = 0.85$, with an Ω-shaped coherent structure and moving in board. With the presence of axial flow, the stall is weakened and only one asymmetric arch-like vortex exhibited during primary dynamic stall. All cases showed dominating radial flows after the stall took place. Schwermer et al [96] performed an experimental investigation on the model rotor as Ref. [95]. Although the cyclic pitch control was slightly different, the experiment showed a similar stall event as the numerical case. Firstly the separation begins from the leading edge, at around $r/R = 0.85$ and propagates in board. Secondly, there is a strong radial flow in the stalled region, and the radial flow velocity increases as moving from blade root to tip, which is contrary to Raghav's [50] observations. Thirdly, the tip area stall was postponed. Furthermore, they noticed the untwisting of the blade due to the aerodynamic loads to be constantly 0.8° for the whole cycle. Letzgus et al. [97] carried out numerical simulations on the same case as Schwermer's experiment [96], and compared the simulation results of different numerical solvers and different turbulence models. They concluded that the blade elasticity, rotor head and shear layer effects of the wind tunnel seem to be negligible. Among all the set-ups, the delayed detached-eddy-simulation(DDES) captures the flattening of lift polar beyond the static stall angle, which was observed in the experiment, and it is capable of reproducing cycle-to-cycle(CTC) variations for the separated flow, while unsteady Reynolds average numerical simulation (URANS) with Menter-SST and Spalart-Allmaras (SA) turbulence models can not. However, DDES approach showed strong artificial vortex that influenced the lift and nose-down pitching moment, which was not observed in the experiment and URANS results. In addition, the difference in the result by two solvers doesn't tell anything, since their grid strategies are totally different.

Richez [98] did a numerical simulation on a 4-bladed 7A rotor in forward flight. The cyclic control is solved by coupling a comprehensive analysis tool HOST and the computational fluid dynamics(CFD) code, and the force curves on a certain radial locations were compared with experiment measurements to guarantee the validation. The rotor has a $-8.3°/R$ twist. A shape factor based criteria has identified 3 different separation regions from the simulation, the trailing edge separation, the leading edge separation and the shock induced separation. The rotor map shows the beginning of trailing edge separation for the inboard part of the blade in third quadrant of the rotor disk. And the leading edge separation happens at the blade tip at the beginning of the fourth quadrant of the rotor disk. The shock-induced separation appears on the tip at the end of the fourth quadrant. However the tip shock-induced separation doesn't show strong relations associated with stall hysteresis. The simulation also show clearly the onset of stall as an impact of the tip vortex of a previous blade. Gibertini et al. [99] carried out an experimental investigation on a model rotor wind tunnel with a descending flight condition. The measurement shows a deficit in the thrust coefficient, which was believed to be a consequence of a perpendicular vortex filament induced stall.

Ruan et al. [100](the current author) did a numerical simulation on a single blade rotating with cyclic pitch control in forward flight state. The cyclic control was obtained with comprehensive analysis tool CAMRADII. The blade is a rectangular untwisted blade with NACA0012 airfoil profile, and the grid convergence study is carried out to increase the credibility. They identified three different types of separation: the leading edge separation, full separation and shock-induced separation. The simulation result shows drastic interaction between the dynamic stall vortex and the tip vortex, which yields a pair of counter-rotating vortex in the near wake. They also noticed a swell structure emerging inboard and convects outboard, which plays a significant role in the dynamic stall event after the primary DSV sheds outboard. The comparison of a slice at $r/R = 0.898$ with an airfoil pitching in a uniform free stream velocity shows drastic differences in terms of the stall onset, the maximum overshoot and the separated flow after the shedding of the primary DSV. They also tried to figure out the effect of Coriolis force and centrifugal force on the swell structure.

The investigation methods, objectives or main conclusions, rotor characteristics and flight state are summarised in Table 2.1. The research is not systematic compared with that of the 2-dimensional pitching airfoil, in which the effect of different parameters have been well interpreted, while three-dimensionality has just drawn researchers' attention recently. Researchers in the field of helicopter technologies focused mainly on the traditional pseudo-steady flow characteristics, for example, the separation points, the pressure profile, etc., while other researchers in the field of bio-fluid mechanics are engrossed in modern unsteady fluid mechanical theories, such as vorticity dynamics. The research fields in bio-fluid mechanics that deals with rotating, pitching, plunging motions, though mostly characteristic of low M and Re, serve to provide new perspectives to understand the classical problems on the helicopter blades. And with the better understanding of the unsteady phenomenon, the quasi-3D models that is widely used in helicopter aerodynamics to predict the aerodynamic loads may be revised for the dynamic stall cases.

Table 2.1: Summary of the literature on three-dimensional dynamic stall on rotating system

Literature	Method .	Main Objectives	Additional information		
			Model & Blade geometry	Flight state	Tip Aerodynamic Parameters
Bross et al. [90]	Experiment; PIV; Water channel	Comparison of vortical structures: pitch, rotate, pitch+rotate	Flat plate; $AR = 2$; $c = 0.0381m$; $R = 0.113m$;$t = 2.8mm$	–	$Re = 1.2 \times 10^4$
DiOttavio et al. [91]	Experiment; Wind tunnel; PIV	Measurement of radial flow	2-bladed teetering rotor NACA0012; Rectangular; untwisted; $AR = 3.49$; $c = 0.178$m; $R = 0.889$m	Forward flight; $\mu = 0.33$	$Re = 3.0 \times 10^5$ $M_{\max} = 0.07$
Raghav et al. [50]		Investigation of radial jet-like layer			
Raghav et al. [92]		Investigation of the effect of advance ratio μ on radial flow		$\mu = 0.4$	
Mulleners et al. [93]	Experiment; sPIV	Identification of dynamic stall event on different radial locations	4-bladed full helicopter model ONERA 7AD; Parabolic tip; $\tau = -8.3°/R$; $AR = 15$; $c = 0.14$m; $R = 2.1$m	Forward flight; $\mu = 0.42$; $U_\infty = 88.3$m/s	$Re = 2.1 \times 10^6$ $M_{\max} = 0.876$
Gardner et al. [94]	Numerical Simulation;	Comparison of stall hystereses on: pitching airfoil(2D), pitching finite wing; pitching + rotating blade.	Single blade; OA209; Rectangular; untwisted $AR = 8.3$; $c = 0.3$m $R = 4m$	Hovering with cyclic pitch	$Re = 1.7 \times 10^6$ $M = 0.45$

Letzgus et al. [95]	Numerical simulation	Grid resolution study; Axial flow effect on dynamic stall	2 bladed model rotor; DSA-9A Parabolic tip; $\tau = -9.3°/R$ $AR = 18$; $c = 0.027$m $R = 0.65$m	Hovering with cyclic control	$Re = 1.0 \times 10^6$ $M = 0.6$
Schwermer et al. [96]	Experiment; PIV; Wind tunnel;	Investigation of dynamic stall on rotating blades		Hover with cyclic control; $U_{\infty,axial} = 2.2$m/s	$Re = 4.6 \times 10^5$ $M = 0.28$
Letzgus et al. [97]	Numerical simulations	Comparing the simulation results of different solver, turbulence models with experiment results.			
Richez [98]	Numerical simulation	Identification of separation types; Discovered BVI induced dynamic stall	4-bladed root-cut rotor; OA213 for $r/R < 0.75$ OA209 for $r/R \leq 0.9$ $\tau = -8.3°/R$; $AR = 12$; $c = 0.14$m; $R = 2.1$m	Forward flight $\mu = 0.3$	$Re = 2.3 \times 10^6$ $M_{\max} = 0.84$
Ruan et al. [100]	Numerical simulation	Vortical structure of dynamic stall on rotating system; DSV-tip interaction; Comparison with 2D simulation	Single blade; NACA0012; Rectangular; untwisted; $AR = 4$; $c = 0.15$m; $R = 0.8$m	Forward flight; $\mu = 0.21$	$Re = 2.8 \times 10^6$ $M_{\max} = 0.783$

2.3 Prediction of dynamic stall on rotating blade: Lower Order Models

To improve the accuracy of lower order aerodynamic models including dynamic stall, the selection and development of inflow models, or wake models is the prior consideration. Lee et al. [101] evaluated different inflow models in a comprehensive analysis for a AH-1G flight test, although the Leishman's dynamic stall model is integrated, the predicted forces on the blade deviate to a greater extend than the 2D Leishman's model for all in-flow models. Moreover, the inflow model that results in a deficit estimation at 60% radii may show an over-prediction at 90% radii. The author attributed the errors to the re-attachment phase of the 2D dynamic model, yet the over-prediction or under-estimation in the up-ward pitching phase on the 3D case may indicate the absence of some factors in the present models.

Modarres [102] extended from 2D dynamic stall model, and developed a semi-empirical model for 3D dynamic stall, which includes what he called radial coupling. A convection equation is added to the blade element method,

$$\frac{\partial \Gamma_i}{\partial t} + U_R \frac{\partial \Gamma_i}{\partial r} = \dot{\Gamma}_i \text{ (without radial coupling)} \tag{2.9}$$

and here U_R is the yaw effect, and $\dot{\Gamma}_i$ is similar to $\mathrm{d}C_v/\mathrm{d}t$ in Eq.1.28. However the comparison between the lower order model and experiments, flight cases or higher order models, e.g. CFD simulations, are not presented. And this radial coupling is also not validated.

3 Method

3.1 Objective of this thesis

In order to answer the questions that are raised in section 1.5, based on the literature review, the following numerical experiment and analysis process are designed, such as to avoid possible blade vortex interaction (BVI) triggered dynamic stall, twist, and tip shape effect.

- A single rigid, rectangular, untwisted rotating blade (angular velocity Ω) set with 0 inclined angle in a free stream $U_\infty = \mu\Omega R$, with pitch control θ_0, θ_c andθ_s, so that the pitch angle in each revolution satisfies:

$$\theta = \theta_0 + \theta_s \sin\Psi + \theta_c \cos\Psi, \tag{3.1}$$

  with Ψ representing the azimuth angle defined in Figure 1.4.

- One equation turbulence model (SA model) and two-equation turbulence model ($k-\omega$ with Menter SST version) are utilised for the computational fluid dynamic simulation of the flow field around the rotating blade.

- The simulated flow field is to be analysed in detail, aiming to address the full picture of dynamic stall phenomena on a single rotating blade.

- Vorticity transport function is to be analysed on a planar control region at slices near $r/R = 0.898$, to illustrate the role of the rotating effect. (The location $r/R = 0.898$ is the place where the symmetric plane of the main Ω-shaped vortex structure dwells.)

The parameters for simulation are summarised in Table 3.1. The pitch control is a rough approximation by CAMRAD II [10] with $T = 900N$ and $M_x = 0$, $M_y = 0$ as the trim condition.

Table 3.1: Parameters for simulation

Flow conditions		Blade geometry and pitch control	
Air density ρ	1.225 kg/m^3	Airfoil type	NACA0012
Temperature T	$289K$	Chord c	0.15m
Rotor angular velcoity Ω	275 rad/s	Rotor radius R	0.8m
Tip Mach number $M_{tip} = \Omega R/a$	0.5456	Blade aspect ratio AR	4
Advance ratio μ	0.2	Pitch control θ_0, θ_c, θ_s	13.18°, 7.74°, −5.57°

3.2 Acquiring data of dynamic stall on a rotating system: Numerical Approach

3.2.1 Governing Equation and flux definitions

The Navier-Stokes equations for a three-dimensional case can be written in conservative form as:

$$\frac{\partial}{\partial t}\iiint_V \vec{W}\, dV = -\iint_{\partial V} \bar{\bar{F}} \cdot\, d\mathbf{S} = 0 \tag{3.2}$$

where

$$\vec{W} = \begin{pmatrix} \rho \\ \rho u \\ \rho v \\ \rho w \\ \rho E \end{pmatrix}$$

is the conserved quantities' vector. V denotes an arbitrary control volume with the boundary ∂V and the surface with the outer normal vector $\mathbf{S}$. The flux density tensor $\bar{\bar{F}}$ is composed of the flux vectors in three coordinate directions:

$$\bar{\bar{F}} = (\vec{F}_i^c + \vec{F}_v^c)\cdot\vec{e}_x + (\vec{G}_i^c + \vec{G}_v^c)\cdot\vec{e}_y + (\vec{H}_i^c + \vec{H}_v^c)\cdot\vec{e}_z \tag{3.3}$$

with $\vec{e}_x$, $\vec{e}_y$,$\vec{e}_z$ denoting the unit vectors in the coordinate directions. The indices i and v represent the inviscid and viscous contributions, respectively. The inviscid and viscous fluxes are:

$$\vec{F}_i^c = \begin{pmatrix} \rho u \\ \rho u^2 + p \\ \rho uv \\ \rho uw \\ \rho Hu \end{pmatrix},\ \vec{F}_v^c = -\begin{pmatrix} 0 \\ \tau_{xx} \\ \tau_{xy} \\ \tau_{xz} \\ u\tau_{xx} + v\tau_{xy} + w\tau_{xz} + \kappa_l \frac{\partial T}{\partial x} \end{pmatrix}, \tag{3.4}$$

$$\vec{G}_i^c = \begin{pmatrix} \rho u \\ \rho uv \\ \rho v^2 + p \\ \rho vw \\ \rho Hv \end{pmatrix},\ \vec{G}_v^c = -\begin{pmatrix} 0 \\ \tau_{xy} \\ \tau_{yy} \\ \tau_{yz} \\ u\tau_{xy} + v\tau_{yy} + w\tau_{yz} + \kappa_l \frac{\partial T}{\partial y} \end{pmatrix}, \tag{3.5}$$

$$\vec{H}_i^c = \begin{pmatrix} \rho u \\ \rho uw \\ \rho vw \\ \rho w^2 + p \\ \rho Hw \end{pmatrix},\ \vec{H}_v^c = -\begin{pmatrix} 0 \\ \tau_{xz} \\ \tau_{yz} \\ \tau_{zz} \\ u\tau_{xz} + v\tau_{yz} + w\tau_{zz} + \kappa_l \frac{\partial T}{\partial z} \end{pmatrix}. \tag{3.6}$$

The pressure is calculated by the state equation:

$$p = (\gamma - 1)\rho(E - \frac{u^2 + v^2 + w^2}{2}). \tag{3.7}$$

For a control volume fixed in time and space, the temporal change of the conservative variables $\vec{W}$ can be derived from equation3.2

$$\frac{d}{dt}\vec{W} = \frac{\partial}{\partial t}\vec{W} = -\frac{\iint_{\partial V} \bar{\bar{F}} d\mathbf{S}}{\iiint_V dV} \equiv -\frac{1}{V} \cdot \vec{Q}^F \tag{3.8}$$

with $\vec{Q}^F$ representing the fluxes over the boundaries of the control volume. If the boundary is divided into n faces, $\vec{Q}^F$ is given by:

$$\vec{Q}^F = \sum_{i=1}^{n} \vec{Q_i}^F = \sum_{i=1}^{n} (\vec{Q_i}^{F,c} - \vec{D}_i)$$

where $\vec{Q}^{F,c}$ represent the fluxes over the respective face.

3.2.1.1 Flow Solver

The numerical simulation, or more specifically, the computational fluid dynamics is fully based on the DLR-TAU code [103], which is a three-dimensional, parallel, hybrid, multigrid code. The finite volume scheme for solving the Reynolds-averaged Navier-Stokes (RANS) equations is implemented and the flow variables are stored on the vertices of the initial grid. The spatial discretization is cell-vertex with a dual metric, which is computed during the preprocessing step.

3.2.1.2 Detailed solver settings

- Inviscid flux discretisation: Central scheme
  - Central dissipation scheme: Scalar dissipation [104]
  - Central convective mean flow flux: Flux of average, the flux is the analytic flux of centrally averaged conservative variables on the face.
  - Central convective turbulence flux: second order upwind scheme for turbulence flux
  - Compute exact whirl flux: due to the rigid body motion of the blade, the additional flux is integrated over the control volume surface.
- Viscous flux type TSL/Full: Full, using a full gradient based approach to evaluate viscous fluxes;
- Gradients reconstruction: Least square with QR decomposition and Gram-Schmidt orthogonalisation

Explanation: It is first described by Anderson, Bonhaus [105] and Haselbacher, Blazek [106] This approach has shown much more accurate gradients as in comparison to the Green-Gauss theorem. Using the achieved better robustness and more accurate solutions as the Green-Gauss approach. This viable algorithm reconstructs linear functions exactly on any type of mixed grids. (Or hybrid grid.)

- Turbulence models: the linear eddy-viscosity models
  - Boussinesq hypothesis: $\bar{\rho}\tilde{R}_{i,j} = -2\mu^{(t)}\tilde{S}_{i,j} + 2/3\bar{\rho}\tilde{k}\delta_{i,j}$
  - Spalart-Allmaras model with Edwards and modification [107]: a single transport equation for "SA viscosity" $\tilde{\nu}$ is employed.
  - $k-\omega$ model, Menter Shear Stress Transport (SST) 2003 version [108–110]: two transport equations for the specific kinetic turbulence energy $\tilde{k}$ and the specific dissipation rate ω are solved to obtain the eddy viscosity $\mu^{(t)}$.
- Time stepping
  - Relaxation solver: implicit backward Euler
  - Time-accurate computations: Dual-time stepping, with CFL number 0.7.
  - Inner iterations per time step: $200 \sim 400$
- Convergence criteria
  - Relative Cauchy convergence control on C_L, C_D, C_{my} for inner iterations.

    Explanation: If any of the force coefficients sequences $C_L(N)$, $C_D(N)$ and $C_{my}(N)$ in the last 30 inner iteration steps satisfies:

    $$C_X(m) > C_X(m+1) \text{ for } m \in \mathbf{N}, \tag{3.9}$$

    and

    $$|\frac{C_X(N) - C_X(N-1)}{C_X(N-1)}| < 1 \times 10^{-7} \text{ for } N = 30, \tag{3.10}$$

    The relative Cauchy convergence criteria is reached.
  - Global residual: The based on the initial value normalised $||res_\rho^n||'$ drops 2 orders of magnitude

Explanation: The global density residual $||res_\rho^n||$ at pseudo-time step n for the monitoring output is computed as the root mean square value:

$$||res_\rho^n|| = \sqrt{\sum_{j=1}^{N_p} \frac{[res_\rho^n(j)]^2}{N_p}}. \tag{3.11}$$

and the normalised $||res_\rho^n||' = ||res_\rho^n||/||res_\rho^{N_0}||$, where N_0 is the initial pseudo time step in a new dual time stepping.

- Multigrid level: 3

Explanation: The normal convergence behavior of an iteration method slows down after a rapid start, due to the fact that low frequency errors are hardly damped. Multigrid method can well resolved these low frequency errors (attached to a long wavelength) on a coarser mesh. And the number of equations to be solved decreases with the number of agglomerated volumes. It is based on the numerical simulation experience with TAU code that level 3 is an adequate choice as a trade-off of computational resource and accuracy.

3.2.2 Grid Strategy

3.2.2.1 Chimera technology in DLR-TAU

The overset grids method was originally introduced for building structured meshes over a complicated configuration. Steger et al. [111], Benek et al. [112] developed overset grid method in two and three dimensions for Euler Equations. Dougherty et. al. [113, 114] extended this technique to allow movement of embedded meshes, which is powerful to deal with moving bodies. In order to overcome the shortcomings of the algorithm, such as loss of conservation, extra computation cost due to interpolation and locally reduced accuracy due to mismatched cell sizes between the overset meshes, three major steps in DLR-TAU code is implemented to improve the aforementioned problems.

- The creation of the overlapping region: In order to guarantee that in the chimera search process, all points have a donor cell for linear interpolation, a sufficient grid overlap layers is necessary.
- The cell surrounding each interpolation point is searched from the other grids, using Alternating Digital Tree (ADT) [115].
- The conservative variables are transferred by linear or trilinear interpolation [116].

The parallel chimera method has also been developed, one can get more information on the algorithms and implementations from Ref. [117].

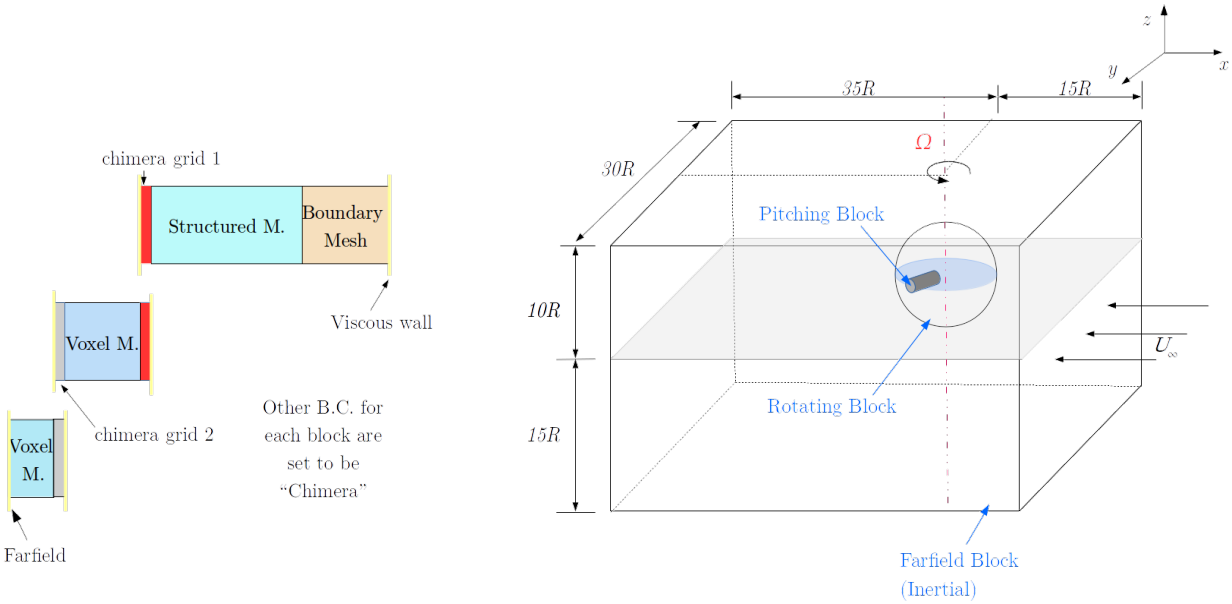

(a) (b)

Figure 3.1: (a) Schematic plot of chimera grid strategy. Red and grey squares represent two overset meshes (chimera meshes); yellow lines represent the boundary conditions for each block. (b) Schematic plot of the computation field, which consists of pitching, rotating and far-field (inertial) block.

3.2.2.2 Overview of the blocks

In order to avoid the appearance of orphaned points due to the motion of the blade, and to guarantee the minimum interpolation error in the chimera layer between the blocks, we set up a shapes and discretisation that are homogeneous in the motion direction. Or in other words, using cylindrical shape with its centreline aligned with pitching axis for the pitching motion, so that as the blade pitches, the outer surface stays in a fixed region, and hence the overlapping region can also be fixed. Similarly, axisymmetric body, such as a sphere or cylinder for the rotating motion can also provide such a condition. In addition, the homogeneous discretisation in the arc direction guarantees the best interpolation quality. The schematic plot of the grid strategy is presented in Figure 3.1. The size of the far-field is determined such that the influence of the wake is small to a great extend on the far-field boundaries. This value is mostly empirical, $5R \sim 8R$(5 $\sim$ 8 times of the blade rotating radius) seem to be sufficient [118] to yield a result comparable to flight test. $20 \sim 30R$ were adopted by early literature [98] for simulating dynamic stall on a forward flying helicopter. Figure 3.2 shows the generated mesh.

Pitching Block

The process and detailed data to create the surface mesh and pitching block are documented here, so that anyone can start from the current work and further improve the

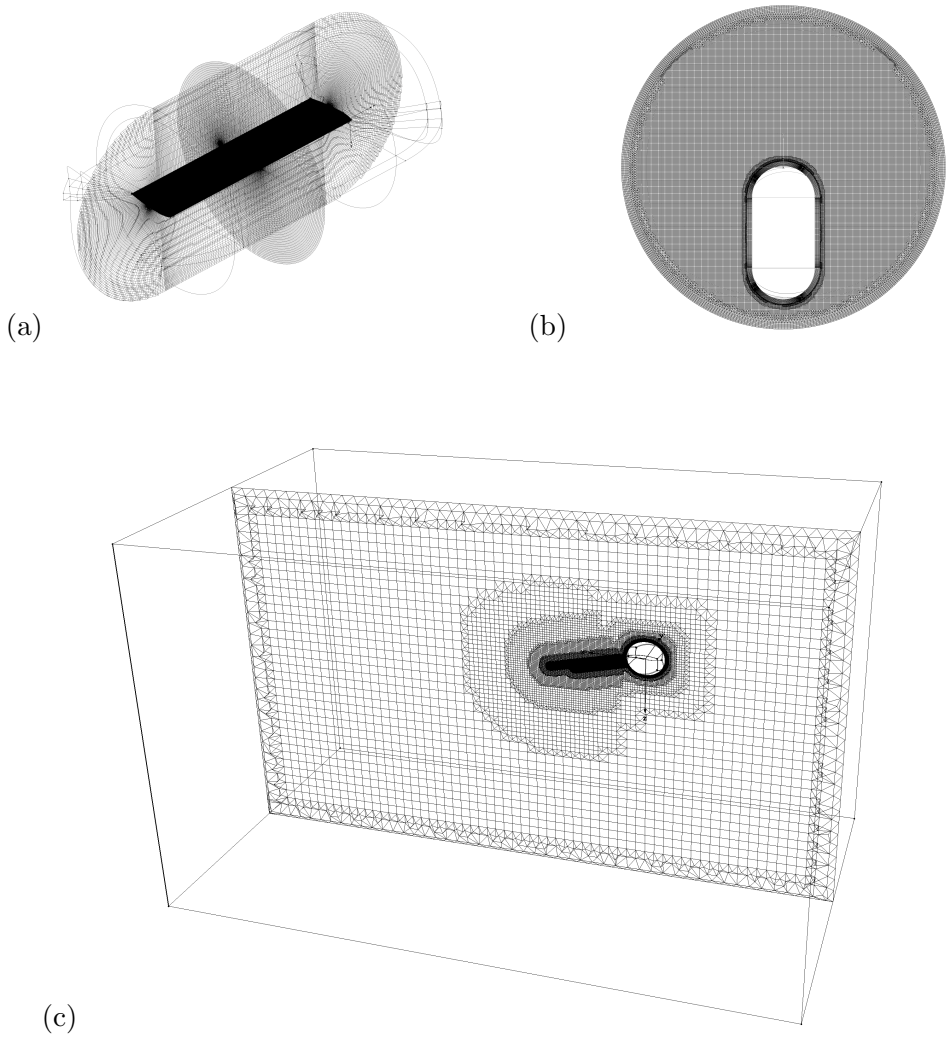

(a) (b)

(c)

Figure 3.2: Configuration of the mesh: (a) blade block, (b) voxel rotating block, (c) voxel farfield block

mesh quality for high fidelity simulations, such as LES, DDES approach. The difficult part of creating structured grid on a curved surface is separating the areas. The division of curved surface at the blade tip, the extruded boundary layer mesh and the pitch block topology are presented in Figure 3.3; the spacing, distribution of the points are listed in Table 3.2. The basic steps for the establishment of the surface grid in Pointwise [119] are:

- Determine the tip region, which is $l_0 = 5\%c$ from the tip $y = 800$mm, and the transition region, which is $l_1 = 20\%c$ from the tip;
- Assign grid points on half of the airfoil according to Table 3.2, and split at LE and TE at twelfth nodes counting from both ends;
- Create connectors Con-h and Con-v for both LE and TE;
- Assemble domains from the connectors created, and smooth the mesh on the tip of the model using laplacian method.
- Smooth the domain by setting Con-2 to be a boundary of the domain, at which the adjacent cells satisfy orthogonality and the size of the cells are equal to the mesh on the other side of the connector (in the transition part).

And the boundary mesh is created by extruding the surface mesh normally into the space, with setting the initial step $\Delta s = 7 \times 10^{-4}$mm and a growth rate of 1.05 for 20 steps, 1.1 for 40 steps. The extrusion method is hyperbolic and total steps are 60, which makes the connector Con-transition's node number to be 61. Based on the extruded block surface, the rest parts of the pitch block is built:

- Create a half sphere centering at $\begin{pmatrix} 0 & R - 0.2c & 0 \end{pmatrix}$, and project all the connectors on to the half sphere;
- Create domains on the half sphere with the projected connectors, and smooth the domains with laplacian method;
- Create connectors to between the two surfaces (boundary mesh surface and spherical surface);

  Note that the connectors should be adjusted in the way that both ends are perpendicular to the domain surfaces.
- Create domains from the newly created connectors and assemble block-parts from these domains;
- Select all the inner block-parts and smoothing by setting the inner domains as floating;
- Repeat the process on the other end of the model, and close the pitch block with creating a structured block-part between two tip block-parts.

- Extrude the outer surface domain of the pitching block normally for 5 steps, with equal space 6.67%c, to create the chimera mesh.

Since the model is using the symmetric NACA0012 airfoil and the model itself is symmetric by plane $y = 500$mm, the steps listed above together with the data in Table 3.2 are sufficient for recreating the mesh in Pointwise. We compare the spatial resolution of the current pitching block with that by Richez [98] in Table 3.3.

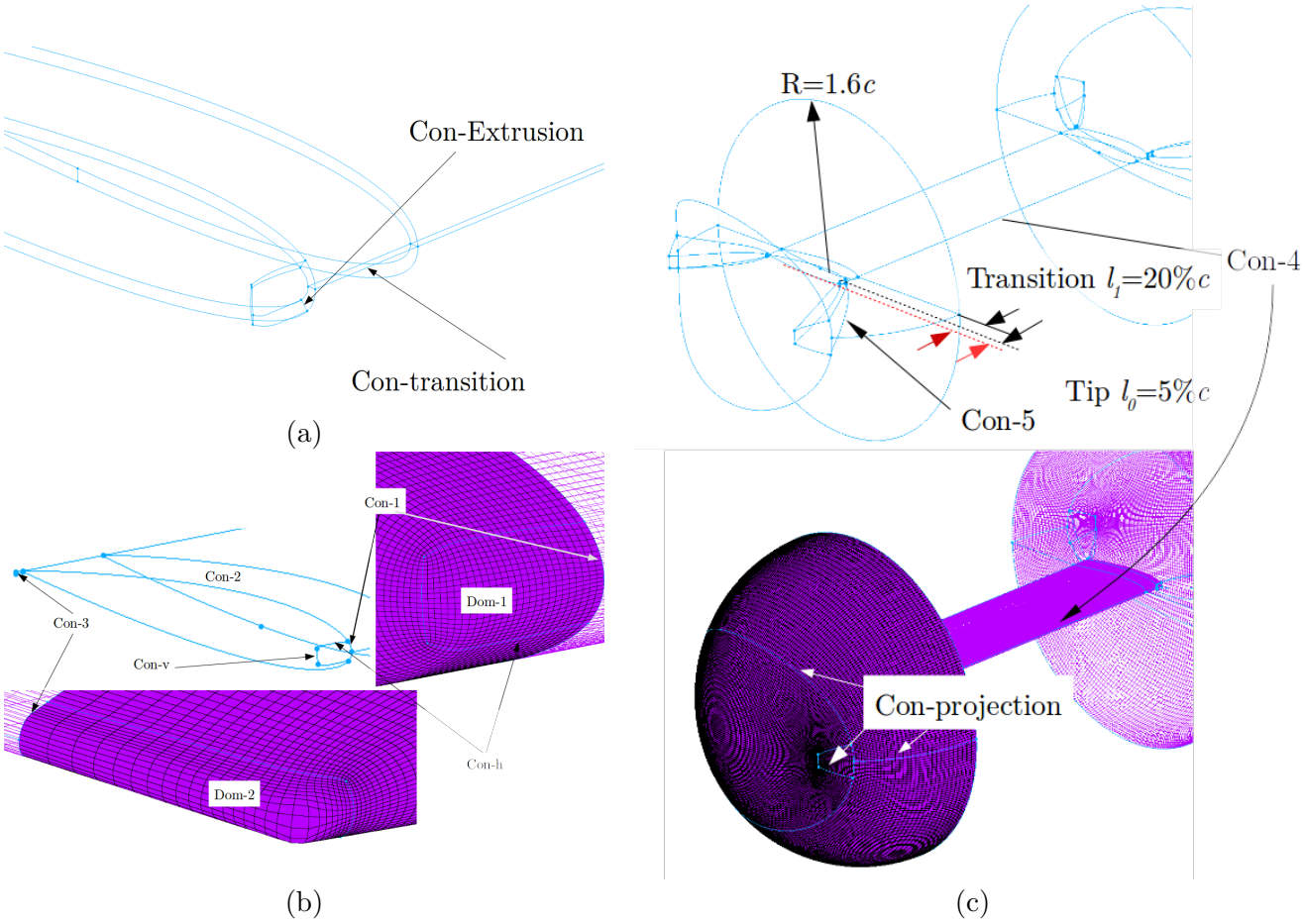

Figure 3.3: Details of (a) normally extruded boundary block from surface mesh, (b) surface mesh on the blade, and (b) structured pitch block topology built on the boundary layer mesh.

Table 3.2: Details of the connectors

Connector ID	Number of nodes	spacing Δs	Other information
Combined Con-1,2,3	183	Δs-LE: 0.2	Distribution function: Tanh
Con-1, Con-2	12	-	Directly split from Combined Con-1,2,3
Con-h	28	-	Lines projected onto the surface.
Con-v	23	-	
Con-4	101	Δs at both ends equal to tip distributions	Distribution function: Tanh
Con-transition	33	LE: $\Delta s_{tip} = 0.477$; $\Delta s_{mid} = 1.033$ TE: $\Delta s_{tip} = 0.306$; $\Delta s_{mid} = 1.2$	Distribution function: Tanh
Con-Extrusion	61	$\Delta s_{1st} = 7 \times 10^{-4}$; $\Delta s_{end} = 0.1655$	Distribution function: constant growth rate, 1.05 for the first 20 steps, 1.1 for the rest 40 steps.
Con-projection	-	-	Projected from connectors in tip region, using laplacian smoothing
Con-5	65	both ends adjusted according to $\Delta\bar{s}$ of the point on the surface that they are connected with.	Distribution function: Tanh

Table 3.3: Comparison of the spatial resolution between current simulation and the 7A rotor mesh of [98]

	Current Simulation	**7A Rotor [98]**
N around airfoil	364	313
N over the blade span/AR	55.25	10.33
N inside the boundary layer at midchord and $r/R = 0.8$	56	40
Max y+	0.55	0.4
$\Delta s/c$ at LE	0.133%	0.11%
max $\Delta s/c$ chord-wise	1.3%	1.6%
max $\Delta s/c$ normal to wall	4.6%	5.6%

Rotating Block

The details of the rotating block is shown in Figure 3.4 and in Table 3.4. Basic steps to create the rotating block is as follows:

- Create an sphere with radius $R_0 = 3R$, and scale the sphere in z direction with a factor of 0.9 in order to decrease the number of cells in z direction;

- Draw 12 connectors that form a hexahedron, and project them onto the oval surface. Setting the numbers of the connectors Con-H to be 111, and Con-V to be 54;
- Assemble domains from these connectors and smooth with laplacian method on the oval surface;
- Create the unstructured voxel block using the chimera mesh's outer surface of the pitching block, and the newly created domain, adjust the parameters to yield the space as listed in Table 3.4

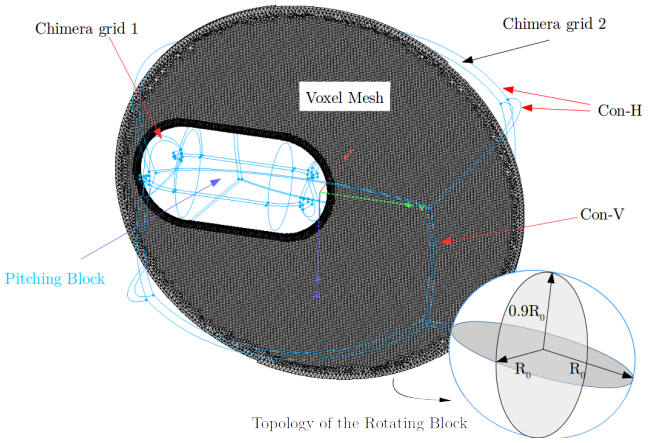

Figure 3.4: Details of the rotating block and its topology.

Table 3.4: Details of the rotating block

Structured surface mesh		Unstructured voxel grid	
$\Delta\bar{s}$	18.50mm	$\Delta\bar{s}$	8.29mm
$(\Delta\bar{A})^{1/2}$	18.76mm	$(\Delta\bar{V})^{1/3}$	7.44mm
No. Cells	47,520	No. Cells	15,025,551

Farfield Block

In order to resolve the wake, we tried two different methods: (1) using a point cloud that forms a helical path; (2) using a structured, finely designed mesh. The first method can save computation resources, but since the wake doesn't strictly follow a helical path, there will be artificial diffusion of the wake due to the grid size change. The second method can relieve the aforementioned problem to a great extend, but costs more computing resources. We compare these two methods and try to figure out if the wake has a great impact on the dynamic stall event in a forward flight state.

The first method is shown in Figure 3.5 (a), and the second method is shown in Figure 3.5 (b). The detailed spacing information is listed in Table 3.5.

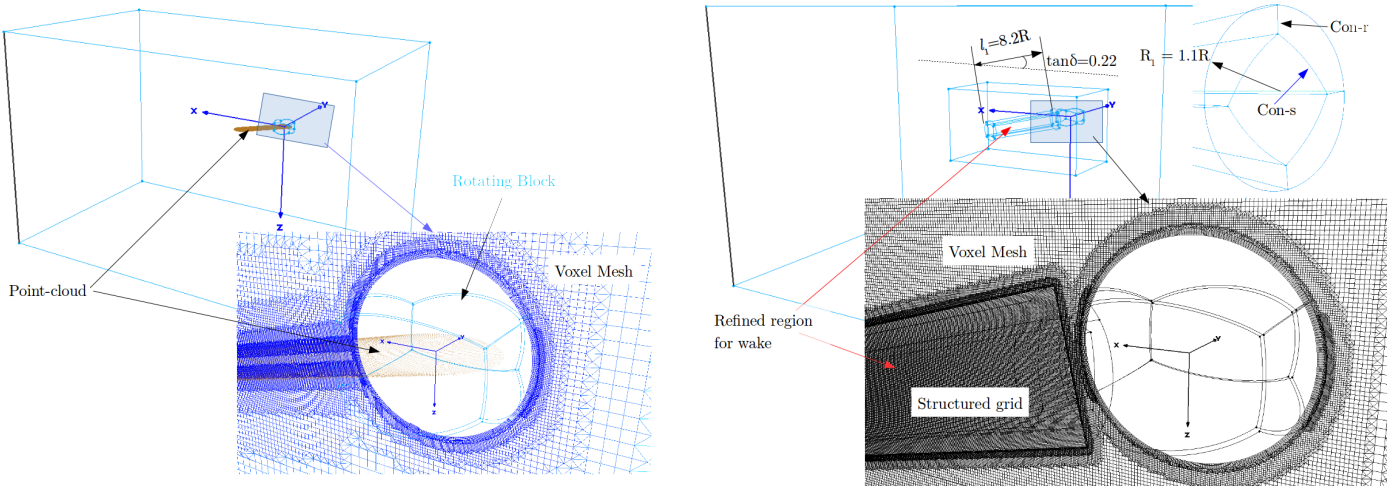

(a) (b)

Figure 3.5: Details of the far-field block (a) with point-cloud refined grid; (b) with a structured cylindrical refined grid for the wake region.

Table 3.5: Details of the farfield block

Parameters	Point-cloud refined	Structured grid refined	
		Farfield together	Structured Wake region
$\Delta\bar{s}$, (mm)	33.17	31.54	12.23
$\Delta s_{\max}$, (mm)	1514.93	1326.65	18.00
$(\Delta\bar{V})^{1/3}$, (mm)	126.83	82.89	7.44
$(\Delta V_{\max})^{1/3}$, (mm)	607.80	443.27	16.21
No. Cells	11,527,188	22,496,336	7,772,310

3.3 Validation of the grid strategy

3.3.1 Voxel grid: Hovering case

The Caradonna–Tung rotor model is adopted, and the surface mesh follows the same space criteria as described in Section 3.2.2. The only difference of the blade block is the root part, where unstructured pyramids' prisms and tetrahedra are used, as shown in Figure 3.6a. The farfield block consists of a region that is uniformly spaced as the rotating block in current simulation and the voxel grid growing from small to large scale on a farfield boundary. The region right below the rotor is refined with a point source in order to catch tip vortex trajectories, as shown in Figure 3.6b. The flow condition is summarised in Table 3.6, and the comparison of grid for the simulation and validation case are summarised in Table 3.7. The numerical method for the hovering case is the same as the current simulation, except that the rigid motion herein includes only rotation of the whole block. The Spalart–Allmaras turbulence model is adopted. Figure 3.7 shows the thrust coefficient along the simulation revolutions, and Figure 3.8 shows the comparison of the pressure coefficients on $r/R = 0.5$, $r/R = 0.8$, $r/R = 0.96$ span-wise locations. Figure 3.9 shows the tip vortex trajectory using Q-criterion shaded with vorticity magnitude.

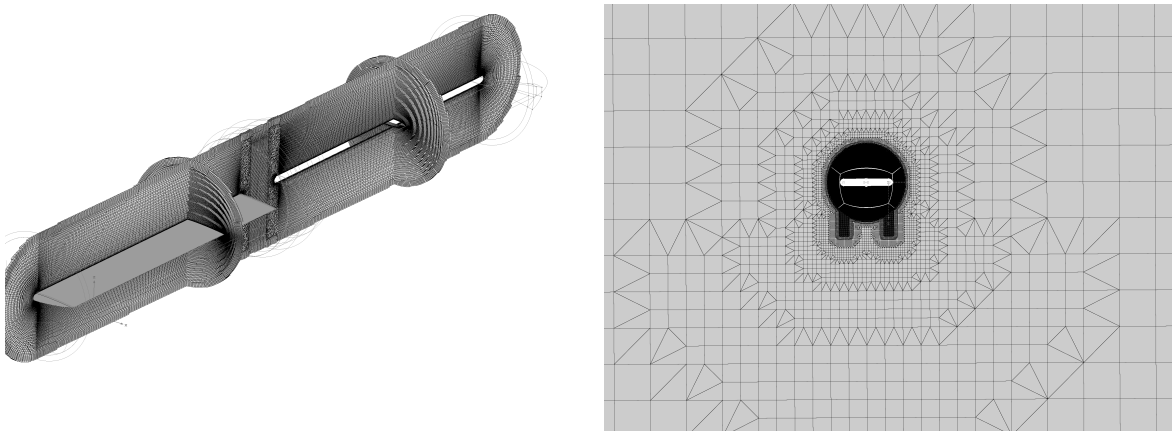

(**a**) Blade block (**b**) Farfield block

Figure 3.6: Configuration of the mesh for validation: (**a**) blade block; (**b**) voxel farfield block.

The thrust coefficient of the experiment is $C_T = 0.00473$, and the validation case gives a value of 0.00566, which is 19.6% larger than experiment data, which is consistent with the pressure coefficient, where, at $r/R = 0.8$, the maximum Cp has an error of 11.55%. Comparing the simulation result of the hover case with the Experiment data from [120], we conclude that the SA turbulence model is capable of qualitatively catching the main characteristic of the pressure distribution on the blade in rotation environment, and the voxel grid with point source as refinement is able to keep track of the tip vortex outside the fine grid region. The same mesh strategy and turbulence utilised for the current

Table 3.6: Flow condition for validation.

Chord length c (m)	0.195
Aspect Ratio AR	6
Tip Mach number, $M_{tip} = \Omega R/a$	0.877
Tip Reynolds number Re_{tip}	3.93×10^6
Tip velocity U_{tip} (m/s)	299.24
Collective pitch $\theta(°)$	8
Angular Velocity (rad)	255.76

Table 3.7: Comparison of the spatial resolution between current simulation and the validation case.

	Current Simulation	**Validation Case**
N around airfoil	364	308
N over the blade span/AR	55.25	33.67
N inside the boundary layer at midchord and $r/R = 0.8$	56 ($\delta = 1.5$ mm)	68($\delta = 1.85$ mm)
Max y+	0.55	0.9
$\Delta s/c$ at LE	0.133%	0.2%
max $\Delta s/c$ chord-wise	1.3%	1.43%
max $\Delta s/c$ normal to wall	4.6%	3.39%

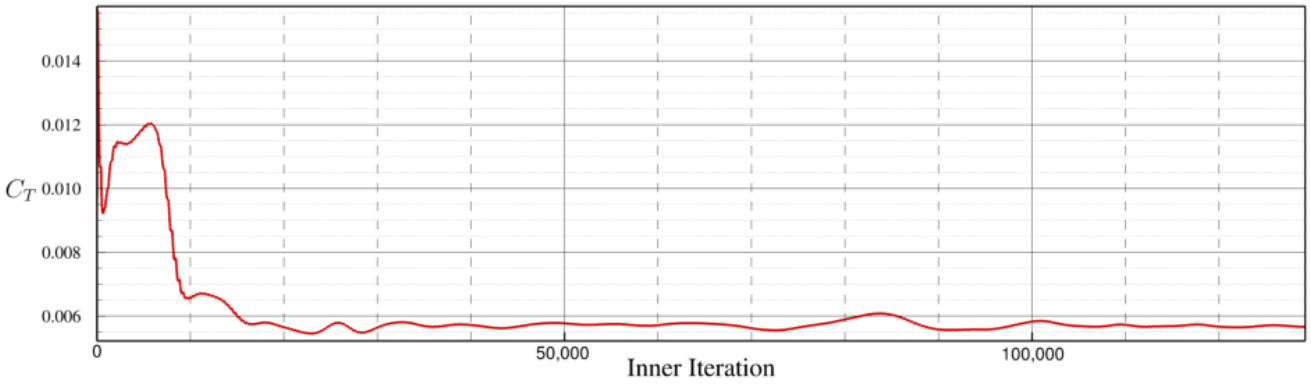

Figure 3.7: Thrust coefficient along inner iterations.

simulation is thus considered to give a close estimation of the flow phenomena on the pitching rotating blade.

3.3.2 Grid convergence study

In order to show the convergence of current grid, a coarse grid and a medium grid with the same strategy as described in Section 3.2.2 are created, and we list the spacing of each block for these grids in Table 3.8. $\overline{h}$ is the average of the edge length among

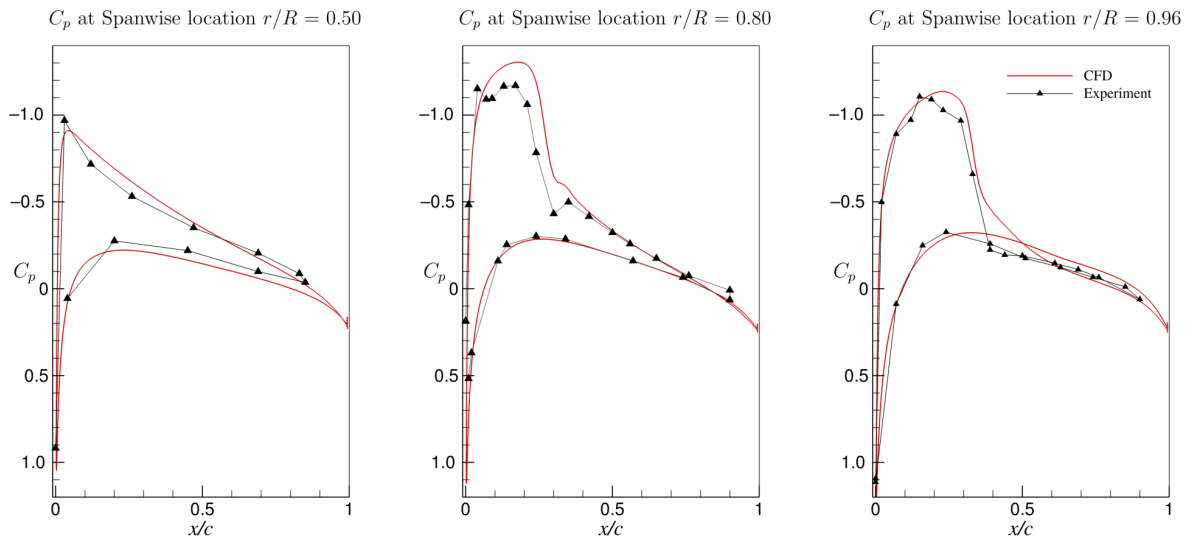

Figure 3.8: Pressure coefficient at different span-wise locations on the hovering rotor blade: comparison between numerical simulation with Spalart–Allmaras turbulence model and experiment result [120]).$C_p == \frac{p-p_\infty}{0.5\rho(\Omega R)^2}$.

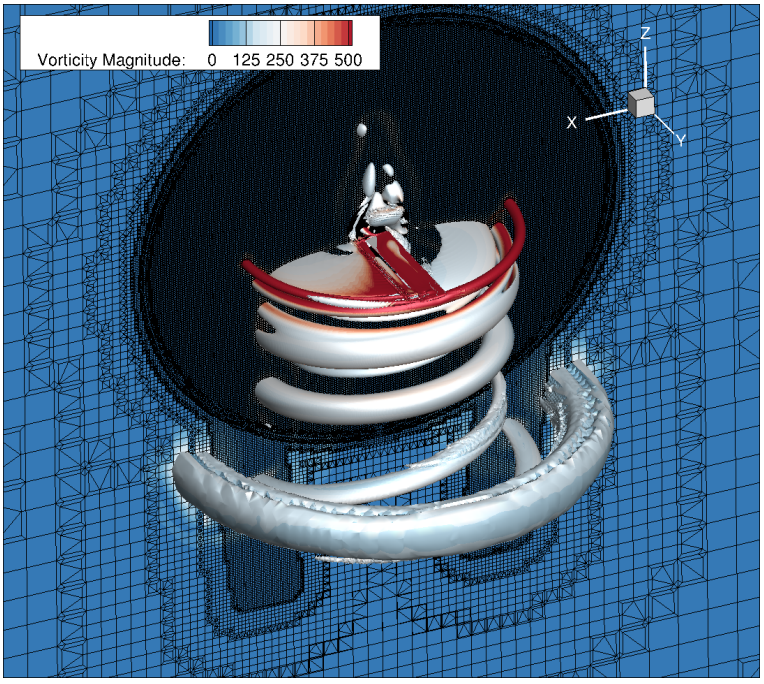

Figure 3.9: Iso-surface of Q-criterion ($Q = 5000\ \mathrm{s}^{-2}$) contoured with vorticity magnitude and super-positioning on y-sliced mesh.

the cells, and $\overline{V}$ is the average of the cell volumes. During coarsening the original fine grid, we keep the height of the first layer off the blade surface having the same value which satisfies $y+ = 1$. In addition, the number of connectors in three directions are all reduced according the level of the coarse grid. We present here only simulations with the Spalart–Allmaras turbulence model.

Table 3.8: Grid spacings and numerical results.

	Coarse Grid	**Medium Grid**	**Fine Grid**
Pitch Block	$\overline{h} = 5.74\%c$; $\overline{V}^{1/3} = 7.18\%c$	$\overline{h} = 2.82\%c$; $\overline{V}^{1/3} = 3.61\%c$	$\overline{h} = 1.40\%c$; $\overline{V}^{1/3} = 1.77\%c$
Rotating Block	$\overline{h} = 18.41\%c$; $\overline{V}^{1/3} = 14.33\%c$	$\overline{h} = 9.37\%c$; $\overline{V}^{1/3} = 8.80\%c$	$\overline{h} = 4.08\%c$; $\overline{V}^{1/3} = 3.73\%c$
Far-field Block	$\overline{h} = 1.32c$; $\overline{V}^{1/3} = 1.69c$	$\overline{h} = 0.52c$; $\overline{V}^{1/3} = 1.175c$	$\overline{h} = 0.22c$; $\overline{V}^{1/3} = 0.84c$
C_T	0.00782	0.00793	0.00791

We choose the average of cell edge lengths in pitch block as the spacing indicator, and following [121], we can obtain the exact value of a partial differential equation as:

$$f_{exact} = f_h + C \cdot h^p + \mathcal{O}(h^{p+1}) \tag{3.12}$$

where c is a constant and h is some measure of grid spacing, p is the order of convergence. We plot the grid convergence curve in Figure 3.10. The fitted curve of Equation (3.12) is $f = f_{h=0} - 1.251e - 5 \cdot h^{1.566}$, which means the grid has an order of convergence of 1.566. We have used a 2nd order scheme for both mean-flow flux and turbulence flux with a Spalart–Allmaras model; theoretically, this value should be 2. Based on Equation (3.12), the exact value of C_T is 0.007942, and the current grid has an error of 0.4%. We have compared the average C_T and C_{My} of the SA model and the Menter $k-\omega$ SST model, and found that C_T is exactly the same, while the averaged C_{My} for SA model is -0.001328, and, for $k-\omega$ model, it is -0.001676.

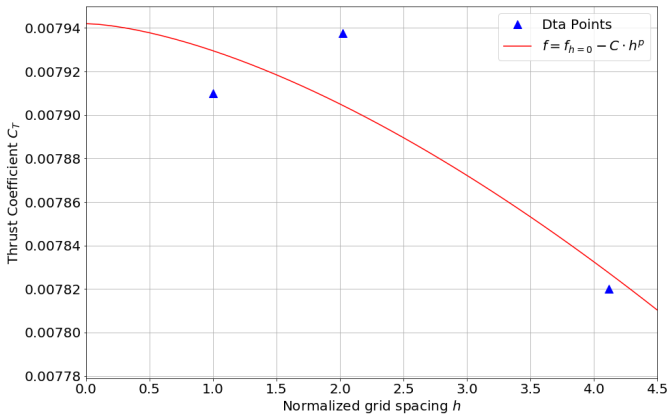

Figure 3.10: Grid convergence study with coarse, medium, and fine grids.

3.3.3 Periodicity and residual data

THE simulation is carried out first with 720 time steps per revolution ($\Delta\Psi = 0.5°$) for 2.5 revolutions, and then 1440 time steps/Rev ($\Delta\Psi = 0.25°$) for the subsequent revolutions. The inner iteration step is set to be at least 200 and maximum 400 to guarantee the density residual dropping two orders of magnitude. Furthermore, Cauchy convergence criteria are also implemented for saving computation time for each time step; if any of the force coefficients sequences $C_L(N)$, $C_D(N)$ and $C_{my}(N)$ in the last 30 inner iteration steps satisfies Cauchy convergence criteria, as described in Section 3.2.1.1, the inner iterations are considered converged for that time step. The residuals of the forces on blade, namely thrust F_z and pitch moment M_y, are plotted in Figure 3.11, where each circle represents the residual at an azimuth position after 400 inner iterations or reaches Cauchy convergence criteria. The ranges where no data points show up are where the residuals drop below 10^{-6}.

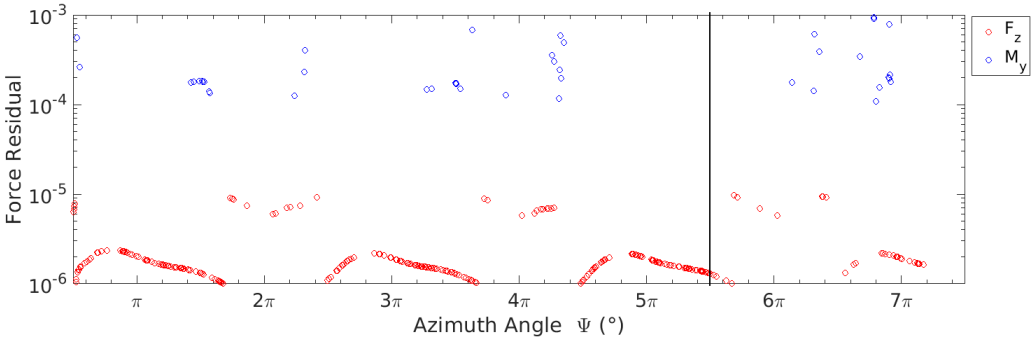

Figure 3.11: Force residual as a function of simulation time history expressed in azimuth angles.

The superposition of C_T and C_{My} in different revolutions is plotted in Figure 3.12, and we can see that, after the 3rd revolution, the forces have already converged to a good extent.

3.4 Analysis of the phenomenon

3.4.1 Determination of separation points

THE feature of dynamic stall is mainly the separation of the boundary layer, both at the trailing edge and the leading edge. Understanding, as well as modelling of dynamic stall need these separation points on the blade. Many methods, both Eulerian and Lagrangian, can be used to detect the flow separation in the unsteady flow. We present here pure Eulerian methods, the skin friction and shape factor criteria. The former theorem requiring wall shear stress is based on steady, laminar flows, but was recently extended by Haller et al. [122] to unsteady, turbulent and compressible flows; and the latter theorem requiring the near wall flow field is based on the boundary theory, and the separation criteria is proposed by Castillo et al. [123] as $H_{sep} = 2.76 \pm 0.23$

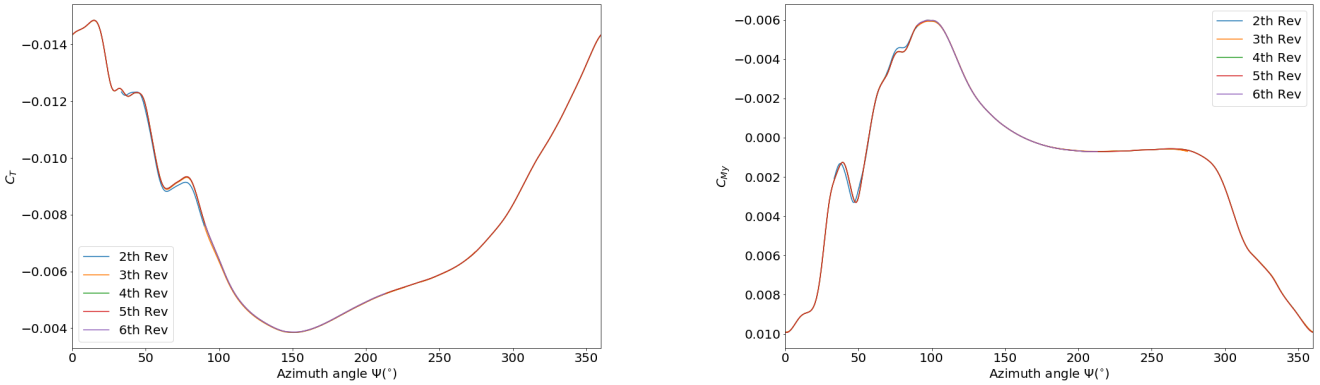

Figure 3.12: Superposition of force coefficients of different revolutions.

for two-dimensional turbulent flows. The rigorous skin friction criteria is followed to extract the instantaneous separation points on the blade and then present the shape factor criteria resultant separation points to show how good the velocity field can be used to evaluate the separation points.

According to Tobak et al. [124], the existence of a skin-friction line on a three-dimensional surface on which other lines converge is a necessary condition for the flow separation; and skin-friction line emerging from a saddle point indicates a global separation; otherwise, it is only a local separation. We do not distinguish here global or local separation, since we know that the leading-edge vortex that attached to the blade can also contribute to such a local separation, which is our interest as well. For the a blade section at a radial position, the aforementioned criteria can be expressed mathematically:

$$c_{fx} = 0; \ \frac{\partial c_{fx}}{\partial x} < 0. \tag{3.13}$$

Similarly, if $c_{fx} = 0$ and $\partial c_{fx}/\partial x > 0$, this is the point of attachment. Note that the stagnation point is also an attachment point, hence we have excluded this point in our algorithm.

Another separation criterion that can be used (see [98]) to detect separation in turbulence flows is based on the shape factor H_i, namely the ratio of the momentum thickness over displacement thickness of the boundary layer for a two-dimensional flow, as illustrated in Figure 3.13:

$$H_i = \int_0^\infty (1 - \frac{\rho(y)u(y)}{\rho_0 u_0})dy / \int_0^\infty \frac{\rho(y)u(y)}{\rho_0 u_0}(1 - \frac{u(y)}{u_0})dy. \tag{3.14}$$

Castillo et al. [123] stated that $H_{sep} = 2.76 \pm 0.23$ is characteristic of the boundary separation, yet they did not give a sufficient criteria. In order to imply the concept on our rotating blade, we transformed all the velocity to the blade-section-fixed coordinate and dealt with the velocity parallel to the airfoil at different radial sections, as shown in

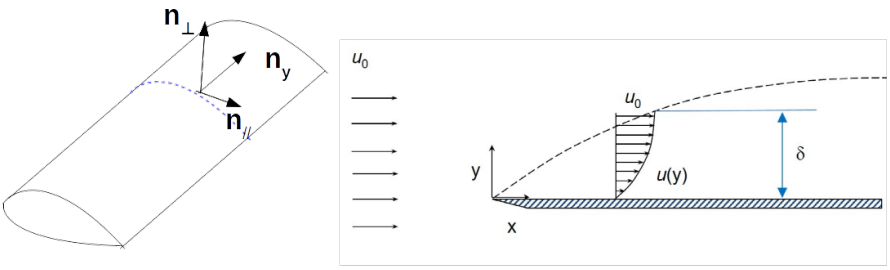

Figure 3.13: **left**: Illustration of coordinate system used to post-process shape factor; **right**: schematics of boundary layer over a flat plate.

Figure 3.13, along $n_{\parallel}$ direction. The flow along radial direction is not considered when analysing the shape factor since observing from the blade, and the main component of the flow is perpendicular to the leading edge of the blade. The outer edge of the boundary layer is treated as the location where the velocity reached its maximum along the $n_{\perp}$ direction. To determine how good this criterion can predict separation using only velocity field, we plot in Figure 3.14 the shape factor and the skin-friction in the x-direction at azimuth position $\Psi = 32.9°$. The lower bound $H_{sep} = 2.53$ shows quite a good agreement with the x skin-friction contour on the blade surface. However, Castillo et al. [123] showed only the correlation of separation and shape factor H in turbulent boundary layers, the utilisation of such criteria to detect separation should be considerably careful.

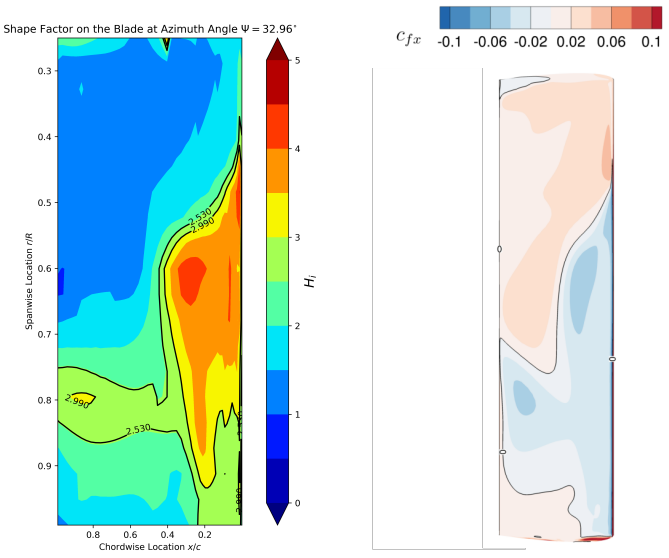

(**a**) (**b**)

Figure 3.14: (**a**) Shape Factor H_i on the upper surface at azimuth angle $\Psi = 32.9°$, two contour lines indicate the upper and lower bound of H_i value to determine the separation; (**b**) skin friction c_{fx} on the upper surface at azimuth angle $\Psi = 32.9°$, the 0 contour line showing the separation line.

3.4.2 Identification of the vortical coherent structure

In order to investigate the difference of the flow field of a pitching airfoil and a pitching-rotating blade, the vortex structures, or coherent structures need to be examined. Although there are many advanced identification criteria, we choose vortex cores, determined by Q-criterion as the coherent structure. Hunt et al [127] proposed the Q-criterion, defined by Chong et al. [128] in terms of the instantaneous velocity gradient tensor as:

$$Q = \frac{1}{2}((\nabla \cdot \mathbf{u})^2 - \nabla\mathbf{u} : \nabla\mathbf{u}^{\mathbf{T}}) = \frac{1}{2}((\nabla \cdot \mathbf{u})^2 + \|\mathbf{\Omega}\|_2^2 - \|\mathbf{S}\|_2^2). \tag{3.15}$$

Here $\mathbf{u}$ is the velocity vector and $\mathbf{S}$ is the strain rate tensor, $\mathbf{\Omega}$ is the rotation rate tensor. Positive Q identifies rotation-dominated regions of the flow or the connected regions of which show a coherent structure of vortices. Hence we use $Q = 5000s^{-1}$ as the core of the "rotating dominated region" or vortical core region of the flow field.

3.4.3 Analysis of the vorticity convection on the rotating system

Following Potter et al. [125], the rate of change of circulation within a control region can be expressed as in equation 3.16 by substitution of the Navier-Stokes equation:

$$\begin{aligned}\frac{\mathrm{d}\Gamma}{\mathrm{d}t} &= \oint_{\partial A} \frac{\partial \mathbf{u}}{\partial t} \cdot \mathrm{d}\mathbf{s} \\ &= -\iint_A [\nabla \times (\omega \times \mathbf{u})] \cdot \mathbf{n}_A \mathrm{d}A - \oint_{\partial A} \frac{\mathrm{d}p}{\rho} + \oint_{\partial A} {}^I\mathbf{a} \cdot \mathrm{d}\mathbf{s} + \oint_{\partial A} \nu\nabla^2\mathbf{u} \cdot \mathrm{d}\mathbf{s}.\end{aligned} \tag{3.16}$$

where, for the planar control region shown in Figure 3.15, $\mathbf{n}_A = \mathbf{e}_y$ is the surface normal to the plane of the control region, and ${}^I\mathbf{a}$ is the local acceleration in the inertial frame,

$${}^I\mathbf{a} = -2\mathbf{\Omega} \times \mathbf{u} - \dot{\mathbf{\Omega}} \times \mathbf{r} - \mathbf{\Omega} \times (\mathbf{\Omega} \times \mathbf{r}), \tag{3.17}$$

where the "$\dot{}$" is the time derivative. And $\mathbf{u}$ is the relative velocity to the rotating frame.

The line integration is performed on the boundaries, based on the body fixed coordinate system shown in Fig.3.16, boundary 3 at $x/c = -0.333$ and boundary 1 at $x/c = 0.333$, boundary 0 at $z/c = 0$ and boundary 2 at $z/c = -0.333$, whereas boundary 4 is directly on the blade surface. Since the grid geometry is not perfectly along the 5 line boundaries, the region for area integration, $\iint_{A'} f(x,z)\mathrm{d}A$ is adjusted so that the difference of $\oint_{\partial A} \mathbf{u} \cdot \mathrm{d}\mathbf{s}$ and $\iint_{A'} \omega_y \mathrm{d}A$ is kept small:

$$\epsilon = \left| \frac{\oint_{\partial A} \mathbf{u} \cdot \mathrm{d}\mathbf{s} - \iint_{A'} \omega_y \mathrm{d}A}{\oint_{\partial A} \mathbf{u} \cdot \mathrm{d}\mathbf{s}} \right| \leq 0.15\%.$$

With such adjusted integration area A', the difference of vorticity convection term $\oint(\omega \times \mathbf{u}) \cdot \mathrm{d}\mathbf{s}$ and $\iint_A [\nabla \times (\omega \times \mathbf{u})] \cdot \mathbf{n}_A \mathrm{d}A$ can be kept $\epsilon \leq 2\%$. However this error is still considered to be very large, and this will be one source of the error when the numerical evaluation of the vorticity transport is carried out.

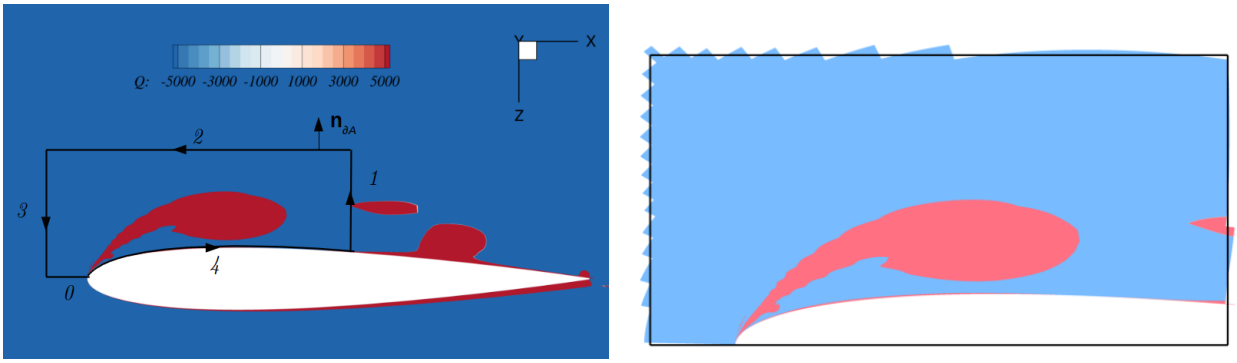

(a) (b)

Figure 3.15: Control region A for vorticity transport analysis. (a) The lines to abstract flow information and perform line integration; (b) the adjusted boundaries for area integration of flow variables.

Convective term

The first term of Equation 3.16 can be rewritten as:

$$\begin{aligned} &-\iint_A [\nabla \times (\omega \times \mathbf{u})] \cdot \mathbf{n}_A \mathrm{d}A \\ &= \iint_A \left\{ \left[\frac{\partial}{\partial x}(v\omega_x) + \frac{\partial}{\partial z}(v\omega_z) \right] - \left[\frac{\partial}{\partial x}(u\omega_y) + \frac{\partial}{\partial z}(w\omega_y) \right] \right\} \mathrm{d}A \\ &= \iint_A \left[-v\frac{\partial \omega_y}{\partial y} + (\omega_x \frac{\partial v}{\partial x} + \omega_z \frac{\partial v}{\partial z}) \right] \mathrm{d}A - \oint_{\partial A} (\mathbf{u} \cdot \mathbf{n}_{\partial A}) \omega_y \mathrm{d}s \end{aligned} \tag{3.18}$$

Compressible effect and diffusive term

And the second term should be handled very careful, since for the current compressible case, $\rho = g(x, z)$ and is not necessarily constant, hence it doesn't vanish automatically as is in an incompressible case; The third term will be examined later, and the fourth term, we consider the integration on the solid boundary part ∂A_{bound} and in-field part ∂A_{fluid}. Wu&Wu [126] showed the following relation on a boundary:

$$\rho(^{\mathbf{I}}\mathbf{a_s} - \mathbf{f}) + \nabla p - \nabla((\lambda + 2\mu)\nabla \cdot \mathbf{u}) + \nabla \times (\mu\omega) = \mathbf{0},$$

where $^{\mathbf{I}}\mathbf{a_s}$ is the surface acceleration in inertial coordinate system:

$$^{I}\mathbf{a}_s = \dot{\mathbf{\Omega}} \times \mathbf{r} + \mathbf{\Omega} \times (\mathbf{\Omega} \times \mathbf{r}),$$

$\mathbf{f}$ is the acceleration due to non-conservative force and λ is the second viscosity, which is an important parameter for irreversible resistance, like compression or expansion of the fluid, but can be neglected for $M < 2$. For our case, there is no non-conservative force, and $M < 2$, hence $\mathbf{f}$ and volume viscosity λ can be neglected. We can expand the

relation as:

$$^{\mathbf{I}}\mathbf{a_s} + \frac{\nabla p}{\rho} - 2\nu\nabla(\nabla\cdot\mathbf{u}) + \nu(\nabla\times\omega) - \frac{2(\nabla\cdot\mathbf{u})\nabla\mu}{\rho} - \omega\times\frac{\nabla\mu}{\rho} = \mathbf{0}.$$

although as will be shown later that $\nabla\cdot\mathbf{u}$ is small comparing to other terms, we still keep it in our equation.

$$\begin{aligned}\nu(\nabla\times\omega) &= \nu(\nabla\times(\nabla\times\mathbf{u}))\\ &= \nu(\nabla(\nabla\cdot\mathbf{u}) - \nabla^2\mathbf{u})\end{aligned}$$

Hence

$$^{\mathbf{I}}\mathbf{a_s} + \frac{\nabla p}{\rho} - \nu\nabla(\nabla\cdot\mathbf{u}) - \nu\nabla^2\mathbf{u} - \frac{2(\nabla\cdot\mathbf{u})\nabla\mu}{\rho} - \omega\times\frac{\nabla\mu}{\rho} = \mathbf{0}. \tag{3.19}$$

Inserting Equation3.19 into the last term of Equation3.16, we have:

$$\oint_{\partial A}\nu\nabla^2\mathbf{u}\cdot\mathrm{d}\mathbf{s} = \int_{\partial A_{fluid}}\nu\nabla^2\mathbf{u}\cdot\mathrm{d}\mathbf{s} + \int_{\partial A_{bound}}\left[^{\mathbf{I}}\mathbf{a_s} + \frac{\nabla p}{\rho} - \omega\times\frac{\nabla\mu}{\rho} - \nu\nabla(\nabla\cdot\mathbf{u}) - \frac{2(\nabla\cdot\mathbf{u})\nabla\mu}{\rho}\right]\cdot\mathrm{d}\mathbf{s}. \tag{3.20}$$

The control region A is fixed on the plate, hence both $\mathbf{\Omega}$ and $\mathbf{a}$ should be expressed in the body fixed coordinate system. Transformation of the vectors onto the non-inertial frame is the first step to evaluate the rate of change of circulation in the control region. In order to clarify the rotating-pitching system, the schematic sketch of the coordinate system is shown in Figure 3.16. A vector $^{I}\mathbf{v} = [v_X, v_Y, v_Z]$ in the inertial system can be expressed as $^{b}\mathbf{v} = [v_x, v_y, v_z]$ in the non-inertial system through two transformations:

1. A rotation of angle Ψ about the Z-axis of the inertial coordinate system due to the rotating angular velocity Ω, denoted as $[\mathbf{T_R}]$;
2. a rotation of the angle θ about the non-inertial $y-$axis due to pitching motion at angular velocity $\dot{\theta}$, denoted as $[\mathbf{T_p}]$.

And

$$^{b}\mathbf{v} = [\mathbf{T_p}][\mathbf{T_R}]^{I}\mathbf{v} \tag{3.21}$$

Considering the rotating and pitching case, the rotating angular velocity of the rigid body $^{I}\Omega_{Rotating} = \begin{pmatrix}0 & 0 & \Omega\end{pmatrix}^{\mathbf{T}}$, and the pitching angular velocity of the rigid body $\Omega'_{pitching} = \begin{pmatrix}0 & \dot{\theta} & 0\end{pmatrix}^{\mathbf{T}}$. The transformation matrix, based on the coordinate system depicted in Figure 3.16:

$$[\mathbf{T_R}] = \begin{pmatrix}1 & & \\ & -1 & \\ & & -1\end{pmatrix}\begin{pmatrix}\cos(\frac{\pi}{2}+\Psi) & \sin(\frac{\pi}{2}+\Psi) & 0\\ -\sin(\frac{\pi}{2}+\Psi) & \cos(\frac{\pi}{2}+\Psi) & 0\\ 0 & 0 & 1\end{pmatrix} = \begin{pmatrix}-\sin\Psi & \cos\Psi & 0\\ \cos\Psi & \sin\Psi & 0\\ 0 & 0 & -1\end{pmatrix} \tag{3.22}$$

and

$$[\mathbf{T_p}] = \begin{pmatrix}\cos\theta & 0 & \sin\theta\\ 0 & 1 & 0\\ -\sin\theta & 0 & \cos\theta\end{pmatrix} \tag{3.23}$$

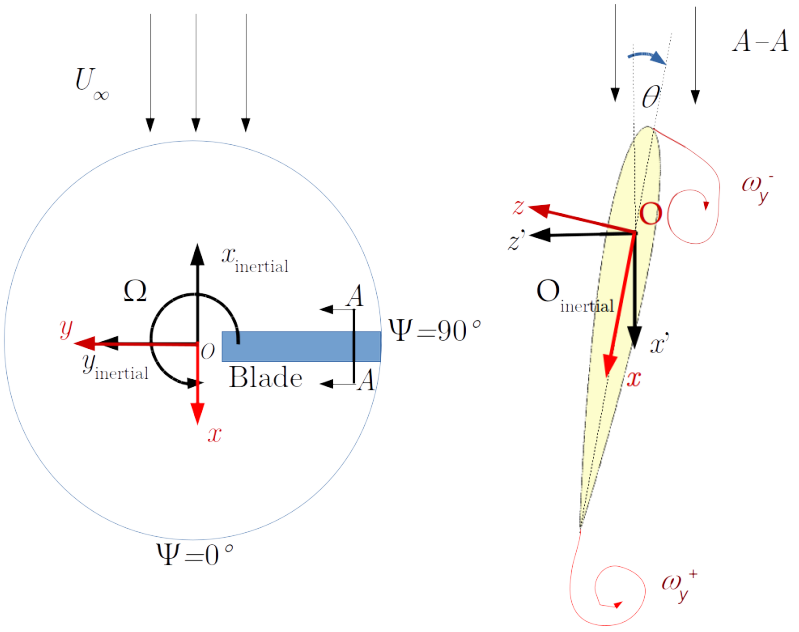

Figure 3.16: Schematic sketch of the coordinate system

Hence the angular velocity of the rigid body expressed in the body fixed coordinate system is:

$$
\begin{aligned}
{}^b\Omega &= [\mathbf{T_p}][\mathbf{T_R}]^I\boldsymbol{\Omega}_{Rotating} + [\mathbf{T_p}]\Omega'_{pitching} \\
&= \begin{pmatrix} \cos\theta & 0 & -\sin\theta \\ 0 & 1 & 0 \\ \sin\theta & 0 & \cos\theta \end{pmatrix} \begin{pmatrix} -\sin\Psi & \cos\Psi & 0 \\ \cos\Psi & \sin\Psi & 0 \\ 0 & 0 & -1 \end{pmatrix} \begin{pmatrix} 0 \\ 0 \\ \Omega \end{pmatrix} + \begin{pmatrix} \cos\theta & 0 & -\sin\theta \\ 0 & 1 & 0 \\ \sin\theta & 0 & \cos\theta \end{pmatrix} \begin{pmatrix} 0 \\ \dot\theta \\ 0 \end{pmatrix} \\
&= \begin{pmatrix} \Omega\sin\theta \\ \dot\theta \\ -\Omega\cos\theta \end{pmatrix}
\end{aligned}
\tag{3.24}
$$

Hence the angular acceleration:

$$
{}^b\dot{\boldsymbol{\Omega}} = \begin{pmatrix} \Omega\dot\theta\cos\theta \\ \ddot\theta \\ \Omega\dot\theta\sin\theta \end{pmatrix} \tag{3.25}
$$

For the current case, the pitch control is expressed in the rotated coordinate system as Equation 3.1. Insert Equation 3.1 into Equations 3.24, 3.25, we have:

$$
{}^b\boldsymbol{\Omega} = \begin{pmatrix} \Omega\sin\theta \\ \Omega(\theta_s\cos\Psi - \theta_c\sin\Psi) \\ -\Omega\cos\theta \end{pmatrix} \quad {}^b\dot{\boldsymbol{\Omega}} = \begin{pmatrix} \Omega^2\cos\theta(\theta_s\cos\Psi - \theta_c\sin\Psi) \\ -\Omega^2(\theta_s\sin\Psi + \theta_c\cos\Psi) \\ \Omega^2\sin\theta(\theta_s\cos\Psi - \theta_c\sin\Psi) \end{pmatrix}
$$

Acceleration Effect

The third term in Equation (3.16) can be re-written as:

$$\begin{aligned} {}^{b}\mathbf{a} =& 2\begin{pmatrix}\Omega_z v-\Omega_y w\\ \Omega_x w-\Omega_z u\\ \Omega_y u-\Omega_x v\end{pmatrix} \\ &+\begin{pmatrix}\dot{\Omega}_z y_0-\dot{\Omega}_y z_0\\ \dot{\Omega}_x z_0-\dot{\Omega}_z x_0\\ \dot{\Omega}_y x_0-\dot{\Omega}_x y_0\end{pmatrix} \\ &+\begin{pmatrix}-(\Omega_x\Omega_y y_0+\Omega_x\Omega_z z_0-\Omega_y^2 x_0-\Omega_z^2 x_0)\\ -(\Omega_x\Omega_y x_0+\Omega_y\Omega_z z_0-\Omega_x^2 y_0-\Omega_z^2 y_0)\\ -(\Omega_x\Omega_z x_0+\Omega_y\Omega_z y_0-\Omega_x^2 z_0-\Omega_y^2 z_0)\end{pmatrix} \end{aligned} \tag{3.26}$$

And for the surface acceleration in Equation (3.19):

$${}^{b}\mathbf{a}_s = -\begin{pmatrix}\dot{\Omega}_z y_0-\dot{\Omega}_y z_0\\ \dot{\Omega}_x z_0-\dot{\Omega}_z x_0\\ \dot{\Omega}_y x_0-\dot{\Omega}_x y_0\end{pmatrix}+\begin{pmatrix}\Omega_x\Omega_y y_0+\Omega_x\Omega_z z_0-\Omega_y^2 x_0-\Omega_z^2 x_0\\ \Omega_x\Omega_y x_0+\Omega_y\Omega_z z_0-\Omega_x^2 y_0-\Omega_z^2 y_0\\ \Omega_x\Omega_z x_0+\Omega_y\Omega_z y_0-\Omega_x^2 z_0-\Omega_y^2 z_0\end{pmatrix} \tag{3.27}$$

Note that in order to compare with the acceleration of the fluid, we have kept the same form of the expressions for the x,y,z components.

Coriolis effect

The Coriolis term only exists in the fluid area, and it has no contribution to the surface vorticity flux. Recall Equation(3.17), using Kelvin-Stokes theorem, note that $\begin{pmatrix}\Omega_x & \Omega_y & \Omega_z\end{pmatrix}$ is independent of x,y,z, we have:

$$\begin{aligned} \oint_{\partial A}\mathbf{a}_{Cor}\cdot\mathrm{d}\mathbf{s} &= \iint_A \nabla\times\mathbf{a}_{Cor}\cdot\hat{\mathbf{n}}\mathrm{d}A \\ &= \iint_A\left[\frac{\partial a_{Cor,z}}{\partial x}-\frac{\partial a_{Cor,x}}{\partial z}\right]\mathrm{d}A \\ &= \iint_A\left\{2\left[\frac{\partial(\Omega_y u-\Omega_x v)}{\partial x}-\frac{\partial(\Omega_z v-\Omega_y w)}{\partial z}\right]\right\}\mathrm{d}A \\ &= \iint_A\left[2\Omega_y\left(\frac{\partial u}{\partial x}+\frac{\partial w}{\partial z}\right)-2\left(\Omega_x\frac{\partial v}{\partial x}+\Omega_z\frac{\partial v}{\partial z}\right)\right]\mathrm{d}A \\ &= 2\Omega_y\oint_{\partial A}\mathbf{u}\cdot\mathbf{n}_{\partial A}\mathrm{d}s-\iint_A 2\left(\Omega_x\frac{\partial v}{\partial x}+\Omega_z\frac{\partial v}{\partial z}\right)\mathrm{d}A \end{aligned} \tag{3.28}$$

Here $\hat{\mathbf{n}}$ is $\begin{pmatrix}0 & 1 & 0\end{pmatrix}$

Centrifugal effect and centripetal effect

The centrifugal effect contributes to the fluid part $-\oint_{\partial A}\mathbf{a}_{cen}\mathrm{d}\mathbf{s}$ and the centripetal effect contribute to the surface part $\int_{\partial A_{bound}}\mathbf{a}_{s,cen}\mathrm{d}\mathbf{s}$. For centrifugal effect, similar to what

we did for the Coriolis term, using Kelvin-Stokes theorem, and note that $\begin{pmatrix}\Omega_x & \Omega_y & \Omega_z\end{pmatrix}$ is independent of x,y,z, we have:

$$\oint_{\partial A} \mathbf{a}_{cen} \cdot \mathrm{d}\mathbf{s} = \iint_A \nabla \times \mathbf{a}_{cen} \cdot \hat{\mathbf{n}} \mathrm{d}A = \iint_A \left(-\Omega_x\Omega_z + \Omega_x\Omega_z\right) \mathrm{d}A = 0$$

And for centripetal effect, the direction of the line integral is counter-clockwise, hence along the upper surface of the airfoil, the integral is from left to right, or the positive direction of x axis. Here we have a constrain for x and z, along the surface, $z/c = g(x/c + 1/4)$, $x \in [-c/4, 3c/4]$, where c is the chord length. With such constrain, we have $\mathrm{d}\mathbf{s} = \begin{pmatrix}dx & 0 & g'(x/c+1/4)dx\end{pmatrix}$. Insert this relation into the line integral of the surface vorticity flux, we have:

$$\begin{aligned}\int_{\partial A_{bound}} \mathbf{a}_{s,cen}\mathrm{d}\mathbf{s} &= \int_{\partial A_{bound}} a_{s,x}\mathrm{d}x + a_{s,z}g'(x_0/c+1/4)\mathrm{d}x \\ &= \int_{-c/4}^{c_1'} \left[\Omega_x\Omega_y y_0 + \Omega_x\Omega_z c g(x_0/c+1/4) - (\Omega_y^2+\Omega_z^2)x_0\right] \mathrm{d}x \\ &+ \int_{-c/4}^{c_1'} \left[\Omega_x\Omega_z x_0 + \Omega_y\Omega_z y_0 - (\Omega_x^2+\Omega_y^2) c g(x_0/c+1/4)\right] g'(x_0/c+1/4)\mathrm{d}x,\end{aligned} \tag{3.29}$$

with c_1' representing the position on the airfoil surface where the LEV boundary ends. Replace $x_0/c + 1/4$ with t and using $c1 \in [0, 1]$ to replace c_1', the first term of the right-hand-side (RHS) can be re-written as:

$$\begin{aligned}&\int_{-c/4}^{c_1'} \left[\Omega_x\Omega_y y_0 + \Omega_x\Omega_z c g(x_0/c+1/4) - (\Omega_y^2+\Omega_z^2)x_0\right] \mathrm{d}x \\ &\quad= \int_0^{c_1} \left[c\Omega_x\Omega_y y_0 + c^2\Omega_x\Omega_z g(t) - c^2(\Omega_y^2+\Omega_z^2)\left(t - \frac{1}{4}\right)\right] \mathrm{d}t \\ &\quad= c\Omega_x\Omega_y y_0 t\Big|_0^{c_1} + c^2\Omega_x\Omega_z \int_0^{c_1} g(t)\mathrm{d}t - c^2(\Omega_y^2+\Omega_z^2)\left(\frac{t^2}{2} - \frac{t}{4}\right)\Big|_0^{c_1}\end{aligned} \tag{3.30}$$

The second term of the RHS can be treated the same way:

$$
\begin{aligned}
&\int_{-c/4}^{c_1'} \left[\Omega_x\Omega_z x_0 + \Omega_y\Omega_z y_0 - (\Omega_x^2+\Omega_y^2)cg(x_0/c+1/4)\right] g'(x_0/c+1/4)\mathrm{d}x \\
&\quad= \int_0^{c_1} \left[c^2\Omega_x\Omega_z(t-\frac{1}{4}) + c\Omega_y\Omega_z y_0 - c^2(\Omega_x^2+\Omega_y^2)g(t)\right] g'(t)\mathrm{d}t \\
&\quad= \int_0^{c_1} \left[c^2\Omega_x\Omega_z(t-\frac{1}{4}) + c\Omega_y\Omega_z y_0 - c^2(\Omega_x^2+\Omega_y^2)g(t)\right] \mathrm{d}(g(t)) \\
&\quad= c^2\Omega_x\Omega_z\left(t-\frac{1}{4}\right)g(t)\Big|_0^{c_1} + c\Omega_y\Omega_z y_0 g(t)\Big|_0^{c_1} - c^2(\Omega_x^2+\Omega_y^2)g^2(t)\Big|_0^{c_1} - \\
&\quad c^2\int_0^{c_1}\left[\Omega_x\Omega_z + c^2(\Omega_x^2-\Omega_y^2)g'(t)\right]g(t)\mathrm{d}t \\
&\quad= c^2\Omega_x\Omega_z\left(t-\frac{1}{4}\right)g(t)\Big|_0^{c_1} + c\Omega_y\Omega_z y_0 g(t)\Big|_0^{c_1} - c^2(\Omega_x^2+\Omega_y^2)g^2(t)\Big|_0^{c_1} - \\
&\quad c^2\Omega_x\Omega_z\int_0^{c_1} g(t)dt + \frac{c^2}{2}(\Omega_x^2+\Omega_y^2)g^2(t)\Big|_0^{c_1}
\end{aligned}
\tag{3.31}
$$

Note that $g(0)=0$, insert Equation 3.30 and Equation 3.31 into Equation 3.29, we have:

$$
\begin{aligned}
\frac{1}{c^2}\int_{\partial A_{bound}} \mathbf{a}_{s,cen}\mathrm{d}\mathbf{s} &= \Omega_x\Omega_y\frac{y_0}{c}c_1 - (\Omega_y^2+\Omega_z^2)(\frac{c_1^2}{2}-\frac{c_1}{4}) \\
&+ \left[c_1 + \Omega_x\Omega_z(c_1-\frac{1}{4}) + \Omega_y\Omega_z\frac{y_0}{c}\right]g(c_1) - \frac{1}{2}(\Omega_x^2+\Omega_y^2)g^2(c_1).
\end{aligned}
\tag{3.32}
$$

When it is a flat plate without thickness, $g(t)=0$ and the terms with $g(c_1)$ vanish. These terms are actually the thickness effect. Depending on the value of c_1, this term has different values. The contribution of the centripetal force to the circulation change rate doesn't need the information of the flow field. Indeed, with only motion parameters and geometry parameters, one can calculate its contribution to the rate of change of the circulation.

Angular acceleration

The angular acceleration contributes to the fluid part $\oint_{\partial A}\mathbf{a}_{ang}\mathrm{d}\mathbf{s}$ and it contributes to the surface flux part $\int_{\partial A_{bound}}\mathbf{a}_{s,ang}\mathrm{d}\mathbf{s}$. For centrifugal effect, similar to what we did for the Coriolis and centrifugal term, using Kelvin-Stokes theorem, and note that $\begin{pmatrix}\Omega_x & \Omega_y & \Omega_z\end{pmatrix}$ is independent of x,y,z, we have:

$$
\oint_{\partial A}\mathbf{a}_{ang}\cdot\mathrm{d}\mathbf{s} = \iint_A \nabla\times\mathbf{a}_{ang}\cdot\hat{\mathbf{n}}\mathrm{d}A = \iint_A\left(-2\dot{\Omega}_y\right)\mathrm{d}A
$$

Together with Equation 3.25, we have:

$$\begin{aligned}\frac{\partial \Gamma}{\partial t} = &\cdots + \oint_{\partial A} \mathbf{a}_{ang} \cdot \mathrm{d}\mathbf{s} + \cdots \\ &\cdots + \iint_A \left(-2\dot{\Omega}_y\right) \mathrm{d}A + \cdots .\end{aligned}$$

with $\iint_A \mathrm{d}A = 0.00463$, this term is a pure pitching motion induced effect. It represents the development of an apparent solid-body rotation in the presence of a time-varying pitch angular velocity ($\dot{\Omega}_y$).

Similar to the centripetal effect, we evaluate the angular acceleration on the surface of the blade.

$$\begin{aligned}\int_{\partial A_{bound}} \mathbf{a}_{s,ang} \cdot \mathrm{d}\mathbf{s} &= \int_{\partial A_{bound}} a_{s,x}\mathrm{d}x + a_{s,z} g'(x_0/c + 1/4)\mathrm{d}x \\ &= c^2 \int_{-c/4}^{c_1'} \left[\dot{\Omega}_z \frac{y_0}{c} - \dot{\Omega}_y g\left(\frac{x_0}{c} + \frac{1}{4}\right)\right] \mathrm{d}(\frac{x}{c}) + c \int_{-c/4}^{c_1'} \left[\dot{\Omega}_y x_0 - \dot{\Omega}_x y_0\right] g'\left(\frac{x_0}{c} + \frac{1}{4}\right) \mathrm{d}(\frac{x}{c}) \\ &= c^2 \int_0^{c_1} \left[\dot{\Omega}_z \frac{y_0}{c} - \dot{\Omega}_y g(t)\right] \mathrm{d}t + c^2 \int_0^{c_1} \left[\dot{\Omega}_y \left(t - \frac{1}{4}\right)\right] \mathrm{d}(g(t)) \\ &= c^2 \dot{\Omega}_z \frac{y_0}{c} t \Big|_0^{c_1} - c^2 \dot{\Omega}_y \int_0^{c_1} g(t)dt + c^2 \left[\dot{\Omega}_y \left(t - \frac{1}{4}\right) - \dot{\Omega}_x \frac{y_0}{c} g(t) \Big|_0^{c_1}\right] - c^2 \dot{\Omega}_y \int_0^{c_1} g(t)\mathrm{d}t \\ &= -c^2 \dot{\Omega}_y \int_0^{c_1} g(t)\mathrm{d}t + c^2 \dot{\Omega}_z \frac{y_0}{c} c_1 + c^2 \left[\dot{\Omega}_y \left(c_1 - \frac{c}{4}\right) - \dot{\Omega}_x \frac{y_0}{c}\right] g(c_1)\end{aligned} \tag{3.33}$$

Re-evaluation of the vorticity transport function

Insert Eq. 3.18 and Eq. 3.19 into Eq. 3.16, note that the line integral of $\partial A = \partial A_{fluid} + \partial A_{surface}$, the terms that influence the vorticity variation can be rewritten as:

$$
\begin{aligned}
\frac{\partial \Gamma}{\partial t} = & \iint_A \left[-v\frac{\partial \omega_y}{\partial y} + \left(\omega_x \frac{\partial v}{\partial x} + \omega_z \frac{\partial v}{\partial z} \right) \right] \mathrm{d}A && \text{Spanwise convection and Vorticity tilting} \\
& - \oint_{\partial A} (\mathbf{u} \cdot \mathbf{n}_{\partial A}) \omega_y \mathrm{d}s && \text{Planer vorticity variation} \\
& - \int_{\partial A_f} \frac{\nabla p}{\rho} \cdot \mathrm{d}\mathbf{s} && \text{Compressible effect} \\
& + \oint_{\partial A} \mathbf{a}_{Cor} \cdot \mathrm{d}\mathbf{s} && \text{Coriolis effect} \\
& + \int_{\partial A_f} \mathbf{a}_{cen,ang} \cdot \mathrm{d}\mathbf{s} && \text{Centrifugal and angular acceleration effect} \\
& + \int_{\partial A_f} \nu \nabla^2 \mathbf{u} \cdot \mathrm{d}\mathbf{s} && \text{diffusion in fluid} \\
& - \int_{\partial A_s} \omega \times \frac{\nabla \mu}{\rho} \cdot \mathrm{d}\mathbf{s} && \text{surface viscous effect}
\end{aligned}
\tag{3.34}
$$

Here the acceleration terms are cancelled out on the surface, the contribution of the surface variables to the total circulation change of the control volume comes only from the surface term in the planar variation $\int_{\partial A_s} (\mathbf{u} \cdot \mathbf{n}_{\partial A}) \omega_y \mathrm{d}s$ and the viscous term $\int_{\partial A_s} \nu \nabla (\nabla \cdot \mathbf{u}) \cdot \mathrm{d}\mathbf{s}$.

3.5 Lower order Model for dynamic stall on a rotating blade

Based on the blade element theory, the Beddoes-Leishman dynamic model [65] can be integrated into a three-dimensional model to evaluate the lower order model. As is shown in Figure 3.17, the lower-order model consists of three main processes, namely the estimation of the inflow field, the calculation of the unsteady loads of two-dimensional airfoil, and the correction of three-dimensional effect based on Prandtl's lifting line theory [129]. We are going to provide improvement directions for such a lower-order model based on the numerical investigation.

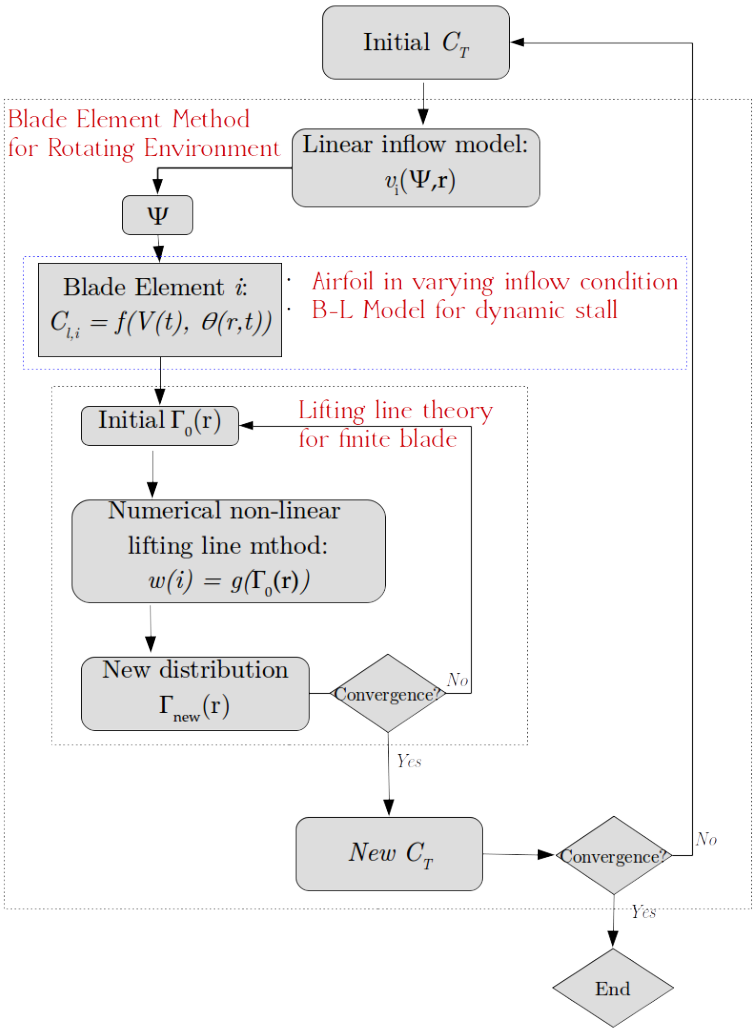

Figure 3.17: Schematics of the modelling process: dynamic stall events on a single rotating blade.

4 General characteristic of dynamic stall on the rotating system

4.1 Force and moment

THERE is a marginal difference in both thrust and pitching moment coefficients in terms of the maximum values as shown in Figure 4.1. The stall event occurs later for the $k-\omega$ SST turbulence model, and the pitching-up moment in the post-stall phase is relatively smaller. This indicates differences of the detailed fluid structure in the stall regime; this will be studied in detail in the future but not within the scope of current study. Nevertheless, the overall trends of the curves are similar to each other, and we are using the numerical results of the SA turbulent model to illustrate the dynamic stall events on the rotating-pitching blade.

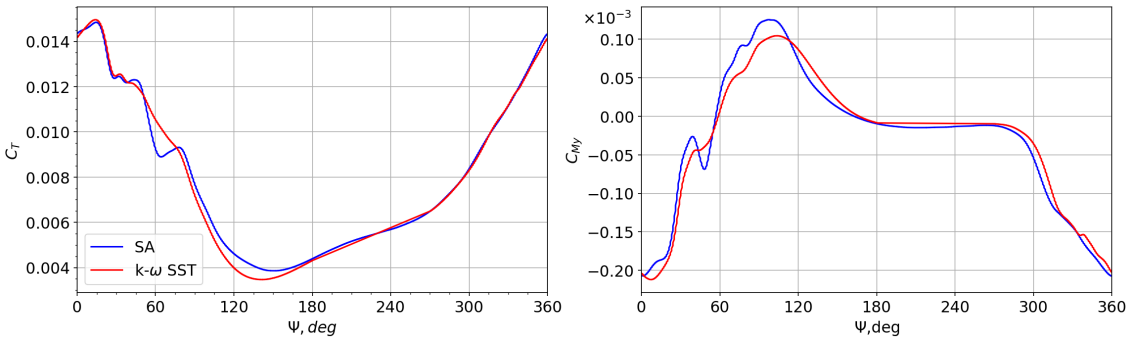

Figure 4.1: Comparison of thrust and pitching moment coefficients of the blade within one revolution by different turbulence models: Spalart–Allmaras (SA) and the $k-\omega$ SST turbulence model.

Sectional force coefficients are shown in Figure 4.2 at radial locations $r/R = 0.607$, 0.785 and 0.928. The plot shows an apparent difference between radial locations in both stall onset time and stalled value. Both C_nM^2 and C_mM^2 show an earlier stall for outboard locations. However, the extreme C_nM^2 and stalled value of C_mM^2 do not take place at the outermost location. Both thrust and pitching moment curves in the post-stall phase oscillate distinguishably compared to their inboard counterparts.

Figure 4.3 is the rotor map of both sectional normal force and moment coefficients. Force coefficients are non-dimensionalized by sound speed. The maximum C_nM^2 appears in the region $0.6 < r/R < 0.85$, $350° < \Psi < 35°$, which is in the pitching-down phase. While the relative high value (orange area) begins at $\Psi = 300°$, $\theta = 21.89° \uparrow$ (pitching up) and remains until $\Psi = 60°$, $\theta = 12.21° \downarrow$ (pitching down). The negative normal force

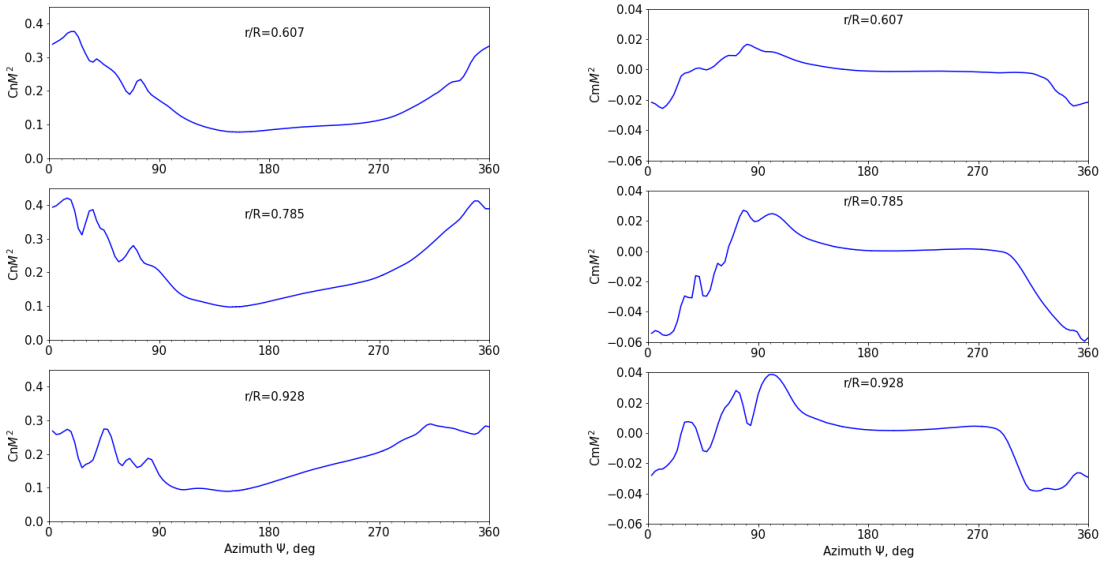

Figure 4.2: Sectional force coefficients at selected radial locations, $r/R = 0.607$, 0.785 and 0.928. (**a**): sectional normal force coefficient C_nM^2; (**b**): sectional pitch moment coefficient C_mM^2.

also exists near blade tip at azimuth angle $330° < \Psi < 30°$, which is a result of the tip vortex; it appears at the blade root as well, which is the attributed reverse flow region and the strong root whirl flow, the latter a pure result of the abrupt cut of the blade model at the root. The minimum C_mM^2 (pitch down moment) appears at $r/R = 0.72$, $\Psi = 20°$, which is in the pitching-down phase well beyond the maximum pitch angle. The relatively small value (blue region) starts from $\Psi = 300°$ and ends near $\Psi = 30°$, which is consistent with the change of normal force, and this indicates that the dynamic stall occurs in this region. The maximum C_mM^2(pitching-up moment) appears at blade tip, $90° < \Psi < 110°$, where a normal shock exists on the suction surface, see Figure 4.4 . $C_m = 0$ is contoured with a bold line in the rotor map. The rugged line shows the recovery of C_m occurs inboard first while very late at radial locations $0.6 < r/R < 1$.

4.2 Vortex structure

4.2.1 Leading edge vortex

SINCE dynamic stall events are closely associated with the vortex generating and shedding on the upper surface of a blade, we show the vortex structures on the rotating blade at different azimuth angles in Figure 4.5.

An Ω-shaped vortex structure is visible in the snapshots (b) $\Psi = 300°, \theta = 21.89° \uparrow$ (c) $\Psi = 315°, \theta = 22.65° \uparrow$, which is similar to the observations for a pitching finite wing by Kaufmann [130], and also similar to what [131] called the Λ-type arch vortex. A

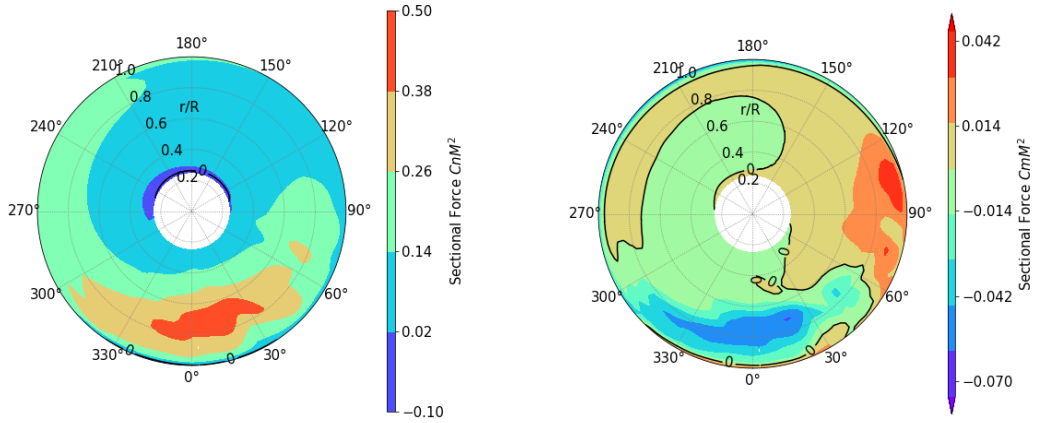

(a) (b)

Figure 4.3: Rotor map of sectional force coefficients. (**a**): C_nM^2 sectional normal force coefficient normalised by sonic speed; (**b**): C_mM^2 sectional pitch moment coefficient.

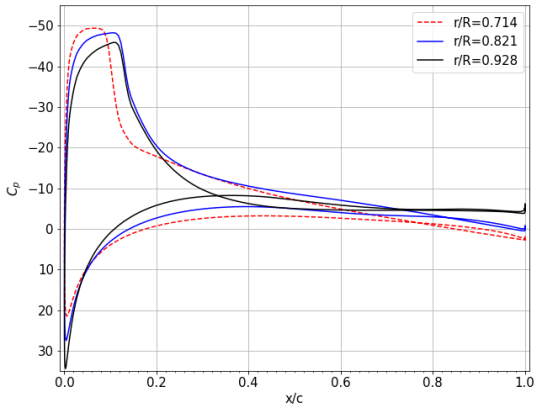

Figure 4.4: Pressure coefficient of a slice on the blade at radial position $r/R = 0.714$, 0.821 and 0.928, azimuth angle $\Psi = 90°$.

similar observation is also reported by [97]. Unlike on a pitching finite wing, as soon as the Ω-shape vortex is shed, the leading edge vortex (LEV) comes into interaction with the blade tip vortex to a great extend, and even an inclined arch vortex appears at the tip, see (e) $\Psi = 345°, \theta = 22.1° \downarrow$.

4.2.2 Tip vortex

In order to see the interaction of the leading-edge vortex and the tip vortex, we take slices at several chord-wise locations near the tip region ($0.94 < r/R < 1.125$), and integrate ω_x,$\pm\omega_y$ in this region where $\omega_x > 0$, which is the main contribution to the tip vortex in cases that are free from strong interaction. The circulation in the y-direction

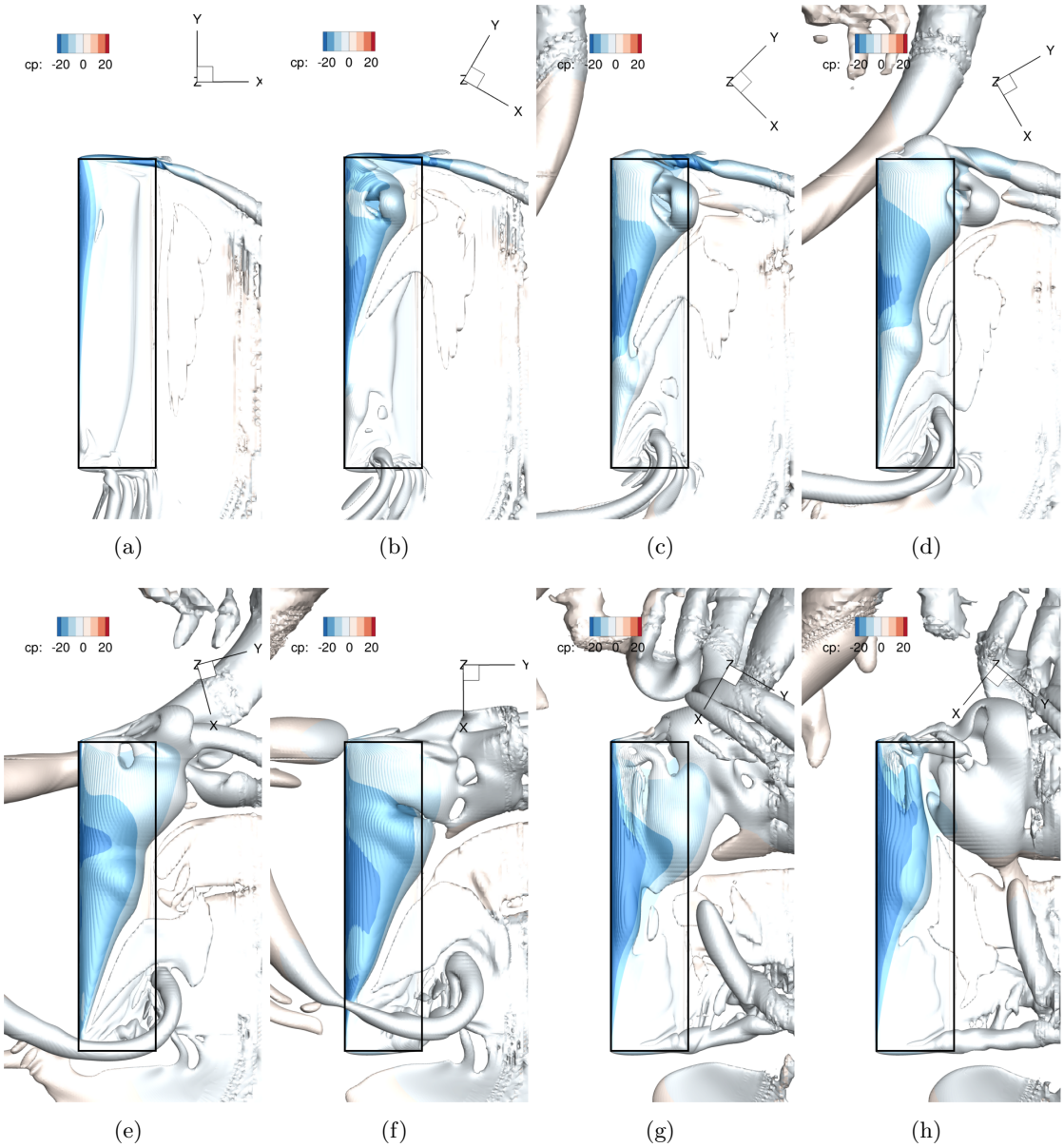

Figure 4.5: Vortex structure shown by iso-surface of Q criterion ($Q = 5000\ s^{-2}$) shaded by pressure coefficient cp referenced to forward flight speed. For each subplot, top: blade tip, bottom: blade root. The blade border is shown with the black rectangle. Azimuth positions: Ψ = (**a**) 270°; (**b**) 300°; (**c**) 315°; (**d**) 330°; (**e**) 345°; (**f**) 0°; (**g**) 30°; (**h**) 39°. The inertial coordinate is plotted here.

indicates the mixture of LEV in the tip vortex region. This result is plotted in Figure 4.6 with selected azimuth angles.

The consequent strong interaction of the LEV and tip vortex dominates the flow behavior of the post-stall phase. There are mainly four stages in this phase, symbolized by the shedding of LEV at the tip area. The 1st stage begins at $\Psi = 300°$, when the LEV accumulates at the blade-tip's leading-edge, which is shown as the increasing integration of negative y circulation $-\Gamma_y$; the LEV starts shedding at $\Psi = 317°$ as the peak of $-\Gamma_y$ moves rearward, and at the place where this peak locates, the circulation in the x-direction Γ_x in the tip region is also relatively larger. As the separated DSV moves downstream and outboard, the tip vortex at $x/c = 0.957$ is elevated and distorted. Alongside the rearward movement of $-\Gamma_y$, $+\Gamma_y$ grows in the vicinity of the tip surface. This explains why the negative C_n exists at the tip region on the rotor map of $C_n M^2$. The second stage begins at $\Psi = 0°$ when the previous main DSV is transported off of the trailing edge; another LEV is accumulated at the leading edge. In this stage, the tip vortex at $x/c = 0.952$ is no longer obvious, but the net circulation in the x-direction increases. This means, in the tip region that there exists a more diffused vorticity field rather than the conventional concentrated structure. As the LEV grows over the chord, the tip vortex is not apparent; nevertheless, it increases continuously in this area. From this time on, the LEV sheds and entrains the tip vortex, forming a large separation region over the tip area. Finally, $\Psi = 35.96°$ marks the end of previous shedding of LEV and the beginning of the next shedding of LEV at the tip area. A reversely rotating tip vortex is generated beneath the mixture layer of the separated leading-edge vortex and tip vortex at $x/c = 0.952$. In the near wake, the tip vortex locates more outboard compared to the 1st stage, and a pair of counter rotating vortices is obvious. At azimuth $\Psi = 53.96°$, the interaction of LEV and tip vortex begins to disentangle at $x/c = 0.418$. Another growing and shedding of LEV at the tip area is observed, but in this stage there is no strong interaction with the tip vortex. It enters the recovery stage.

The interaction of the leading edge vortex with the tip vortex represents three important features:

- The leading-edge vortex is not "pinned" by the tip vortex, which is contrary to the observations for a pitching wing;
- There is a strong correlation of circulation in the x-direction and the chord-wise location of DSV. This can be explained as a result of lower pressure created by the DSV, which induced higher velocity around the tip.
- The concentrated tip vortex is entrained into LEV during the pitching-down phase, and a pair of counter-rotating vortices is observed in the near wake of the blade.

Chang et al. [133] measured the tip wake in the near field of an oscillating wing; he discovered the hysteresis behaviour of the tip vortex, and a more diffused tip vortex during a down-stroke compared with the up-stroke. Current numerical simulation complies with the observation of pitching wing.

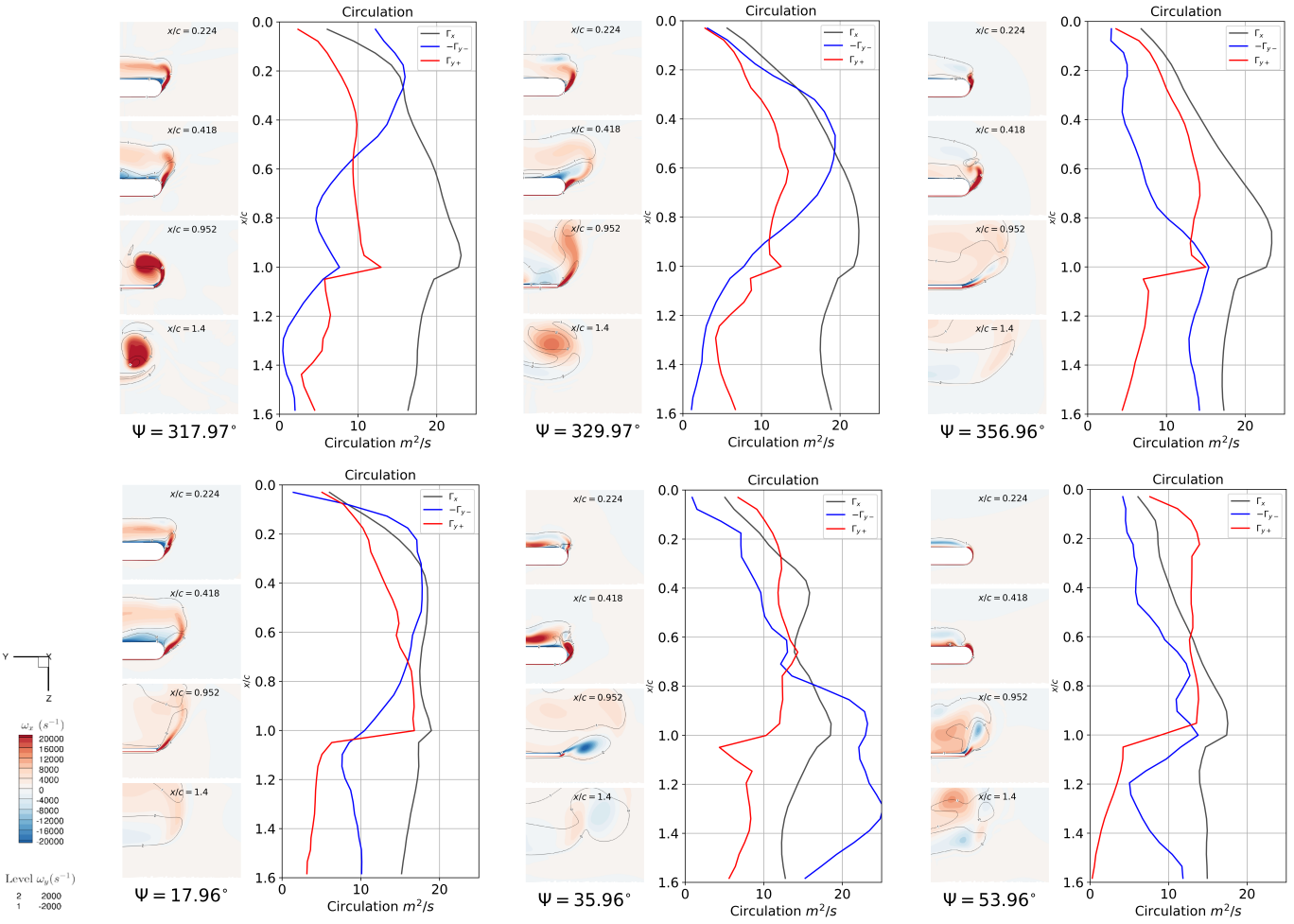

Figure 4.6: Snapshots of the flood contour of vorticity field ω_x and the contour of ω_y in blade tip area ($0.94 < r/R < 1.125$) at different chord-wise sections; The circulation $\Gamma_{i\pm} = \iint_S \pm\omega_i dA$, where S is the tip region where $\omega_x > 0$, $i = (x, y)$. Azimuth positions: $\Psi =$ (**a**) 318°; (**b**) 330°; (**c**) 357°; (**d**) 18°; (**e**) 36°; (**f**) 54°.

4.2.3 Swell structure and vortex cores

THE location of vortex cores over the blade is plotted in Figure 4.10, which is extracted based on the eigenmodes of the velocity vectors [132].

Another significant feature shown in Figure 4.5 is the conical structured LEV on the rotating blade, which is very similar to what Ozen [134] shows on a rotating plate. This conical shaped structure is treated as a more stable LEV, "pinned" at the leading edge [69], if we look at slices taken along the chord-wise direction. Ellington [69] explains that the stability of LEV on rotating wing is due to the span-wise flow, which transports vorticity to the tip and inhibits the growth of LEV, hence the critical circulation beyond which the LEV will detach from the leading edge is not reached. In addition, this can

explain the phenomenon observed by [51], who concluded that vortex evolution varies with radial positions on the blade, namely, at some locations, LEV sheds into dynamic stall vortex (DSV), while, in other places, only a secondary vortex is generated. When the phenomenon inspected from a three-dimensional perspective, this conclusion is just an incomplete description of the Ω-shaped vortex outboard and the conical vortex structure inboard. That is to say, the detached DSV is rather a part of the arch vortex, which attaches to the blade surface with two "legs"; and this is due to the stability of the conical LEV structure in which no DSV is shed and observed inboard.

The special phenomenon of the rotating and pitching blade is the vortex generated inboard which can be seen in Figure 4.5b–f ($\Psi = 300° \sim 360°, \theta = 21.89° \uparrow\sim 20.92° \downarrow$) as a swelling part within the conical LEV region inboard the blade, and it appears on different radial locations and grows in size while moving outboard. This swell structure creates a relative higher pressure on the blade, as is shown in Figure 4.7 where a shallow grey area at $r/R = 0.4875$ is encompassed by a darker area. This is a result of the alleviated LEV, when compared with the one at $r/R = 0.625$, where the LEV stays close to the upper surface of the blade. From the x plane slice, one can easily identify the detachment of the vortex structure. This structure corresponds to what Raghav et al. [51] observed on their retreating blade that inboard LEV didn't generate a DSV but a secondary vortex. As the swell structure moves outboard, it carries the vorticity that arched away from the surface and hence at that radial location no shedding of the LEV occurs. The span-wise flow also contributes to the outboard moving of the swell structure.

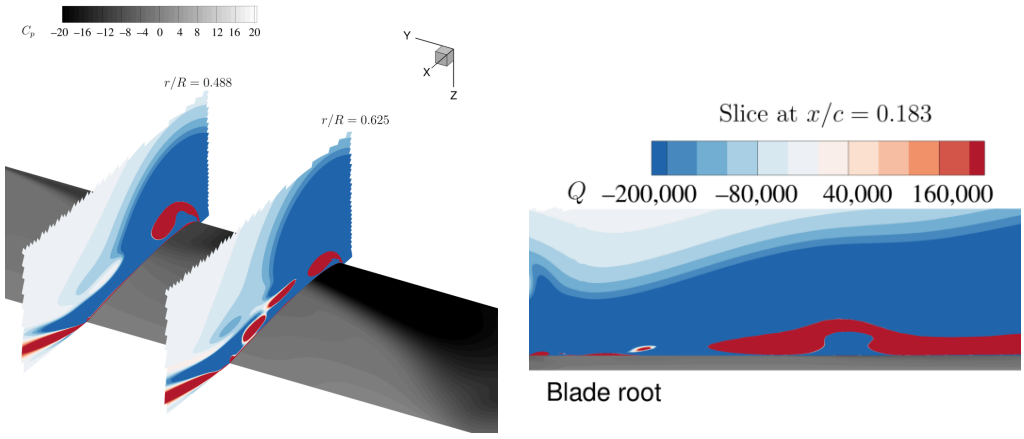

Figure 4.7: The swell structure on the blade, represented with x and y slices. **Left**: slices at $r/R = 0.488$ and 0.625; **Right**: slice at $x/c = 0.183$.

This swell structure seems to be a result of the Coriolis force on the rotating blade at first thought, but we carefully examined the pressure force and the Coriolis force of the conical LEV slices at several spanwise locations and found out that the Coriolis force is too small to affect the vortex structure. The swell structure shown in Figure 4.5 exists at $\Psi = 270°$ near the root corner, prior to the formation of the Ω-type vortex. Indeed, the structure appears even earlier in this simulation at $\Psi = 245°$, but it doesn't

have any obvious effect on the pressure distribution on the blade's surface. The growth, however, does have an impact on the pressure distribution later on as shown in Figure 4.7. The reason why this structure appears first inboard is still unclear. Smith et al. [78] mentioned that a greater magnitude inertial Coriolis force that pulls the LEV core away from the leading edge exists when the a rotating wing is positioned closer to the rotation axis, which might help to explain the phenomena. We evaluated forces in the x-direction on the slices of the vortex structure, as shown in Figure 4.8a. Following the divergence theorem, we evaluated the pressure force on the slices of the vortex core:

$$\Delta F_p = \oint_C p d\vec{s} = \iint_S \nabla p dA \tag{4.1}$$

$$\Delta F_{px} = \iint_S \frac{\partial p}{\partial x} dA \tag{4.2}$$

The Coriolis force exerted on the vortex core can be evaluated as $\Delta F_{Cor} = \iint \rho \mathbf{a_{Cor}} dA$. The ratio of the Coriolis force to the pressure force is plotted in Figure 4.8b. At blade root, this value in y-direction increases from 0.1 to 12, and it keeps a value around 1 for non-dimensional radial locations where $r/R < 0.6$. The maximum value is at the brink of the swell structure, which seems that the Coriolis force is an important factor that balances the swell structure as it moves outboard. This value in x- and z-directions increases first to and then show a continuously decreasing trend as r/R increases. What the plot shows is consistent with Smith's [78] argument and the Coriolis force plays indeed an important role on the rotating system. It is reasonable to explain the emergence of the swell structure as a result of the relative larger $F_{Cor,x}$ and $F_{Cor,z}$ at root region. As shown in Fig. 4.9, the Coriolis force in x-direction pulls the vortex towards trailing-edge and the force in z-direction lifts the core upwards. And the Coriolis force in y-direction drives the structure moving outboard.

Since the position of the swell structure influences the sectional pitching moment, we thereby extracted the vortex cores and plot its x position against azimuth angle Ψ in Figure 4.10. The lighter color represents an aft position of the vortex core, which results in a negative pitching moment component. In Figure 4.2 at a radial location $r/R = 0.607$, $\Psi = 340°$, there is a small kink on both $C_n M^2$ and $C_m M^2$ curves; In Figure 4.10, we see that, at $\Psi = -21°$(or 339°), the vortex core at $r/R = 0.62$ is located well beyond the line of the nearby LEV cores. The lighter color formed an edge in the contour map that represents the trajectory of the swell structure as it moves afterward as well as outward. We define this ridge as the position of the swell structure $(r/R)_{swell}$ when (1) $\partial(x/c)_{VortexCores}/\partial(r/R) = 0$, (2) $\partial^2(x/c)_{VortexCores}/\partial^2(r/R) < 0$, in radial locations (3) $(r/R) < 0.8$, where $(x/c)_{VortexCores}$ is the scatter plot of the normal projection of the vortex cores on the blade in Figure 4.10. This value $(r/R)_{swell}$ can be estimated as a quasi-uniform-acceleration movement on the blade:

$$(r/R)_{swell} = \frac{1}{2} a^{\star}_{swell} \Delta\Psi^2 + \eta\mu \cos(\Psi)\Delta\Psi + r_0. \tag{4.3}$$

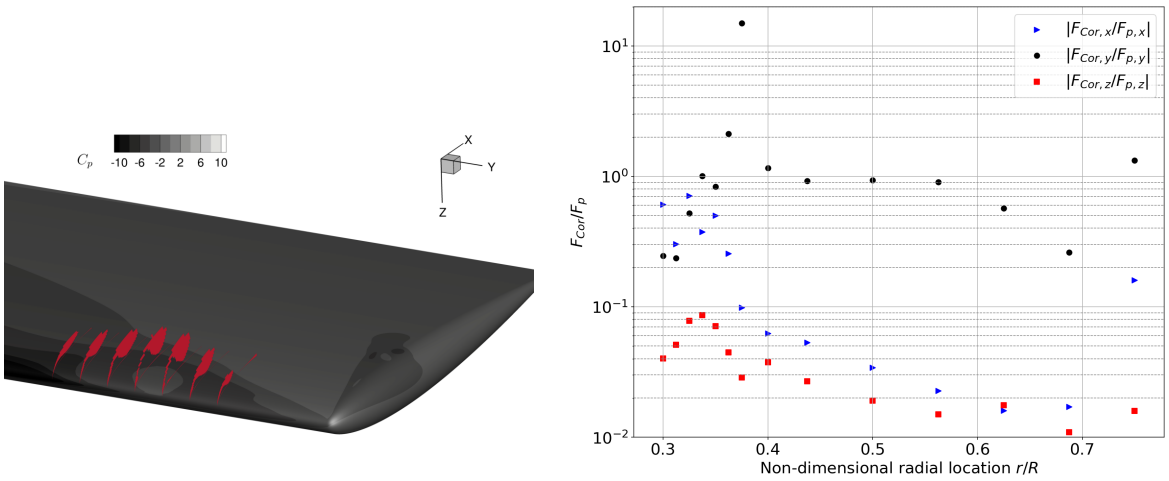

(**a**) (**b**)

Figure 4.8: Comparison of the pressure force and the Coriolis force in vortex cores. (**a**) area of integration, where $Q > 0$; (**b**) ratio of Coriolis force and pressure force in 3 directions $\Delta F_{Cor}/\Delta F_{px}$.

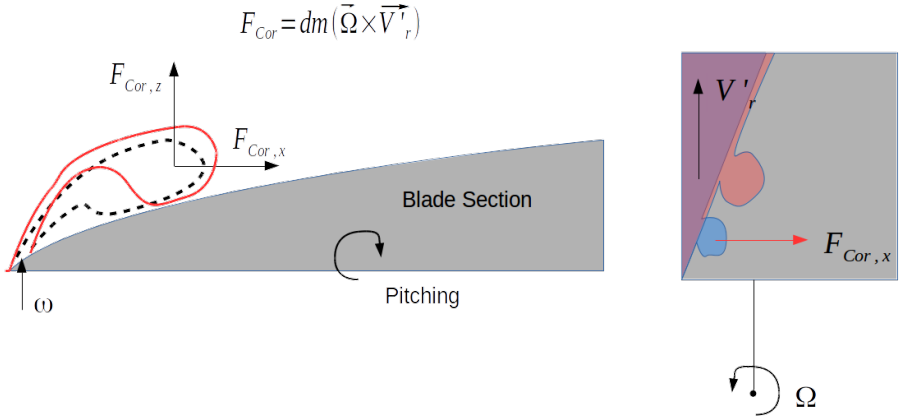

Figure 4.9: Schematics of the generation of the swell structure near the root of the blade.

The first term is the centrifugal effect, the second term is the contribution of the yawing effect, with η representing a lower flow speed in vicinity of the blade's upper surface, and the third term is the initial position of this vortex structure on the blade. In our case, the white dotted line in Figure 4.10 gives an approximation of the trajectory using the expression mentioned above for the movement, and $a^{\star}_{swell} = 0.25, \eta = 0.8, r_0 = 0.3426$.

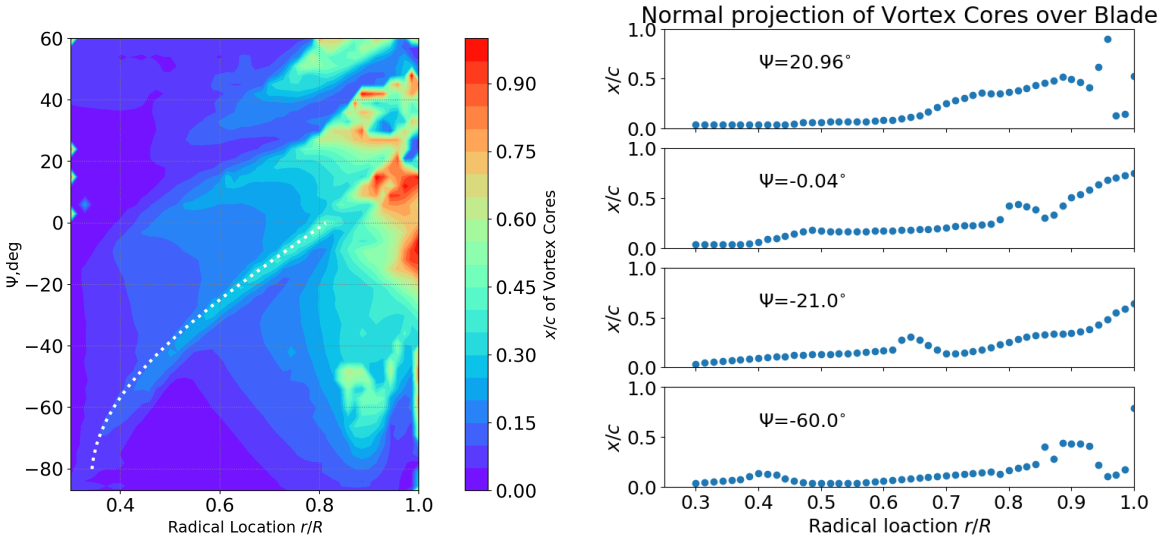

Figure 4.10: **Left**: Location of the vortex cores over the blade in radical region $r/R = 0.3 \sim 1.0$ evolving along azimuth. Dotted line is a curve $r/R = 1/2 \times 0.248\Delta\Psi^2 + 0.16\cos(\Psi)\Delta\Psi + 0.3426$, $\Delta\Psi$ in rad. **Right**: Projection of vortex cores on the blade upper surface at selected azimuths.

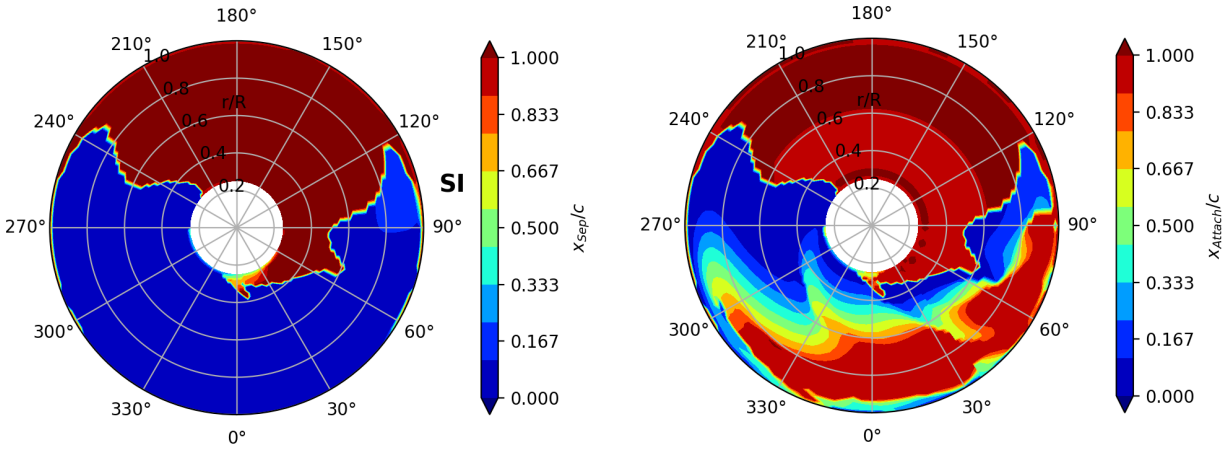

Figure 4.11: Rotor map of chord-wise separation x_{Sep}/c and attachment x_{Attach}/c locations. The direction of the free stream is from $\Psi = 180°$ to $\Psi = 0°$, and the rotating direction is counterclockwise.

4.3 Separation points

BASED on the methods mentioned in section 3.4.1, the classical skin friction criterion is chosen to extract the separation points on the blade at different azimuth angles.

The skin friction lines are plotted in Fig. 4.12 and the extracted separation points and attachment points are plotted in Figure 4.11.

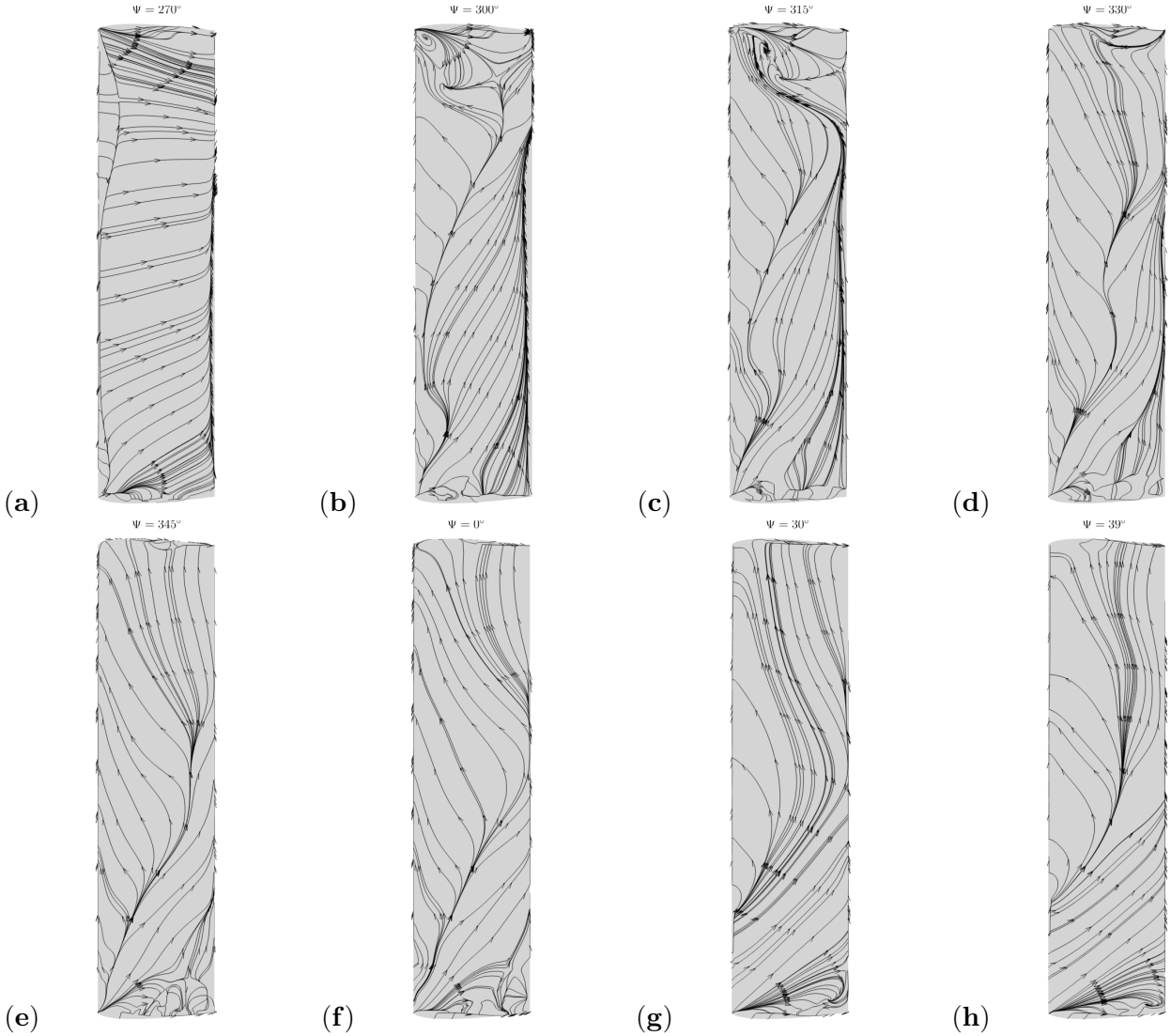

Figure 4.12: Snapshots of the skin friction lines c_f. For each subplot, the blade is placed the same way as in Figure 4.5, with the top side being blade tip and bottom being blade root, the left side being the blade leading edge, and the right side being the trailing edge. Azimuth positions are: Ψ = (**a**) 270° (**b**) 300° (**c**) 315° (**d**) 330° (**e**) 345° (**f**) 0° (**g**) 30° (**h**) 39°.

The leading-edge separation of boundary layer starts outboard and inboard both at $\Psi = 230°$, while, at mid-span $r/R = 0.6$, this starts at $\Psi = 250°$. Together with the attachment points, we see that, between azimuth angle $\Psi = 240°$ and $\Psi = 270°$, the flow re-attaches immediately beyond the separation points, which indicates the existence of attached leading edge vortex. When the blade enters the third quadrant, the attachment

points begin to move downstream, but the starting azimuth is highly dependent on the radial location. For example, at $r/R = 0.89$, the vortex begins to grow leeward very early while, at $r/R = 0.5$, the vortex remains at the leading edge for a long time. Note that the growth of LEV starts at both ends of the blade and propagates toward mid-span.

A helicopter blade may not show the same character, for example simulation by [98], shows a rather inboard to outboard propagation of the growth of LEV, in which 7A rotor has a linear twist -8.3deg/R meaning larger pitch angle inboard. In this case, the pitch angle is the same for different radial stations, and we observed a double directional propagation of the growth of LEV. Costes et al. [135] mentioned that, in the vicinity of wing tip, the flow is attached due to tip vortex induced flow as the wing pitches. And this holds for the azimuth angles before $\Psi = 330°$. As is already shown in Figure 4.6 that there exists a strong correlation of tip vortex strength Γ_x and the leading edge vortex strength Γ_{y-}, and it is indeed this interaction of LEV with tip vortex makes the LEV no longer staying attached at tip. At $\Psi = 90°$, we can see a light-coloured region out board, where the separation occurs between $x/c = 0.121$ and $x/c = 0.223$, far away from the other leading edge separation positions. Figure 4.13 shows the Mach contour, pressure coefficient c_p and skin-friction coefficient in the x-direction c_{fx} at radial location $r/R = 0.898$ at this azimuth angle. On the upper surface of the blade section, c_{fx} drops from positive to negative and crosses 0 at $x/c = 0.12$, where the $-C_p$ shows a sharp decrease. This separation is obviously a product of shock wave. Based on the discussion above, we can categorise the rotor map into four regions, namely fully attached region (F.A.), leading-edge separation region (L.S.), fully separated region (F.S.) and a shock induced separation region (SI). These regions are plotted in Figure 4.14.

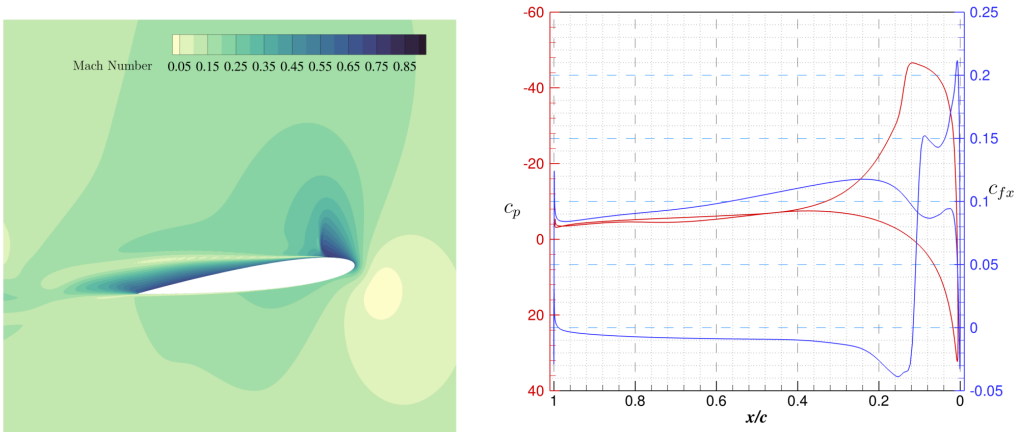

Figure 4.13: Mach contour of the slice $r/R = 0.898$ and the corresponding pressure coefficient c_p, skin-friction in the x-direction c_{fx} on the blade section, azimuth angle $\Psi = 90°$. On the upper surface, c_{fx} drops from positive to negative and crosses 0 at $x/c = 0.12$, where the C_p shows a sharp increase.

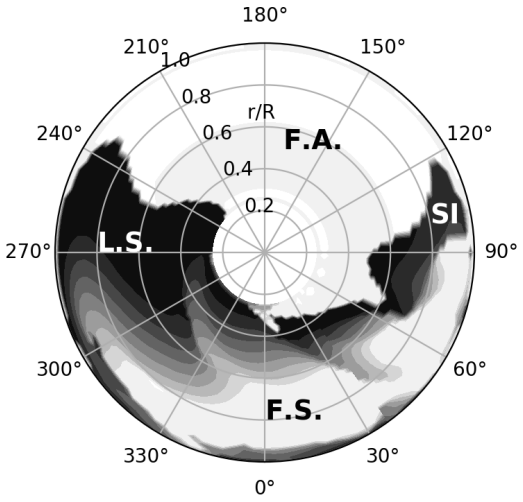

Figure 4.14: Rotor map of separation regions. F.A. is the fully attached region; L.S. is the region where the LEV is attached, and the conical vortex structure on the rotating blade is present; F.S is the fully separated region due to the shedding of DSV; SI is the shock induced separation region.

4.4 Comparison of stall on the rotating blade and non-rotating 2-D pitching airfoil

In order to understand the differences of dynamic stall between a rotating blade section and a pitching airfoil with the same harmonic pitching, the force coefficients and the Q contours of both cases are plotted in Figure 4.15. This span-wise location is exactly the center of the Ω-type dynamic stall vortex. The numerical investigation of a pitching airfoil satisfying equation (1) is explained in detail by [136]. The main differences between the pitching airfoil (2D case) and the section of the three-dimensional rotating blade (3DR case) include: (1) the magnitude of the force coefficients (both C_n and C_m) differ significantly in the pitching-up phase; (2) the onset of the stall of the pitching airfoil is, in terms of the pitch angle, earlier than the blade section.

The maximum normal force coefficient C_n of the airfoil is 1.85 while the value of the blade section is only 1.16. In the process when the leading-edge vortex grows, there is an obvious increase of the slope C_{n_α}, while this is not observed on the blade section. The normal force of the pitching airfoil stalls at 16.67°, and the blade section stalls at 20°. In the post-stall stage, normal force coefficients C_n are relative close to each other. The extreme value of the moment coefficient C_m of the 2D case is -0.425, while the counterpart on the rotating blade is only -0.145. The moment stall of the blade section lags behind that of the pitching airfoil, and is relatively milder.

Four characteristic points on the normal force curve are selected and correlated with the vortex structure in Fig. 4.15, namely (a) early stage when the normal force stall onset occurs on the pitching airfoil, and moment stall onset on the blade, with only leading edge separation, (b) the 1st local maximum C_n in one revolution, (c) the first

local minimum of C_n for both the pitching airfoil and the slice at $r/R = 0.898$ on the blade, and finally (d) the maximum angle of attack. From (a) to (c), the pitching airfoil goes through stall onset, LEV growing to cover the whole upper surface of the airfoil and growing trailing edge vortex(TEV) that comes along with the detachment of the LEV. However, the stall process on the blade doesn't seem to occur until time (c). LEV is not present on the blade at (a), and after the LEV begins to grow, the C_n begins to drop immediately. The LEV occupies less than half of the chord on the blade at time (b) while C_n has reached the local maximum. And even at time (c), the dynamic stall vortex is still concentrated at the leading edge, although it is lifted off from the surface. Indeed the process from (a) to (d) is the process of moment stall, which agrees with the evolution of the vortical structures.

Actually this decrease of C_n is an effect of the arced Ω-shaped vortex structure. Directly under the arced vortex, the normal force coefficient C_n shows the stalled feature. Unlike the 2D case, the vortex is not convected away, rather it still connects with the LEV. Fig. 4.16 shows the local C_n and C_m, which is non-dimensionalised by the local free stream velocity $U_{loc} = \Omega r + \mu\Omega R\sin(\Psi)$. It is shown that only at $r/R = 0.898$ there is a slight decrease in C_n while C_ns at both $r/R = 0.82$ and 0.92 do not stall in the upward pitching phase.

The vorticity ω_y of the counter-clockwise rotating vortex over the upper surface of the airfoil in Figure 4.15 is integrated and plotted in Figure 4.17. This value interprets the total strength of the DSV and TEV for one revolution. The two curves have a similar trend, in the early stage of upward pitching phase, the curves of the circulation are quite flat. Then, after a slight decrease they surge up and in the downward pitching phase, they attenuate in oscillation. There are still three major differences:

(1) The maximum circulation of the DSV in 2D case is larger;

(2) The oscillation of the 2D case in the downward pitching scenario is stronger and the vortex strength of the 2D case is obviously larger;

(3) There is a delay of 8.1° for the 3D rotating blade case when comparing the point when the LEV strength begins to grow.

The first point **may** be explained as the lack of a third dimension for the vortex to grow, resulting in a concentration of vorticity. The second point **may** be explained as the continuing transportation of the vorticity. At the early upward pitching phase ($4° \leq \theta \leq 11°$), the circulation of the 3D slice is clearly smaller which may also be the effect of the continuous transportation of vorticity. The third point can be explained as the combined effect of the induced velocity field V_i in the rotating environment and the outward transportation of vorticity by the radial flow. The induced velocity field means that the effective angle of attack on a rotor blade is different from that on a pitching airfoil: $\alpha_{eff} = \theta(\Psi) - V_i(r,\Psi)/U(r,\Psi)$; Additionally, the outward transportation of vorticity means that, unless an increase of Γ_{net} is present, the circulation over the blade section will not increase. Here,

$$\Delta\Gamma_{net} = \lim_{\Delta\to 0} \frac{(\iint_S v\Delta t\mathrm{d}A)\Gamma_{y,\ r/R\to 0.898-} - (\iint_S v\Delta t\mathrm{d}A)\Gamma_{y,\ /R\to 0.898+}}{\iint_S \Delta y\mathrm{d}A} + \Delta\Gamma_{other} \quad (4.4)$$

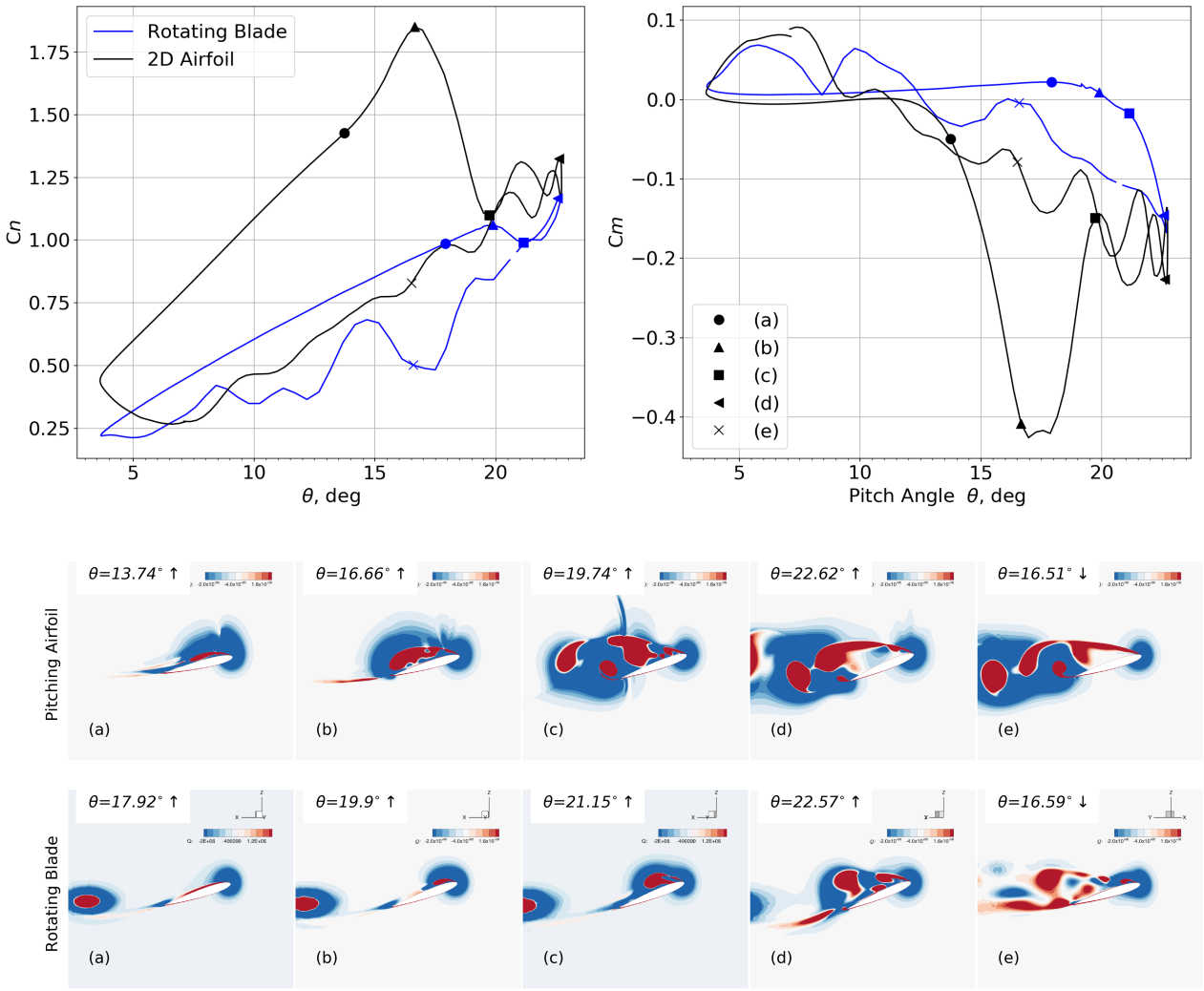

Figure 4.15: Up: Comparison of Sectional force coefficients on blade at $r/R = 0.898$ with the numerical simulation of non-rotating pitching blade and pitching airfoil. Down: vortical structure on pitching airfoil and the slice at radial location $r/R = 0.898$ of the rotating blade, shown as a contour of Q at selected pitch angles shown in the force plot. For rotating blade, these pitch angles correspond to azimuth angle (**a**) $\Psi = 264.0°$, (**b**) $\Psi = 279.0°$, (**c**) $\Psi = 291.0°$, (**d**) $\Psi = 315.0°$, (**e**) $\Psi = 33.0°$. The coordinate in the slice of the rotating blade is inertial.

"0.898−" is the side of the blade section towards root, and "0.898+" is the side of the blade section towards tip. $\iint_S v\Delta t dA$ is the flux caused by the spanwise flow and $\Delta y \iint_S \mathrm{d}A$ is the volume between the two measured surface, hence $\Delta y = v\Delta t$. Assume

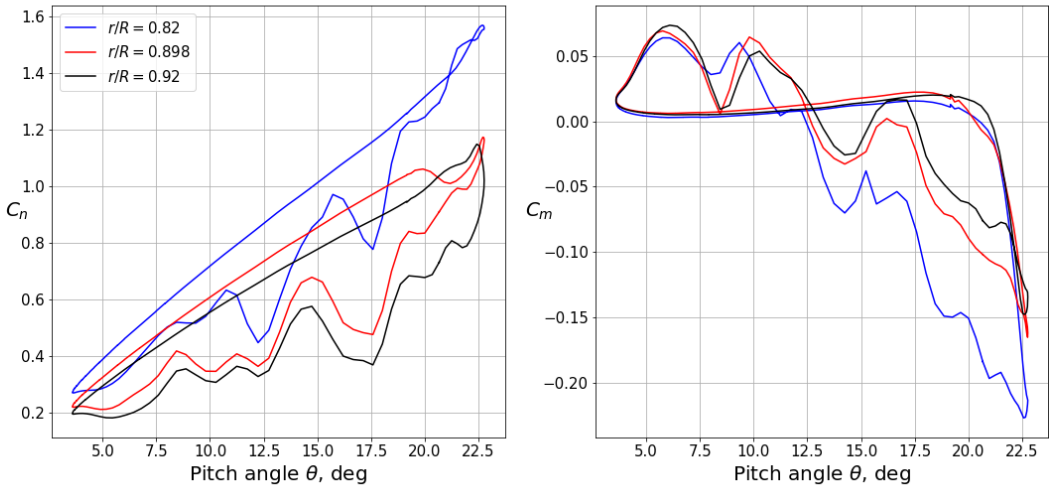

Figure 4.16: Sectional force coefficients C_n and C_m at different radial locations, $r/R = 0.82$, 0.898 and 0.92.

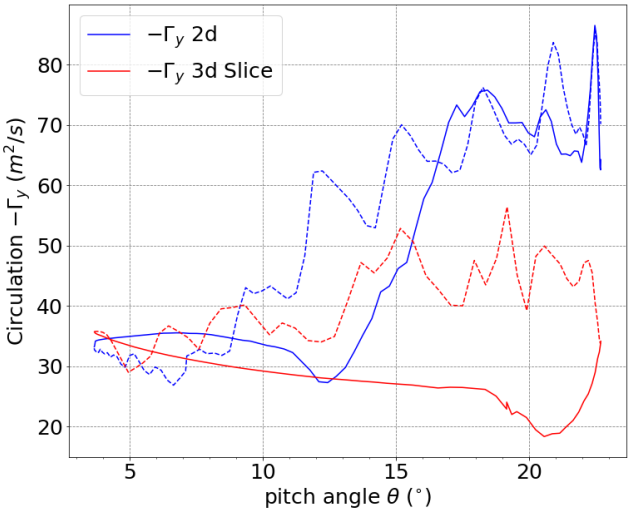

Figure 4.17: Integration of vorticity over the upper surface ($0 \leq x/c \leq 2.25$, $0 < z/c < 2$) of the pitching airfoil and the slice of the rotating blade, with solid lines representing the upward pitching and dashed lines the downward pitching. The circulation $\Gamma_y = \iint_S \omega_y dA$, integrated in region S, $S : Q > 0$.

that v is constant across the integration area, the equation can be rewritten as:

$$\lim_{\Delta t \to 0} \frac{\Delta \Gamma_{net}}{\Delta t} = \lim_{\Delta y \to 0} v \frac{\Gamma_{y,\ r/R \to 0.898-} - \Gamma_{y,\ /R \to 0.898+}}{\Delta y} + \lim_{\Delta t \to 0} \frac{\Delta \Gamma_{other}}{\Delta t} \tag{4.5}$$

This is an approximation of the term $\iint_A(-v\frac{\partial\omega_y}{\partial y})\mathrm{d}A$ in vorticity transport function, Equation 3.16.

Nevertheless, the explanation for the differences between the pitching airfoil and the blade slice is based on Ellington's [69] assumption that the span-wise flow plays a significant role, **which may not be true** as is already shown by previous research that span-wise flow isn't even sufficient to stabilise the LEV on the rotating blade [72]. The other terms of Eq. 3.16 need to be examined to confirm the assumption or provide a more comprehensive explanation.

Blade element momentum theory (BEMT) is the lower order model that is widely used to predict the loads on the rotor disk. The in-flow sub-model is used for determining the effective angle of attack (AoA) for the blade elements. If we take the Drees linear inflow model [45] and implement the momentum analysis on the rotor for our case, we can get the modelled induced AoA as shown in Figure 4.18(a), (b). At the radial location $r = 0.898$, the induced AoA α_i has a maximum value of 2.6°, which is much smaller than 8.1°. Hence, the evaluation of transported circulation is another modelling factor to relate the stall event on the blade section to that on the pitching airfoil.

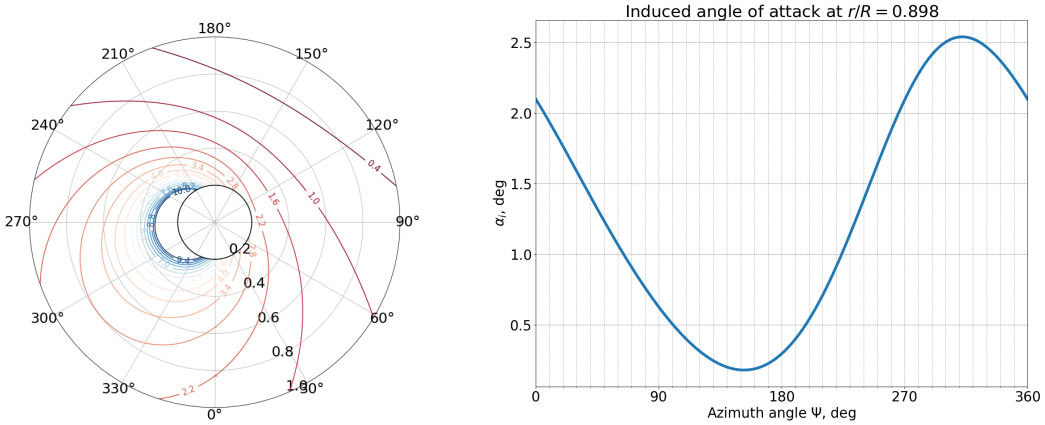

(a) (b)

Figure 4.18: Induced AoA according to BEMT, $\alpha_i = V_i/U(r,\Psi)$; (**a**) rotor map of α_i; (**b**) α_i at $r/R = 0.898$.

4.5 Comparison of the simulation results with different turbulence models

THE analyses are mainly based on the simulation with SA turbulence model. In this section, we are going to compare the SA-model-based simulation result with the k-ω-model-based one. Figure 4.19 shows the net thrust coefficients and y moment coefficients for both turbulence models with standard point-cloud refined wake region and k-ω model with cylindrical refined wake region as described in 3.2.2. We evaluate the sensitivity

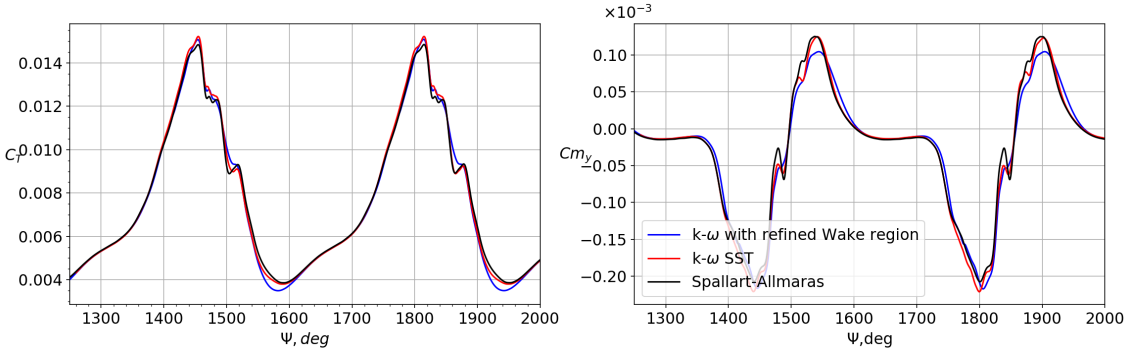

Figure 4.19: Comparison of the net thrust coefficients and y moment coefficients of the rotor.

of the net thrust coefficient C_T and the net moment coefficient C_{my} as:

$$\sigma = \sqrt{\frac{1}{N}\sum_{\Psi i}^{N}\left(C_{T,\ my}^{seq\ compare} - C_{T,\ my}^{std\ seq}\right)}, \tag{4.6}$$

where $^{std\ seq}$ denotes the standard sequence, the time history of C_T or C_{my} of the simulation with standard point-cloud refined wake and k-ω SST turbulence model, and $^{seq\ compare}$ represents the time history of the simulation with either SA model or a cylindrical refined wake region. The result is summarised in Table 4.1. Hence we can draw the following conclusions:

- Both C_T and C_{my} are more sensitive to the wake refinement methods than the turbulence model when the other variable is fixed.
- C_T is less sensitive than C_{my} when either wake refinement method is changed or another turbulence model is implemented.

Table 4.1: Sensitivity of C_T and C_{my} to wake refinement methods and turbulence models.

Sensitivity	to Wake refinement method	Turbulence model	ratio
δ_{C_T}	2.00×10^{-4}	1.88×10^{-4}	1.06
$\delta_{C_{my}}$	5.09×10^{-4}	3.68×10^{-4}	1.38

Table 4.2: Sensitivity of C_n and C_m at $r/R = 0.898$ to wake refinement methods and turbulence models.

Sensitivity to	Wake refinement method	Turbulence model	ratio
δ_{C_n}	7.62×10^{-3}	4.50×10^{-2}	0.17
δ_{C_m}	1.73×10^{-3}	1.33×10^{-2}	0.13

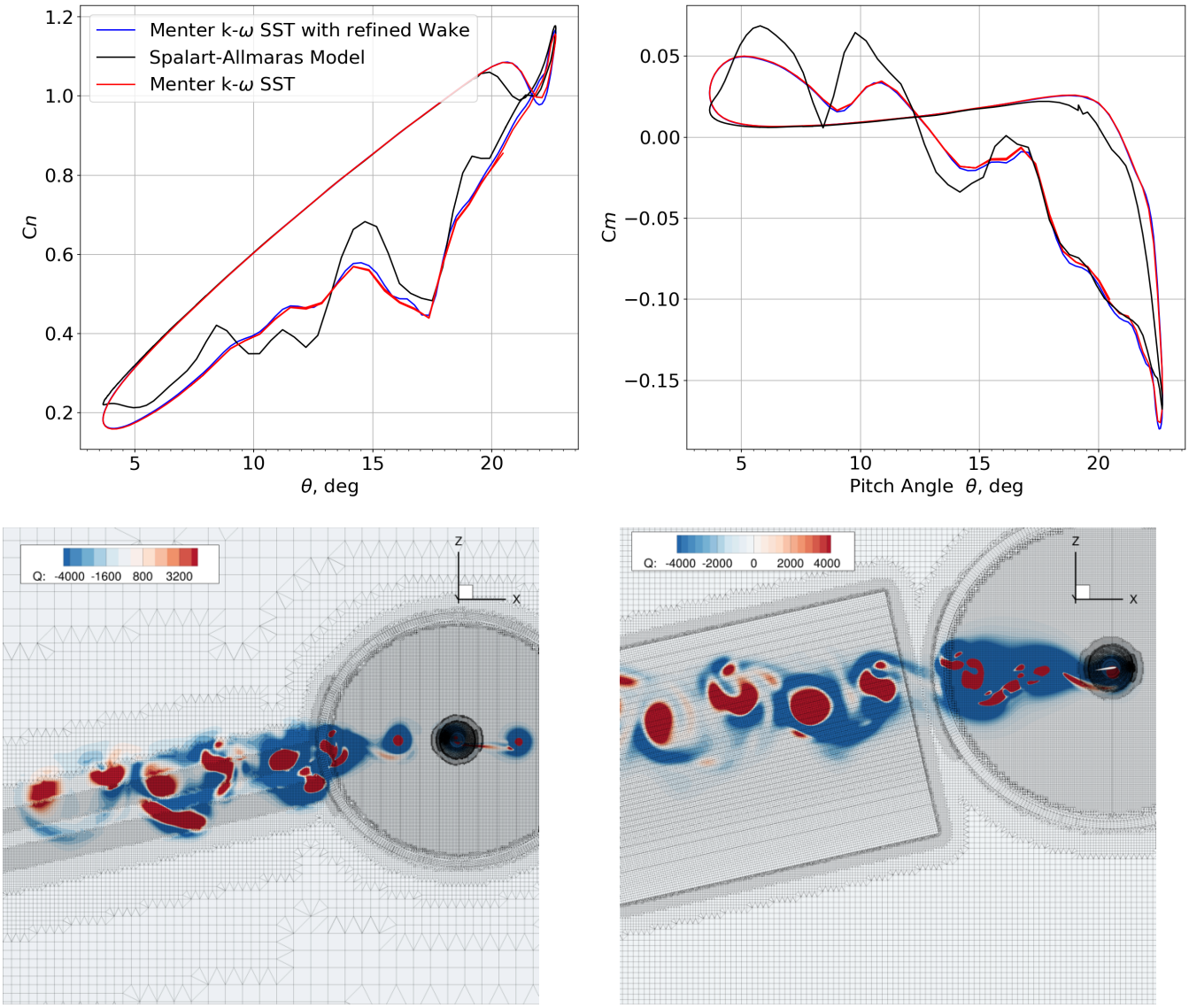

Figure 4.20: **Up**: Comparison of normal force and moment force coefficients of different grid strategies and turbulence models; **Down**: Comparison of the vortex cores in the wake region. **left**: standard point-cloud refined wake region; **right**: cylindrical refined wake region.

Figure 4.20 shows the differences of the normal and moment coefficients at radial $r/R = 0.898$. The red and blue curves are almost identical. It is obvious that both sectional force and moment coefficient C_n and C_m are more sensitive to the turbulence model than to the wake refinement methods. We use the same equation (Eq. 4.6) to evaluate the sensitivity, and the values are summarised in Table 4.2, the values agree

with our intuition. This seems to contradict the conclusions we draw for C_T and C_{my}, but if we examine the magnitude of the sensitivity, the sensitivities of the net force is of the same magnitude, that is, $\sigma_{C_T,\ wake} : \sigma_{C_T,\ turbulence\ model} = 1.063$, while that of the chord-wise force is almost one magnitude smaller, $\sigma_{C_n,\ wake} : \sigma_{C_n,\ turbulence\ model} = 0.17$. Hence we can conclude that:

- Both sectional C_n and C_m are more sensitive to the turbulence model than the wake refinement methods when the other variable is fixed.
- Sectional coefficients are more sensitive to the turbulence model than the net thrust or moment coefficients.
- Since dynamic stall events are highly radial dependent, the selection of turbulence model is hence more important than the refinement of the method.

We shown in Fig. 4.21 the difference between the k-ω turbulence case with cylindrical refinement method and the SA case with point-cloud standard refinement method. It is seen that in the post-stall stage, the discrepancy are more obvious than the un-stalled azimuths. And the discrepancy increases with the radial location r/R. Fig. 4.22 shows the difference of the vortex cores' locations on the blade. At $\Psi = 300°$, the x_c value of the vortex cores at $r/R = 0.9$ predicted by SA model is more aft-ward, which is corresponding to an early drop of C_n and the z_c value at $r/R = 0.9$ by SA is smaller, hence a larger C_n after the lift-off of the Ω-shaped vortex is presented in Fig. 4.20. Moreover, the swell structure seems to move slower if the turbulence model SA is used.

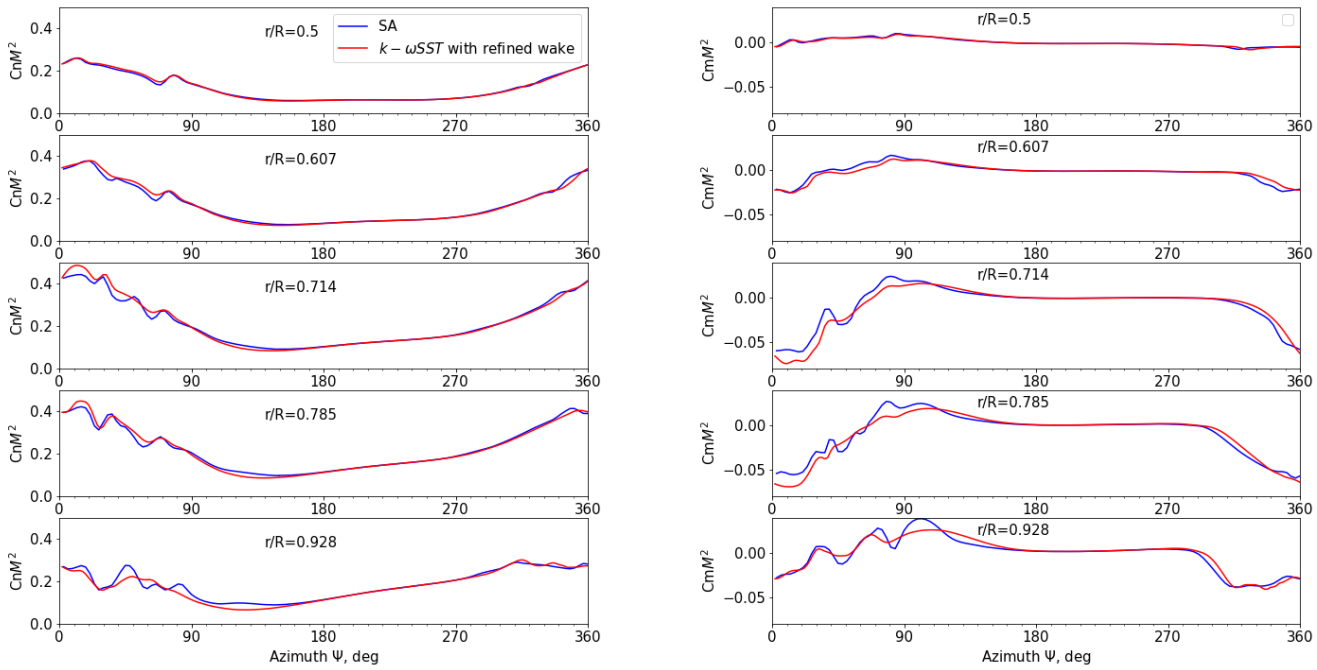

Figure 4.21: Comparison of the sectional force coefficients C_nM^2 and C_mM^2 between two simulations.

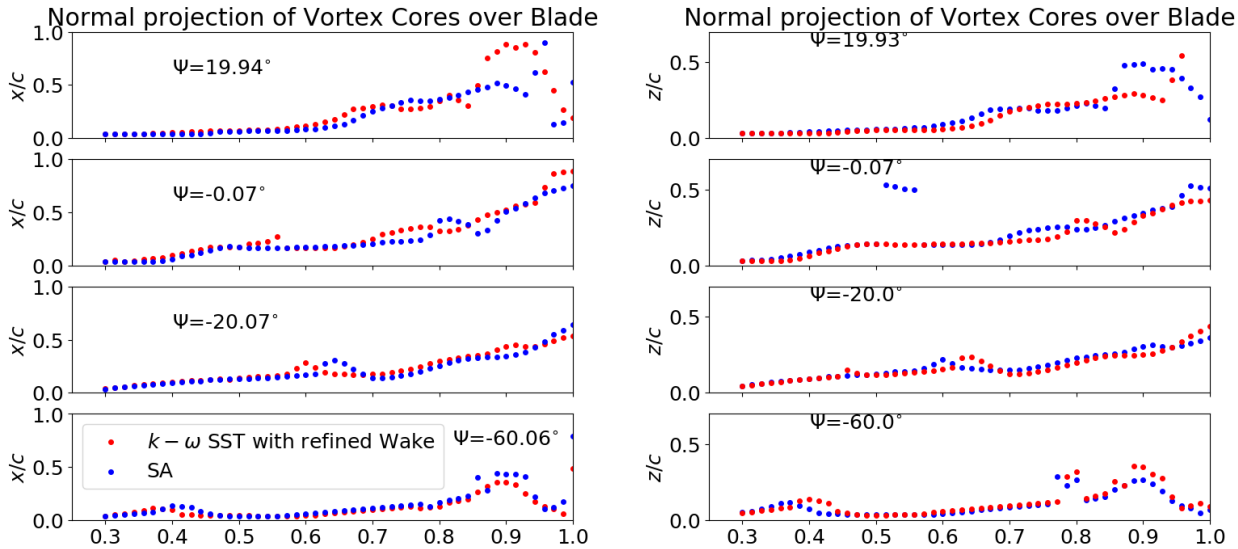

Figure 4.22: Comparison of the vortex core locations on the blade between two simulations.

5 Understanding dynamic stall on the rotating blade: Vorticity transport analysis

5.1 Vorticity transport analysis on the rotating blade

BASED on the vorticity transport analysis method described in Section 3.4.3 in Chapter 3 , the terms in Eq. 3.34 are evaluated for each azimuth angle, and the result is plotted in Fig. 5.1. The planer variation $\oint_{\partial A}(\mathbf{u}\cdot\mathbf{n})\omega_y \mathrm{d}s$ is broken into 5 components, namely the five boundaries as described in Fig. 3.15. The line integration of pressure gradient is split into the part in the fluid and the part on the wall, with the latter representing the contribution of wall vorticity flux. The acceleration term in the fluid part $\int_f \mathbf{a}\cdot\mathrm{d}\mathbf{s}$ is plot as a whole, and the contributions of centrifugal effect, Coriolis effect is discussed later. The span-wise convection part and the vorticity tilting terms are also plotted in lighter colours.

It is obvious that the planer variation and the pressure gradient are the most dominant terms throughout the whole revolution. The red curve represents the large scale of vortex going through bound 2, and positive value means the leading edge vortex (the Γ of which has a negative sign) are convecting through this boundary line, the scale of the vortex reaches $0.33c$. The vorticity convection and tilting are only obvious after $\Psi = 260°$, when the leading edge vortex begins shedding. They enters great oscillation in the post-stall phase, and seems to always have negative signs. Or in other words, the vorticity tilting and the span-wise convection of the vorticity are highly correlated. We can then expand the modelling of the circulation in the third dimension from Eq.2.9 with blade elements' circulations:

$$\frac{\partial\Gamma}{\partial t} - v\frac{\partial\Gamma}{\partial y} + \dot{\Gamma}_{tilting} = \dot{\Gamma} \tag{5.1}$$

if this correlation exists, $\dot{\Gamma}_{tilting} = g(-v\frac{\partial\Gamma}{\partial y})$, we can then improve the lower order model in the third dimension.

Fig.5.1(b) shows the difference between the summation of split terms and the direct evaluation of $\partial\Gamma/\partial t$, the error comes from the large values of the vorticity field and the numerical integration of these values, as well as the difference method used to evaluate the circulation's change rate due to inadequate number of snapshots of flow fields in one revolution. We are going back to discuss it later.

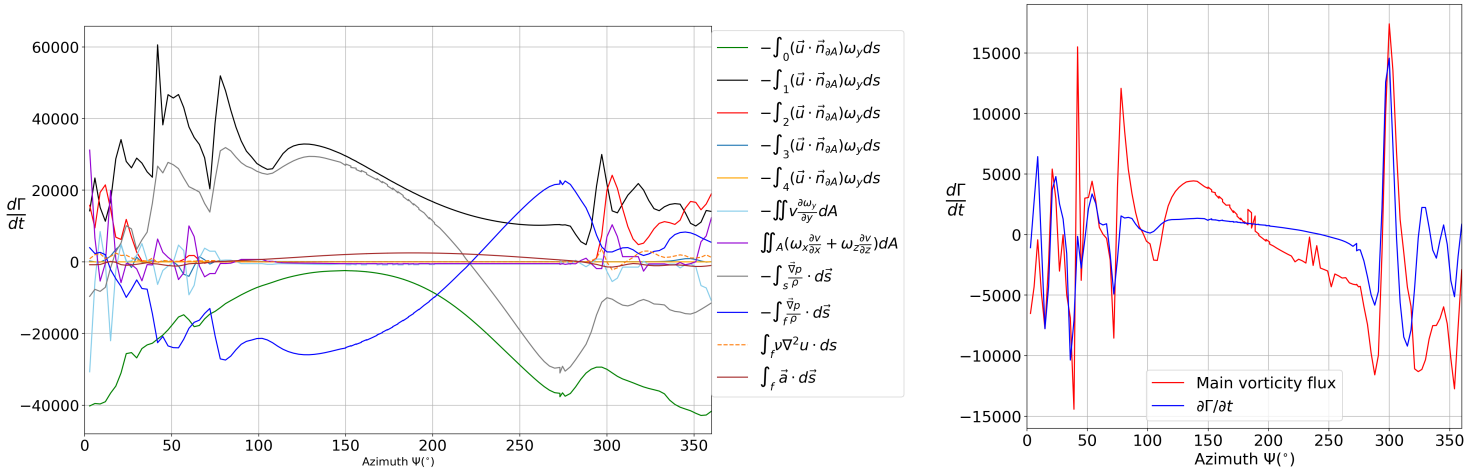

(a) (b)

Figure 5.1: (a) Contribution of different terms to the circulation change in the control volume. (b) Comparison of the summation of the terms and $\mathrm{d}\Gamma/\mathrm{d}t$

The Contribution of pressure gradient and the effect of Compressibility

The pressure gradient has two distinct phases: in the azimuth range $\Psi \in [15°,\ 222°]$, the pressure gradient act as a "source", which contributes to the accumulation of the negative ω_y; while in the range $\Psi \in [222°, 15°]$, the pressure gradient acts as a "sink", hindering the strength of leading edge vortex. This might from intuition contradict the surface vorticity flux theory, which states that **a negative value of the pressure gradient serves as the source for the leading edge vortex**, since the LEV is growing in the phase period $\Psi \in [230°, 270°]$. However, when the LEV is lifted off from the blade surface, vorticity with positive sign is generated underneath it. And our integration of the pressure gradient along the surface is thus a representation of the net contribution of both the "source" and the "sink" of the LEV. On the other hand, the stronger the LEV, the stronger the induced vortex comes along with it. And here, this term represents the strength of the induced vorticity by the LEV, **indirectly showing the strength of the LEV**.

One has to be very careful treating the term $\oint \frac{\nabla p}{\rho}\cdot\mathrm{d}\mathbf{s}$, which equals 0 for incompressible flow. By comparing this term with 0 doesn't imply the compressibility effect, since the compressibility effect also influences the viscous term, $\nu\nabla^2 u$, in which there is the term $\frac{\nabla p}{\rho}$. As is derived in Section 3.4.3, the net contribution of the pressure gradient term is only the integration of pressure gradient in the flow field, namely $-\int_f \frac{\nabla p}{\rho}\mathrm{d}\mathbf{s}$. Fig. 5.1 shows this term at different radial locations, and since the free-stream Mach number M_∞ varies along the radial direction, the compressibility effect can be seen from the peak value of $-\int_f \frac{\nabla p}{\rho}\mathrm{d}\mathbf{s}$. As the radial location moves outwards, M_∞ increases, and the peak of this term decreases. Or in other words, the increasing compressibility results in a decreasing strength of the leading edge vortex. This agrees with what Patrick [39] reports

on the compressibility effect. Notice that in the advancing phase, the compressibility effect strongly augments the LEV, which results in shock-induced separation as discussed in Chapter 4.

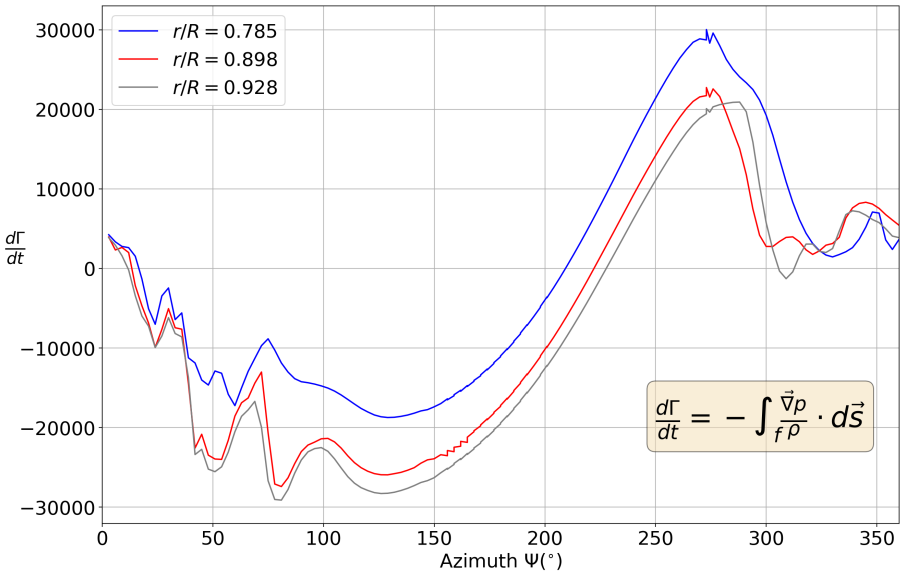

Figure 5.2: Pressure gradient contribution to vorticity change at different radial locations: Compressibility effect with respect to the vorticity transport analysis

Vorticity tilting and span-wise convection

We have plotted the integral of vorticity tilting vs. the integral of span-wise convection in Fig. 5.1. The linear regression model gives a standard deviation of 0.0262, and the determination coefficient $r^2 = 0.9123$.

This also means, the summation of these 2 terms yields a very small value, comparing to the planar variation. Hence the assumption in the previous chapter that the large oscillation of force coefficients is a pure result of the span-wise convection of the y vorticity should be extended by adding the contribution of the tilting term.

Rotational acceleration effect

The acceleration terms has a positive contribution to $\partial\Gamma/\partial t$ in the azimuth angles $\Psi \in [75°, 285°]$, although it is very small comparing with other terms, but is significantly larger than the viscous term in the flow field, and comparing to a 2D case, this term increases significantly in the 3D rotating case. A positive contribution acts as a "sink" for the leading edge vortex, and this "sink", larger than the span-wise convection term in azimuth angles $\Psi \in [100°,\ 250°]$, is responsible for the stability of the conical shaped leading edge vortex on the rotating blade. This term changes its sign when the dynamic stall begins, which serves as a"source" for the leading edge vortex.

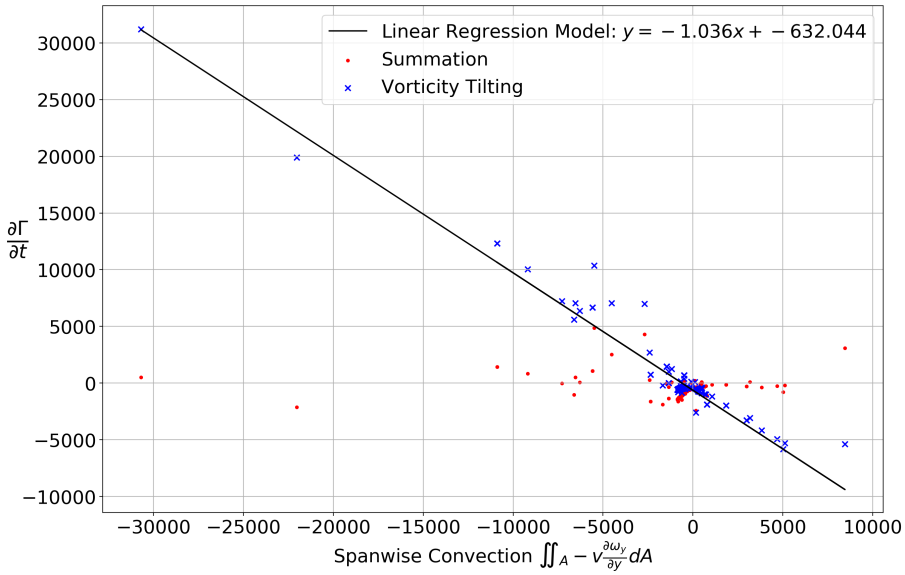

Figure 5.3: Correlation between the span-wise convection term and the tilting term.

The three components of the acceleration terms at radial location $r/R = 0.898$ are plotted separately in Fig. 5.4. The contribution of the Coriolis force is far more larger than the other 2 terms, which agrees with what is concluded by Jardin et. al. [79,80], that Coriolis effect plays a key role in lift generating on a rotating wing, while the centrifugal force has a marginal effect. And our current case shows that under the condition of compressibility, such conclusion holds for the azimuth angle in phase $\Psi \in [70°, 283.5°]$.

The sign of the Coriolis-effect-contributed circulation change rate ($\frac{\partial \Gamma}{\partial t}\big|_{\mathbf{a}_{Cor}}$) alters at $\Psi = 283.5°$ during the stall gestation period, after the stall occurs. The separation type discussed in Section 4.3 shows that for $r/R = 0.898$, the L.E. separation begins at as early as $\Psi = 240°$, and F.S. begins at as late as $\Psi = 300°$: they are not linked to the azimuth angle when $\frac{\partial \Gamma}{\partial t}\big|_{\mathbf{a}_{Cor}}$ changes its sign. Moreover, the rotor map shown in Fig. 4.11 indicates that when azimuth angle $\Psi = 283.5°$, the re-attachment point moves to $x/c = 0.4$ at $r/R = 0.898$. It is likely that this "re-attachment point" is a key factor that influences the sign of $\frac{\partial \Gamma}{\partial t}\big|_{\mathbf{a}_{Cor}}$. Moreover, the yaw effect aroused span-wise flow may also have an important effect on the aforementioned sign-change. For phase angle $90° < \Psi < 270°$, the span-wise component of the yaw flow is negative, or towards blade tip. The Coriolis term reaches its maximum value at $\Psi = 180°$, this is also the azimuth when the yaw-effect-resulted span-wise flow reaches its maximum value.

In deed, this sign change is governed by Eq. 3.28, as shown in Fig. 5.4, the first term of the Coriolis effect plays a small role. Since $|\Omega_x| \ll |\Omega_z|$, and $|\partial v/\partial z| > |\partial v/\partial x|$, it is then obvious that the term $\Omega_z(\partial v/\partial z)$ plays a crucial role for the Coriolis effect. When $-\Omega_z(\partial v/\partial z) > 0$, the Coriolis force acts as a "sink" that stabilises the LE vortex, vice versa. In our case, $\Omega_z < 0$, $\partial v/\partial z > 0$ is the prerequisite for a "sink". As shown in Fig. 5.5, at $\Psi = 180°$, the relative spanwise velocity v increases to a positive extreme and

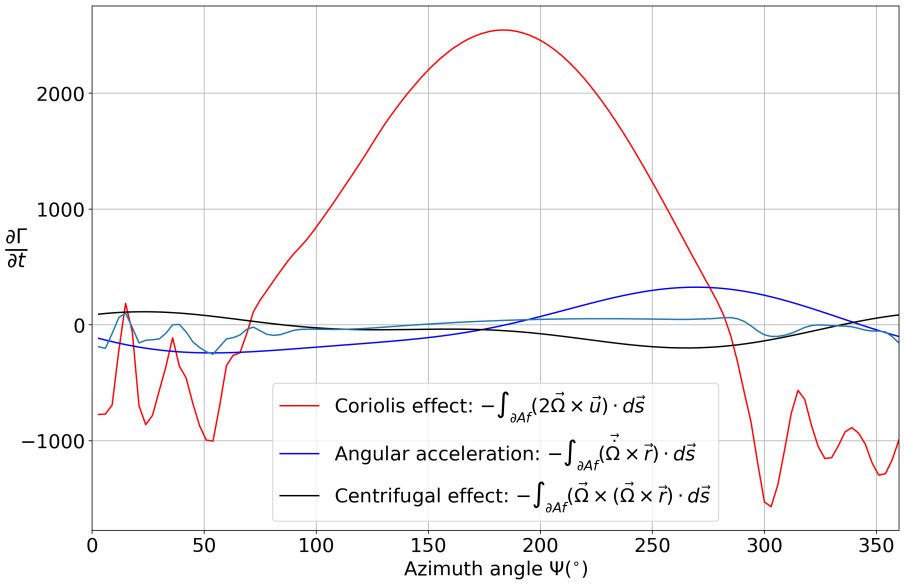

Figure 5.4: Contribution of acceleration terms to the rate change of circulation $\frac{\partial\Gamma}{\partial t}$ at radial location $r/R = 0.898$. With the light blue curve representing the first term of the Coriolis acceleration: $2\Omega_y \oint_{\partial A} \mathbf{u}\cdot\mathbf{n}_{\partial A}\mathrm{d}s$.

then decreases linearly, which is due to the fact that the velocity of the rotational frame increases linearly with $|z|$. This led to the large portion of the control volume showing the characteristic $\partial v/\partial z > 0$. At azimuth angle $\Psi = 270°$, we see that at leading edge, the relative span-wise flow shows a negative $\partial v/\partial z$ in enlarged regions in the control volume, while at azimuth angle $\Psi = 360°$, at leading edge, the velocity profile shows $\partial v/\partial z < 0$ for the majority upper part.

Note that the velocity profile in Fig. 5.5 is the relative velocity in y direction, hence the profile shape does not indicate the separation or re-attachment points on the cross-section. However, within the LEV, the vorticity tilting entangles the in-plane and the span-wise velocity. A sound conclusion can be drawn as: the coupling of the yaw-effect-resulted span-wise flow and the growing up of the LEV results in the sign-change of the term $\frac{\partial\Gamma}{\partial t}\big|_{\mathbf{a}_{Cor}}$.

Stabilisation or de-stabilisation?

The stability of the vortex system on the airfoil going through dynamic stall lacks a strict definition. A vague definition of the stability of the conical vortex system on a rotating wing can be found on previous research like Jardin et al. [79] , Wolfinger et al. [137] to be associated with the attachment of the leading edge vortex. However, when the topic is extended to dynamic stall, the vague definition is no longer sufficient. Since for a complete period of a deep dynamic stall process, the LEV will shed. On the other hand, the control of dynamic stall with momentum flows by Starikovskiy et al. [138] or plasma actuator by Singhal et al. [139] aim at a smaller hysteresis of both C_n and

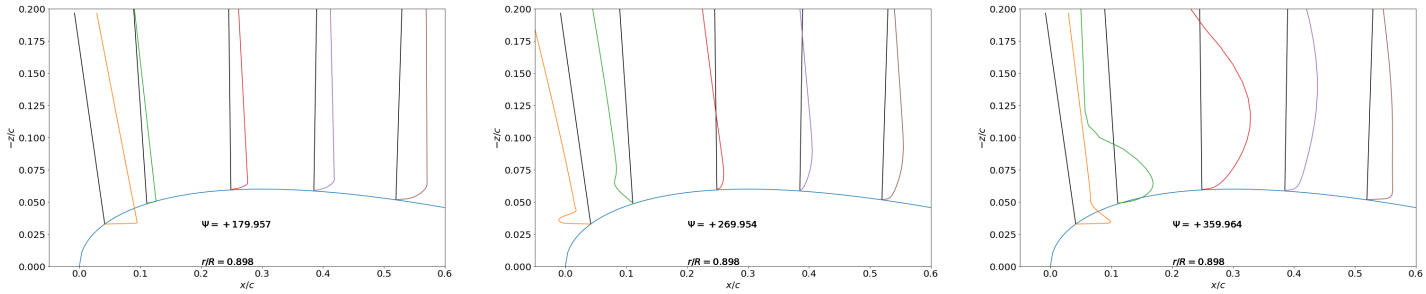

(a) (b) (c)

Figure 5.5: Relative velocity profile in y direction at $r/R = 0.898$ at different azimuth angles: (a)$\Psi = 180°$; (b)$\Psi = 270°$ and (c)$\Psi = 0(360)°$. Due to the inverse of z axis, the coloured lines (v profile) that lean towards (at right side) or extend away (at left side) from the black solid line have the characteristic $\partial v/\partial z > 0$.

C_m. This smaller hysteresis can mean a more 'stable' vortex system over the pitching airfoil. Therefore, in this sense, the definition of the vortex system's stability should be associate with both C_n and C_m. After the detachment of the LEV, the stability denotes a less oscillation of both C_n and C_m curves in the post-stall stage. A stability effect factor η_γ can be defined to present the relative sign and the relative magnitude of the term in vorticity transport analysis:

$$\eta_\gamma = \frac{(\partial\Gamma/\partial t)_i \cdot \Gamma}{\left|\partial(\Gamma/\partial t)_i \cdot \Gamma\right|} \cdot \frac{|(\partial\Gamma/\partial t)_i|}{\sum_i \left|(\partial\Gamma/\partial t)_i\right|} \tag{5.2}$$

in which, the first term represents if the ith term of the vorticity transport function augments or damps the circulation Γ in the planar region, and the second term implies the proportion of the ith term's absolute value among the summation. Note that the absolute values are used for summation, the summation doesn't equal to the total rate change of circulation. By using the absolute value, the relative magnitude can be compared. On the other hand, the vortex resultant force $C_{n,v}$ may be denoted by the difference of the linear approximation of the blade cross-section $C_{n,\,linear} = C_{n_\alpha}(\theta(\Psi) - \alpha_i(\Psi))$ and the total normal force coefficient integrated by the pressure force, with θ representing the pitch angle, and α_i denoting the rotor induced angle of attack approximated by linear inflow model described in Section 4.4. The comparison of the vortex generated force coefficient and the stabilisation parameter for Coriolis term, centrifugal term and the net convection and tilting term are analysed and plotted in Fig. 5.6 .

The comparison of $C_{n,v}$ and η_γ at $r/R = 0.898$ shows that in the range $\Psi \in [70°, 283.5°]$, the Coriolis term has an opposite sign to the net circulation, and in the meantime the vortex resultant force is larger than 0. It means during this period, the Coriolis term has the effect to decrease the vortex resultant force over the airfoil, a stabilisation effect. After the LEV detaches from the leading edge, the vortex resultant force $C_{n,v} < 0$, while the Coriolis term increases the magnitude of the circulation over the airfoil upper

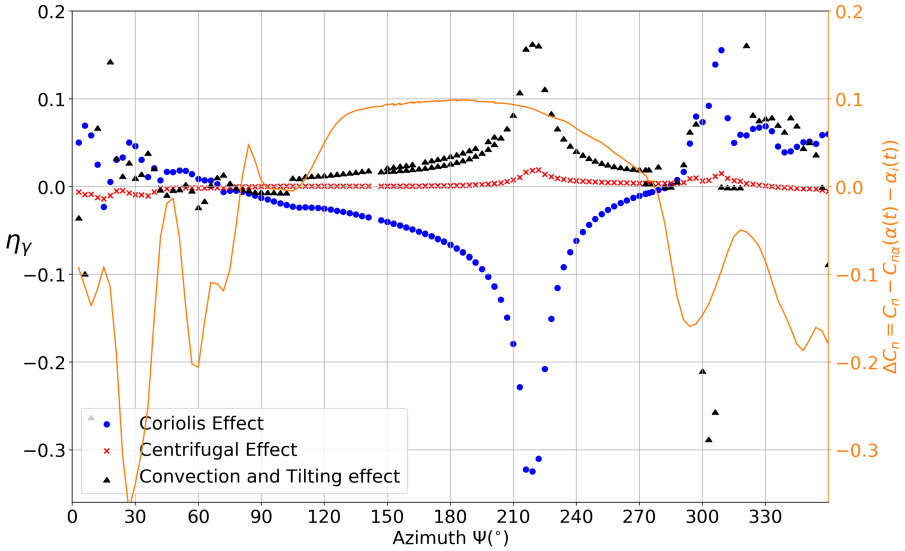

Figure 5.6: Comparison of ΔC_n in orange and stabilisation parameter η_γ for Coriolis term, centrifugal term and the net of span-wise convection and vorticity tilting terms, where ΔC_n is the difference between the cross-sectional normal force coefficient and the linear approximation of the normal force. The definition of the individual terms can be found in Eq. 3.34.

surface, which is a compensation for the loss of the normal force. Hence in this phase, the Coriolis force also has a stabilisation effect in terms of the normal force coefficient.

This conclusion cannot be easily extended to the moment coefficient. Since the movement of the vortex on the upper surface of the blade can result in a shift of the pressure centre. There are, however, no direct equations that state the individual contribution of the terms to the total pressure centre. Nevertheless, the vorticity change rate field can have a weighted-average position x_ξ:

$$x_\xi = \frac{\iint x\dot{\omega}\mathrm{d}S}{\iint \dot{\omega}\mathrm{d}S} \tag{5.3}$$

this weighted average position x_ξ represents the "centre" of the vorticity field. If $x_\xi < 0$, the majority of the vorticity concentrate within the first quarter chord region. Together with η_γ, the effect of individual terms to the moment coefficient term can be comprehended. The effect of vorticity change rate due to the Coriolis acceleration is plotted in Fig. 5.7. The magnitude is very small and oscillating near 0. As a result, it has a neutral influence on the moment coefficient.

Based on the discussion above, we have a clearer idea about how the circulation in the control region is affected by the different terms. To conclude:

- The rotating system has a generic effect to create a span-wise flow that has a potential stabilising effect on leading edge vortex.

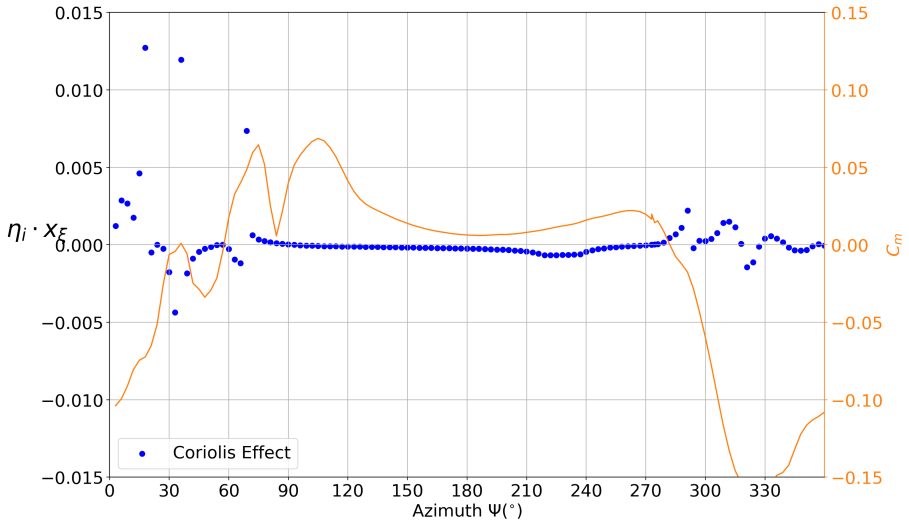

Figure 5.7: Comparison of C_m in orange and combined stabilisation parameter $x_\xi \cdot \eta_\gamma$ for Coriolis term.

- The mechanism of the stabilisation effect lies **NOT ONLY** in the convection of vorticity, **but ALSO in the creation of a "sink" by the normal gradient of span-wise flow.**
- This mechanism is a direct result of **Coriolis term**.
- Coriolis term can also lead to a "source" for the leading edge vortex when **the yaw angle aroused span-wise flow is towards blade tip or the separation region enlarges. This happens during the dynamic stall process, after the shedding of the first dynamic stall vortex.**
- After the shedding of the DSV, the Coriolis acceleration provides a "source" for the LEV, which **stabilises the vortex system** on the rotating blade **by compensating the separation/vortex-resulted C_n coefficient**. And hence for the whole revolution, **Coriolis effect has a stabilisation effect for the vortex system.**

5.2 Comparing with 2D case: Vorticity transport analysis on a pitching airfoil

THE vorticity transport analysis is also carried out for the 2D pitching case, and the terms in Eq. 3.34 are plotted in Fig. 5.8.

For the 2D case, the terms in the 3rd dimension vanish. In Eq. 3.18, the Vorticity tilting and convection vanish, simply due to $v = 0$. And for the acceleration term, due

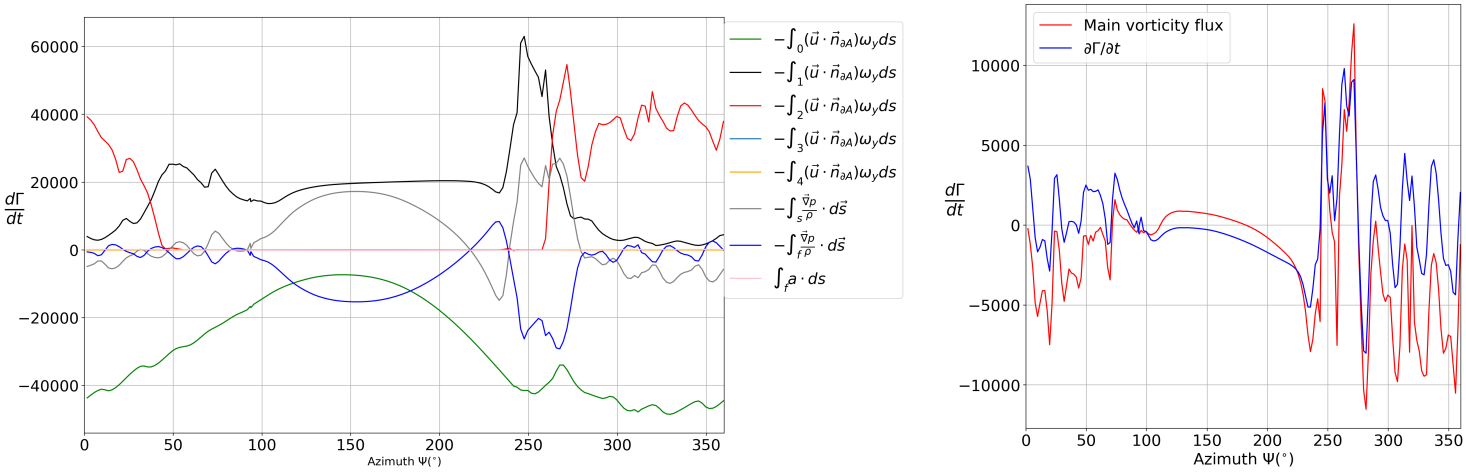

(a) (b)

Figure 5.8: (a) Contribution of different terms to the circulation change in the control volume. (b) Comparison of the summation of the terms and $\mathrm{d}\Gamma/\mathrm{d}t$

to the same reason $v = 0$, the Coriolis effect only reduced to:

$$\oint_{\partial A} \mathbf{a}_{Cor} \cdot \mathrm{d}\mathbf{s} = 2\Omega_y \oint_{\partial A} \mathbf{u} \cdot \mathbf{n}_{\partial A} \mathrm{d}s$$

and because $\Omega_x = 0$ and $\Omega_z = 0$, the centripetal effect on the surface reduces to:

$$\frac{1}{c^2} \int_{\partial A_{bound}} \mathbf{a}_{\mathbf{s,cen}} \mathrm{d}\mathbf{s} = -\Omega_y^2 (\frac{c_1^2}{2} - \frac{c_1}{4} + \frac{1}{2} g^2(c_1)) + c_1 g(c_1).$$

finally the angular accelerating term can be written as:

$$\frac{1}{c^2} \int_{\partial A_{bound}} \mathbf{a}_{\mathbf{s,ang}} \mathrm{d}\mathbf{s} = -\dot{\Omega}_y (\int_0^{c_1} g(t)\mathrm{d}t - (c_1 - \frac{c}{4}) g(c_1)) - \frac{1}{c^2} \iint_A (2\dot{\Omega}_y) \mathrm{d}A$$

These terms contribute only a small value in the net change rate of the circulation in the control volume, as is shown in Fig. 5.8.

The planar variation of the circulation is similar to the rotating blade, with negative vorticity input at boundary 0 and outward-convection at boundary 1. When dynamic stall begins and the separation region extends to a larger scale, the negative vorticity leaves the control region from boundary 2. The pressure gradient is similar in the upward pitching phase before the stall occurs, but fundamentally different when the separation occurs. After reaching the maximum value, which is related to the strongest LEV induced vortex or the start of dynamic stall, this pressure gradient term drops drastically into negative value, which is related to the sudden recovery of the moment coefficient and the complete off-board DSV. While on the rotating blade, this term gradually grows to its maximum value (the maximum LEV induced vorticity on the surface) and drops

gently. This is also associated with the vortex structure discussed earlier: the LEV is not detached completely on the rotating blade, rather it is still connected to the LE via two "legs". This structure prevents the drastic oscillation and allows the continuous growth of LEV induced vorticity.

The difference of the planar variation on bound 1 between the two cases are also a result of the varying inflow velocity. With decreasing velocity from $\Psi = 90°$ to $\Psi = 270°$, this term $\int_1(\mathbf{u} \cdot \mathbf{n}_{\partial A})\omega_y \mathrm{d}s$ also decreases.

5.3 Effect of the radial locations

5.3.1 Contribution of different terms at different radial locations

THE vorticity transport analysis is carried out at different radial locations and the difference of the contribution of different terms are plotted in Fig. 5.3.1. The maximum absolute value of the planar variation at boundary 1 is larger at outboard, while at boundary 0 it is slightly larger at inboard. The vorticity flux through boundary 2 almost vanishes $r/R = 0.785$, which complies with the fact that the LEV never grows into such a big scale as is for $r/R = 0.898$ and $r/R = 0.928$. And indeed, this value $\int_2(\mathbf{u}\cdot\mathbf{n}_{\partial A})\omega_y \mathrm{d}s$ is mostly obvious at $r/R = 0.898$, since this is the location of the symmetric axis of the Ω-shaped vortex.

The pressure gradient effect is already discussed in previous section, with decreasing maximum value and postponed azimuth angle for a sign change as radii r/R increases. The vorticity tilting and span-wise convection of the vorticity is small until $\Psi = 275°$ at $r/R = 0.785$, while these terms show up before $\Psi = 250°$ at $r/R = 0.928$, which indicates a higher 3D effect outboard. Most interestingly, after the dynamic stall occurs, the span-wise convection is negative at $r/R = 0.785$, while stays positive for quite a wide range of phase angles at $r/R = 0.928$, and it starts from negative, oscillating strongly at $r/R = 0.898$.

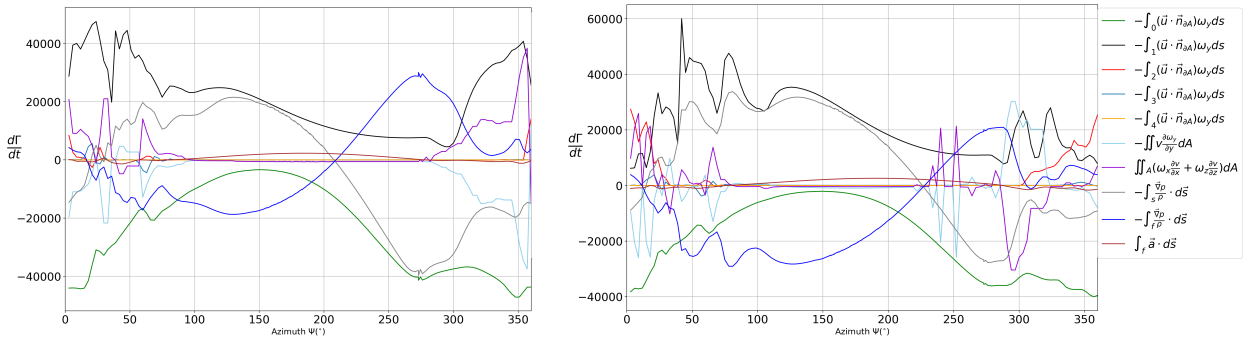

(a) (b)

Figure 5.9: (a) Contribution of different terms to the circulation change in the control volume at $r = 0.785$. (b) Contribution of different terms to the circulation change in the control volume at $r = 0.928$

5.3.2 Vorticity tilting and vorticity convection terms at different radial locations

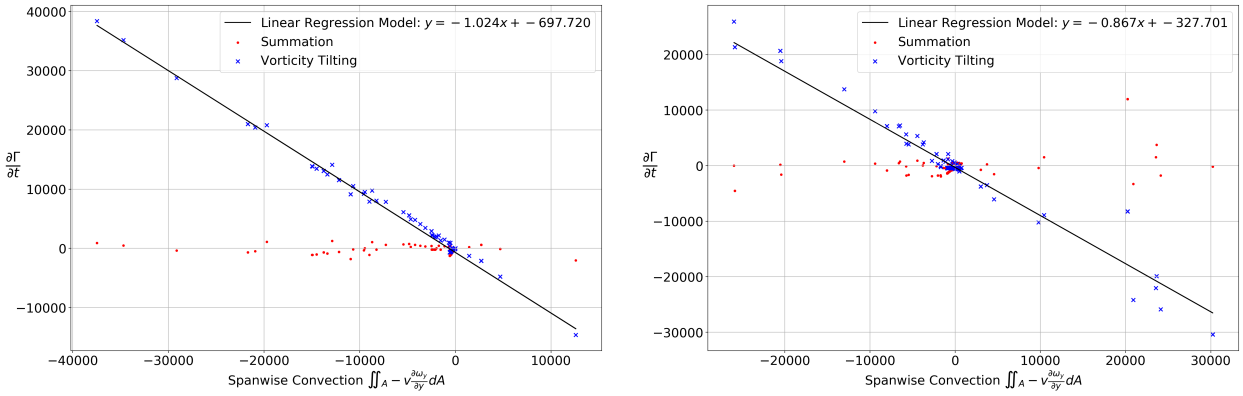

(a) (b)

Figure 5.10: (a) Correlation of vorticity tilting and span-wise convection at radii $r = 0.785$. (b) Correlation of vorticity tilting and span-wise convection at $r = 0.928$

We now examine the effect of the radial location on the linear slope. This k value decreases ($k < 0$) first as r increases from $r/R = 0.785$ to $r/R = 0.898$ and then k increases. Recall the difference behaviour of the span-wise convection term between the region $r/R \in [0.785,\ 0.898]$ and $r/R \in [0.898,\ 0.928]$ as discussed in previous section, the summation of these two terms hence have the same effect for the circulation change rate at the early stage of the dynamic stall: at $r = 0.785$ $\Sigma = -0.036\Gamma_{convection} > 0$, and at $r = 0.898$, $\Sigma = -0.024\Gamma_{convection} > 0$, while at $r = 0.928$, this value $\Sigma = 0.133\Gamma_{convection} > 0$. As a result, we have the conclusion: immediately after the shedding of the DSV, the span-wise convection together with the vorticity tilting act as a "sink" for the negative circulation in the control volume. The net effect of these two terms are plotted in Fig. 5.3.2. Interestingly, the net effect of the span-wise terms plays a role of "source" before the shedding of the DSV, while sometimes acting as a "sink" during the post-stall phase. This is actually contrary to what Ellington [69] has proposed, on the rotating system, **the net effect of the span-wise terms**, including the convection of span-wise vorticity and the tilting of the vorticity from other dimensions, **augments the leading-edge vortex**, which is actually **an unstable** factor for the maintenance of the LEV on the blade. However, these terms seem to hinder the drastic oscillation (a strong secondary vortex) on the rotating system.

5.3.3 Rotational acceleration at different radial locations

The rotational acceleration effect on the change rate of the circulation in the control volume at different radial locations are plotted in Fig. 5.12. It is obvious that there are only marginal difference for the angular acceleration term and the centrifugal term at different radial locations. And the Coriolis term show similar behaviours at different

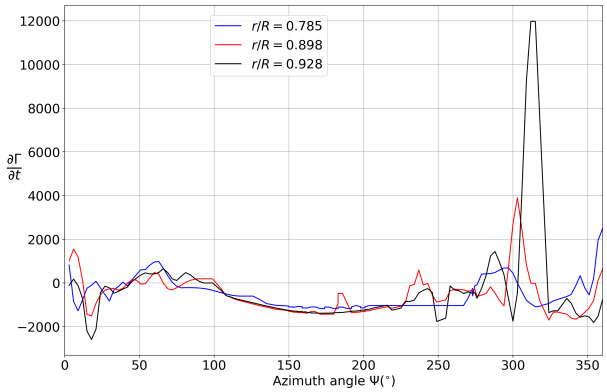

Figure 5.11: Net contribution of the span-wise terms, namely $v\partial\omega_y/\partial y$ and $\omega_x\partial v/\partial x+\omega_z\partial v/\partial z$ to the change rate of circulation in the control volume.

radial locations in the unstalled regime, roughly $\Psi \in [73.5°, 274.5°]$ (the stall on-set depends on the radial location). In the post-stall phase, there is only a phase delay between $r/R = 0.898$ and $r/R = 0.928$, while the value at $r/R = 0.628$ shows different trend in phase angles $\Psi \in [0,\ 73.5°]$.

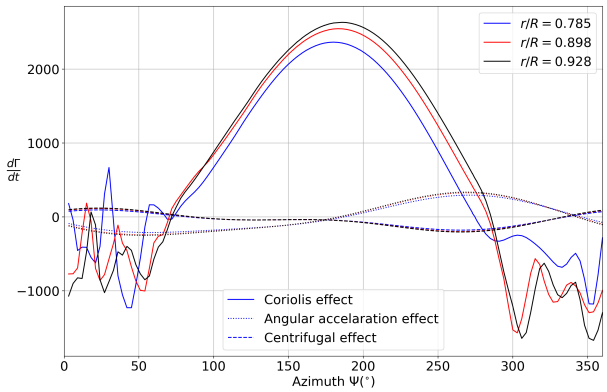

Figure 5.12: Rotational acceleration effect on the change rate of the circulation in the control volume at different radial locations

5.4 Swell Structure and Vorticity transport analysis

THE vorticity transport analysis was also carried out for the slices from $r/R \in [0.27,\ 0.7]$, and the result is plotted in Fig. 5.13. The vorticity convection term $v\partial\omega_y/\partial y$ and vorticity tilting term $\omega_x\partial v/\partial x+\omega_z\partial v/\partial z$ cross each other at around $r/R = 0.326$, which corresponds to the central point of the swell structure as defined in previous chapter. To the root side of this cross-section, the convection term plays as a source, and vorticity tilting acts as the sink, balancing the leading edge vortex. To the tip side of this cross-section, the vorticity tilting plays as a source and the convection term acts as a

sink. Out of the swell structure region, the convection term mainly act as a sink, that balances the planer variation of the LEV circulation.

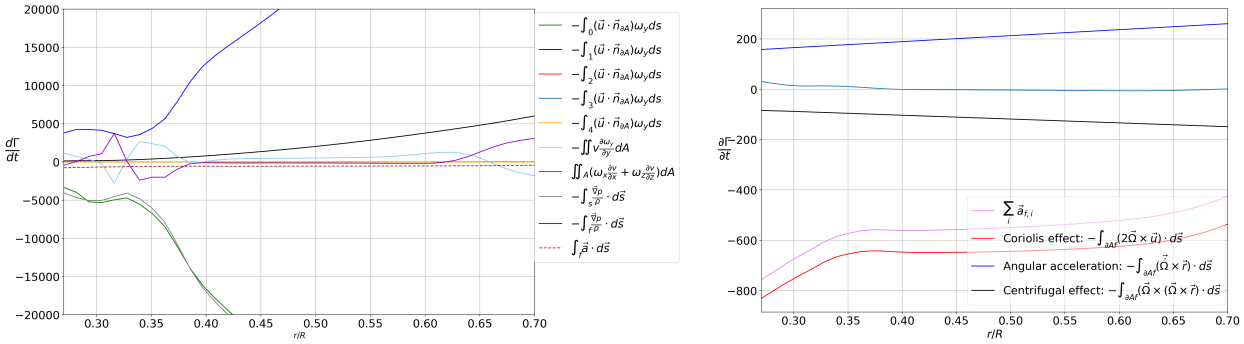

(a) (b)

Figure 5.13: Vorticity transport analysis around the swell structure between $r/R \in [0.27,\ 0.7]$, at azimuth angle $\Psi = 285°$. (a) Analysis result of the control areas as described in Fig. 3.15; (b) Acceleration components.

The swell structure, or the coherent vortical structure is the result of the vorticity tilting and vorticity convection in the radial direction. The convection term is also important in that at some radial locations, to the root side, $\dot{\Gamma}_{convection}$ is negative while to the tip side, it becomes positive. The curves show a similar trend when $r/R > 0.65$, where the leading edge vortex lifts off from the surface. This should be a common character of the three-dimensional LEV.

Another interesting point is the value of acceleration term $\mathbf{a}_{fluid}$, which is negative in the region $0.25 < r/R < 0.70$, even at the places where the LEV remain attached. This affirms the hypothesis that the blade-tip orienting span-wise component of the free stream has a direct relation with the negative Coriolis term. The value of $\mathbf{a}_{Cor}$, as well as the summation of all acceleration components, is larger at the root region as shown in Fig. 5.13(b). It is a reasonable assumption that the Coriolis term is a major source for the generation of the swell structure at root.

5.5 Error sources in the vorticity transport analysis

THE vorticity transport analysis is aimed to qualitatively understand how the rotating system affects the dynamic stall process. The reconstruction (the split and summation of different terms derived from Naiver-Stokes equation) of the change rate of the circulation in the control volume doesn't align 100% with the direct time differentiation of the circulation. In order to provide data-base for lower-order models, it is very important to understand where this difference comes from, and the experimental data can then be used and processed for the modelling of lower-order models for dynamic stall on a rotating system.

The dominant effects leading to this deviation are:

- The extreme large value of ω_y at shear layer is the main source of the error. Due to the difference between the line to extract data and the normal direction, which is the growth direction of the numerical grid, the interpolation introduces the error. The former is starting from a cell 7×10^{-7}m, and our extracting line to extract the data has an interval of 0.67×10^{-7}m. Although the interval is small enough to resolve the extreme value on the line, bound 1 is not the normal direction.

- Another error comes from the reconstruction of the vorticity field by the post-processing algorithm, by comparing the rotational component written by DLR-TAU output and the reconstructed vorticity field has a difference, especially the extreme values in the shear layer.[show the compare]

- The numerical method for line integral is another source of error. The pressure gradient term:

$$\int_{bound\ n} \frac{\nabla \mathbf{p}}{\rho} \cdot \mathrm{d}\mathbf{s} = \sum_i \left\{ \left[\frac{1}{\rho_0} \left(\frac{\partial p}{\partial x} \right)_0 + \frac{1}{\rho_1} \left(\frac{\partial p}{\partial x} \right)_1 \right] \frac{\Delta x_i}{2} + \left[\frac{1}{\rho_0} \left(\frac{\partial p}{\partial z} \right)_0 + \frac{1}{\rho_1} \left(\frac{\partial p}{\partial z} \right)_1 \right] \frac{\Delta z_i}{2} \right\}$$

  where the subscripts $_0$, $_1$ denote the two end points of the segment of i. And the planar convection term:

$$\int_{bound\ n} (\mathbf{u} \cdot \mathbf{n}_{\partial A}) \omega_y \mathrm{d}s = \sum_i \left[\frac{u_0 + u_1}{2} n_{x,i} + \frac{w_0 + w_1}{2} n_{z,i} \right] \frac{(\omega_{y0} + \omega_{y1})}{2} \sqrt{\Delta x_i^2 + \Delta z_i^2}$$

  since at bound 0 and bound 1, the ω_y gradients are very large, we used the mid value of the vorticity ω_y to estimate the planar convection terms.

5.6 Improvement of lower-order modelling for blades under high loads

As is shown in this chapter, the source of the circulation on a three-dimensional rotating system include mainly 2 parts:

- The combined effect of span-wise convection and the vorticity tilting;

- The Coriolis acceleration introduced “sink” and “source”.

The two aspects cover the “swell structure” mentioned in Chapter 4. In theory, there is no need to model another vortex that grows inboard and moves outboard. The first part can be modelled with the correlation that is set up in section 5.1, and the second part, Coriolis effect needs more data for modelling. Further consideration is then the modelling of the span-wise flow velocity.

6 Conclusions and outlook

6.1 The contribution of the current thesis

With the aim to further understand the three dimensional dynamic stall event on a relatively simply blade, the numerical experiment of a single rotating blade is designed to have a rectangular/untwisted geometry. The blade is set to 0 tilt angle and placed in the free stream with a $0.2U_{tip}$ velocity. The collective and cyclic pitch controls are selected such that the dynamic stall takes place on the rotating blade in the fourth quadrant of the revolution. The pitch controls are based on the result of the comprehensive analysis tool CAMRAD II. The numerical investigation of the dynamic stall on a rotating blade is mainly based on the result of Spalart-Allmaras turbulence model, with brief comparison with the result of $k-\omega$ turbulence model.

The time history of the sectional force C_n and moment C_m are examined on each radial location, and the vortex structures on the rotating blade are examined. Several important features that are yet not reported in previous research can be concluded as:

1. A strong interaction of the DSV and the tip vortex is observed and described in detail for this case. Contrary to observations of a pitching wing, the LEV on a rotating pitching blade is not pinned by the presence of the tip vortex, but rather the shedded DSV drastically interacts with the tip vortex, yielding a pair of counter rotating vortices in the near wake; the slices also indicate a diffused tip vortex in the near wake, whether this diffusion is caused by the pure pitch-down effect as observed for the pitching wing or if it is further diffused by the interaction of the tip vortex is not yet clear.

2. Despite an Ω-shaped vortex outboard, a swell vortex structure is observed to generate mostly inboard and to move outboard while gaining vorticity and size, which plays an important role after the shedding of the first DSV.

3. The presence of the swell structure is an outcome of the Ro effect inboard, similar to the low Re counterparts. The Coriolis force is comparable at the blade root to the pressure force, and hence is reasonable to be the main cause. The onset mechanism of the swell structure is proposed to be the effect of a stronger Coriolis force in x- and z-direction at the root region.

4. By tracing the vortex cores over the suction side of the blade, it is proposed to use a quasi-uniform-acceleration movement to describe the position of the swell structure, and the parameters were given for this special case.

5. By comparing the force coefficients on an outboard radial location with pitching airfoil, it is shown that unique vortical structures exist in the vicinity of the blade surface in the 3D Rotating cases and the detachment of the leading-edge vortex is postponed on the blade section. The difference of the detaching angle of attack is as much as 8 deg, which cannot be explained by the induced velocity field of the rotating environment predicted by linear inflow model.

6. By integrating the counter-clockwise rotating vorticity above the upper surface of the pitching airfoil and blade section, it is shown that there is a stronger dynamic stall vortex that magnified both the normal force and the moment, and a stronger circulation in the recovery stage for the 2D simulation.

The separation points of one revolution of the rotating blade are carefully examined. The criteria to determine the separation locations on the blade surface are discussed, two different methods, namely shape factor and c_f, are compared, and the separation types are recognised with the latter criterion. Different from previous papers, the current case shows mainly flow separation starting from the leading edge separation, or the shock-induced separation, while separation starting from the trailing edge is not observed.

Besides the conventional analysis, vorticity transport analysis is carried out for a planar control volume at three different radial locations, $r/R = 0.785$, 0.898 and .0928. This analysis method was previously employed to analyse the unsteady bio-aerodynamics, which includes the rotating and pitching of wings. And the current thesis implements this method on the analysis of the dynamic stall event on a rotating blade at high Re and M number, and the hypotheses of the rotation effect are confirmed:

1. With increasing r/R, the increasing compressibility effect is associated with a decreasing strength of leading edge vortex.

2. The span-wise convection of vorticity comes along with vorticity tilting from the other two dimensions, and the correlation between the two terms are presented with linear regression model in this dissertation, $\dot{\Gamma}_{tilting} = k\dot{\Gamma}_{convection} + C$. The linear regression model parameters vary with radial locations, with the symmetry plane of the Ω-typed vortex as the boundary. Inboard of the boundary, the linear slope k ($k < 0$) decreases, or the vorticity tilting is more dominating than the convection; and outboard of the boundary, the slope ($k < 0$) increases, or the vorticity convection is more dominating than the vorticity tilting.

3. The combined effect of span-wise convection of vorticity and the vorticity tilting in the current case show an unstable-source for the leading-edge vortex. The summation of the two terms serve as a "source" for the LEV for the three selected radial locations before the detachment of the LEV. But it seems to stabilise the circulation after the shedding of the DSV, resulting in a relatively weaker secondary vortex compared to the 2-dimensional case.

4. The main rotating effect is the Coriolis effect, which has a dominant value comparing with other two terms: centrifugal effect and angular acceleration. Before

the shedding of LEV, this Coriolis acceleration acts as a "sink" for the LEV, or it stabilises the vorticity that is entrained into the LEV. After the dynamic stall onset, this term becomes a "source" of the LEV, which seems to balance the circulation in the control volume after the shedding of the LEV. It is hence concluded the Coriolis effect plays a stabilisation role throughout the revolution of dynamic stall event.

5. The mechanism of Coriolis effect is discussed, that is the presence of the span-wise flow and the "sink" and "source" created by its normal gradient. This term does not show drastic variation along the radial location.

6. The difference of 2D and 3DR case lies mainly in the span-wise convection & vorticity tilting, as well as the Coriolis effect. The different time histories of the pressure gradient term of the vorticity transport equation in the 2D and 3DR cases indicate the difference in the vortex systems for both cases.

6.2 On the improvement of a lower-order model and outlook for experiment

Two additional terms can be added into the popular Blade-Element-Method and the 2D semi-empirical dynamic stall model.

1. The span-wise convection and vorticity tilting terms can be modelled as: 1) $\dot{\Gamma}_{convection} = -\bar{v}\partial\Gamma/\partial y$, and 2) $\dot{\Gamma}_{tilting} = k\dot{\Gamma}_{convection} + C$, in which $v(y)$, $k(y)$ and $C(y)$ need to be modelled further.

2. The Coriolis effect created "sink" need to be modelled, $\dot{\Gamma}_{Coriolis} = g(v)$. Other rotational acceleration terms can be estimated with Eq. 3.32 and Eq. 3.33 for each radial location.

Based on the preliminary numerical investigation on the single rotating blade in this thesis, experiments on the rotating blade can focus on the following aspects:

1. Pressure sensors can be placed at the radial locations $r/R = 0.898$ (where the symmetric plane of the Ω-typed vortex lies), $r/R = 0.7$ (where the most drastic moment stall occurs), $r/R = 0.928$ (where only slight stall takes place). These experiment data can then be used as standard data to calibrate turbulence models, mesh, and lower-order models.

2. Experiment with Stereo Particle-Image Velocimetry for y planes can focus on the topology of the vortex at these locations, and the one for x planes can focus on the span-wise velocity. The correlation of the velocity fields can then be post-processed to carry out the vorticity transport analysis, and utilised for lower-order models.

Further experiment research or numerical simulation can further extend to two-bladed rotor, blades with twist, blades with different platform geometries, as well as tip vortex

induced stall. Vorticity transport analysis is a powerful method to understand the mechanism of the revolution of the vortex system, and it is also worth of implemented on these issues. With more accumulated data, the lower-order model can also be improved.

6.3 On the control of dynamic stall on helicopter blades

At last but not the least, on the control of dynamic stall on helicopter blades, methods that changes the normal gradients of the span-wise flow can be also investigated. As is discussed in the previous chapter, the Coriolis acceleration has a stabilisation effect on the vortex system by altering the normal gradient of the span-wise relative flow. As a result, changing the flow structure in the span-wise direction can also has a potential to control dynamic stall on the helicopter blades, in addition to the popular investigations that focus on the chord-wise flow. The methods include modifying blade twists, active momentum flow in the span-wise direction and so on.

Bibliography

[1] Kufeld, R. M., Bousman, W. G. High load conditions measured on a UH-60A in manoeuvring flight. *Journal of the American Helicopter Society*, *43*(3), pp 202–211, 1998.

[2] National Transportation Safety Board, Aviation Accident Factual Report, LAX99LA047. https://app.ntsb.gov/pdfgenerator/ReportGeneratorFile.ashx?EventID=20001211X11580&AKey=1&RType=Factual&IType=LA

[3] Leishman, J. Gordon, T. S. Beddoes. A Semi-Empirical model for dynamic stall. *Journal of the American Helicopter society*, 1989; *34*(3), pp: 3–17.

[4] McAlister, K.W., Lambert, O., Petot, D. Application of the ONERA model of dynamic stall. *NASA Technical Paper 2399*. Aeromechanics Laboratory, U.S. Army Research and Technology Laboratories, AVSCOM, USA. Nov 1984.

[5] Peters D.A. Towards a unified lift model for use in rotor blade stability analyses. *Proceedings of the 40th Annual Forum of the American Helicopter Society*, Arlington, VA, May 1984; 525–538.

[6] Petot D. An investigation of stall on a 4.2 m diameter experimental rotor. In *The Seventh International Workshop on Dynamics and Aeroelastic Modeling of Rotorcraft Systems*. U.S. Army Research Office and Washington University in St. Louis: St. Louis, 1997; 1–17, MO (14161997)

[7] Larsen J.W, Nielsen S.R.K, Krenk S. Dynamic stall model for wind turbine airfoils. Journal of Fluids and Structures, 2007; *23*, pp 959–982.

[8] Hansen M.H, Guanaa M, Madsen H.A. A Beddoes-Leishman type dynamic stall model in state-space and indicial formulations. *Technical Report Risø-R-1354(EN)*, Risø National Laboratory, Roskilde, Denmark, June 2004.

[9] Sheng, W, Galbraith R.A, Coton F.N. A modified dynamic stall model for low Mach numbers. *Journal of Solar Energy Engineering*, 2008; *130*(3), pp: 1–10.

[10] Johnson, W. CAMRAD II, Comprehensive Analytical Model of Rotorcraft Aerodynamics and Dynamics. Release 4.9, Johnson Aeronautics, Palo Alto, CA, USA. 2012

[11] Ngyen, K; Johnson, W. Evaluation of dynamic stall models with UH-60A airloads flight test data. In: *Annual forum proceedings-American helicopter society*. American Helicopter Society, 1998. *54*, pp: 576–588.

[12] Truong, K. V. Modeling aerodynamics, including dynamic stall, for comprehensive analysis of helicopter rotors. *Aerospace*, 2017; *4*(2), pp: 1–24.

[13] https://esut.de/wp-content/uploads/2019/10/NH90-Sea-Lion-1068x712.jpg

[14] Gerontakos, P. An experimental investigation of flow over an oscillating airfoil (Master's thesis), 2004. McGill University, Montreal, Quebec, Canada. Retrieved from https://central.bac-lac.gc.ca/.item?id=TC-QMM-80014&op=pdf&app=Library&oclc_number=891952257

[15] McCroskey, W. J., Carr, L.W., McAlister, K. W. Dynamic stall experiments on oscillating airfoils. *AIAA Journal*, 1978. *14*1, pp: 57–63.

[16] McCroskey, W. J., McAlister, K.W., Carr, L.W. Dynamic stall on advanced airfoil sections. *Proceedings of 36th annual forum of the American Helicopter Society*, Washington D.C., May, 1980. *80*(1), pp: 1–25. Available at https://apps.dtic.mil/sti/pdfs/ADA085809.pdf

[17] McAlister, K. W., Carr, L. W., McCroskey, W. J. Dynamic stall experiments on the NACA 0012 airfoil. *NASA Technical Paper 1100*, Ames Research Center, Moffet Field, CA, USA. January, 1978. Available at https://ntrs.nasa.gov/api/citations/19780009057/downloads/19780009057.pdf.

[18] McCroskey, W. J., McAlister, K. W., Carr, L. W., Pucci, S. L. An Experimental Study of Dynamic Stall on Advanced Airfoil Sections. Volume I. *NASA Technical Memorandum 84245*, Ames Research Center, Moffet Field, CA, USA. July, 1982. Available at https://apps.dtic.mil/sti/pdfs/ADA119827.pdf

[19] St. Hilaire, A. O., Carta F.O., Fink, M. R., Jepson, W. D. The Influence of Sweep on the Aerodynamic Loading of an Oscillating NACA 0012 Airfoil. Volume I. Technical Report. *NASA Contractor Report 3092*, United Technologies Research Center, East Hartford, CT, USA. May, 1979. Available at https://core.ac.uk/download/pdf/42870061.pdf.

[20] McCroskey, W. J., Fisher, R. K. Detailed Aerodynamic Measurements on a Model Rotor in the Blade Stall Regime. *Journal of the American Helicopter Society*,1972. *17*(1), pp: 20–30.

[21] Liiva, J., Davenport, F. J. Dynamic Stall of Airfoil Sections for High?Speed Rotors. *Journal of the American Helicopter Society*, 1969. *14*(2), pp: 26–33.

[22] Ericsson, L. E., Reding, J. P. Dynamic stall of helicopter blades. *Journal of the American Helicopter Society*,1972. *17*(1), pp: 11–19.

[23] McCroskey, W. J. Unsteady airfoils. *Annual review of fluid mechanics*, 1982. *14*(1), pp: 285–311.

[24] Young, W. H. Fluid-mechanics mechanisms in the stall process of airfoils for helicopters. In *Numerical and Physical Aspects of Aerodynamic Flows*, 1982. *5*, pp: 601–615. Springer, Berlin, Heidelberg.

[25] Johnson, W., Ham, N. D. On the mechanism of dynamic stall. *Journal of the American Helicopter Society*, 1972 *17*(4), pp: 36–45.

[26] Martin, J. M., Empey, R. W., McCroskey, W. J., Caradonna, F. X. An experimental analysis of dynamic stall on an oscillating airfoil. *Journal of the American Helicopter Society*, 1974. *19*(1), pp: 26–32.

[27] McCroskey, W. J.The phenomenon of dynamic stall. *NASA Technical Memorandum 81264*. Aeromechanics Laboratory, AVRADCOM Research and Technology Laboratories, Ames Research Center, Moffett Field, CA, USA. March 1981. Available at https://apps.dtic.mil/sti/pdfs/ADA098191.pdf

[28] Carr, L. W. Progress in analysis and prediction of dynamic stall. *Journal of aircraft*, 1988; *25*(1), pp 6–17. Available at https://www.academia.edu/download/56798544/Progress_in_Analyses_and_Prediction_of_Dynamic_stall-carr1988.pdf

[29] Reynolds, W. C., Carr, L. W. Review of unsteady, driven, separated flows. In proceeding of *Shear Flow Control Conference*, March, 1985. Boulder, CO, USA

[30] Doligalski, T. L., Smith, C. R., Walker, J. D. A. Vortex interactions with walls. *Annual Review of Fluid Mechanics*, 1994. *26*(1), pp: 573–616.

[31] Acharya, M., Metwally, M. H. Unsteady pressure field and vorticity production over a pitching airfoil. *AIAA journal*, 1992. *30*(2), pp: 403–411.

[32] Smith, F. T. Finite?time break?up can occur in any unsteady interacting boundary layer. *Mathematika*,1988,*35*(2), pp: 256–273.

[33] Conlisk, A. The pressure field in intense vortex-boundary layer interaction. In *27th Aerospace Sciences Meeting*, January, 1989. Reno, Nevada, USA.

[34] Peridier, V. J., Smith, F. T., Walker, J. D. A. Vortex-induced boundary-layer separation. Part 2. Unsteady interacting boundary-layer theory. *Journal of Fluid Mechanics*, 1991, *232*, pp: 133–165.

[35] Metwally, M. H. Investigation and control of the unsteady flow field over a pitching airfoil (Doctoral dissertation), 1990. Illinois Institute of Technology.

[36] Karim, M. A. Experimental investigation of the formation and control of the dynamic-stall vortex over a pitching airfoil (Doctoral dissertation), 1992. Illinois Institute of Technology.

[37] Sommerfeld, A. *Mechanics of deformable bodies: Lectures on theoretical physics*, 2016. *2*. Elsevier.

[38] Wu, J. C. *Elements of vorticity aerodynamics.* Springer Berlin Heidelberg, 2018.

[39] Bowles, P. O. Wind tunnel experiments on the effect of compressibility on the attributes of dynamic stall (Doctorol dissertation), March 2012. University of Notre Dame, IN, USA. Retrieved from https://search.proquest.com/openview/75697ddfc2b4acd7069abfb140c46be2/1?pq-origsite=gscholar&cbl=18750&diss=y

[40] Sankar N. L., Tassa Y. Compressibility Effects on Dynamic Stall of an NACA 0012 Airfoil. *AIAA Journal*, 1981. *19*(5), pp: 557–558.

[41] Chandrasekhara M. S., Carr L. W., Wilder M. C. Interferometric investigations of compressible dynamic stall over a transiently pitching airfoil. *AIAA journal*, 1994. *32*(3), pp: 586–593.

[42] Carr L. W., Chandrasekhara M. S. Compressibility effects on dynamic stall. *Progress in Aerospace Sciences*, 1996. *32*(6), pp: 523–573.

[43] Gupta, R., Ansell, P. J. Investigation of the effects of Reynolds number on the unsteady flow physics of airfoil dynamic stall. In *2018 AIAA Aerospace Sciences Meeting*, Kissimmee, FL, USA. January 2018.

[44] Carta, F. O. A comparison of the pitching and plunging response of an oscillating airfoil. *NASA Contractor Report 3172*. United Technologies Research Center, East Harford, CT, USA. October, 1979.

[45] J.G. Leishman. *Principles of Helicopter Aerodynamics*. Cambridge Aerospace Series, Cambridge Univ. Press, New York, 2006.

[46] Visbal, M. R., Garmann, D. J. Comparison of pitch versus plunge maneuvers of a finite wing. In *AIAA Aviation 2019 Forum*, Dallas, TX, USA. June 2019. 3334, pp: 1–17.

[47] Gharali, K., Johnson, D. A. Dynamic stall simulation of a pitching airfoil under unsteady freestream velocity. *Journal of Fluids and Structures*, 2013. *42*, pp: 228–244.

[48] Wang, Q., Zhao, Q. Unsteady aerodynamic characteristics investigation of rotor airfoil under variational freestream velocity. *Aerospace Science and Technology*, 2016. *58*, pp: 82–91.

[49] Wen, G., Gross, A. Numerical Investigation of Deep Dynamic Stall for a Helicopter Blade Section. *AIAA Journal*, 2019. *57*(4), pp: 1434–1451.

[50] Raghav V., Komerath N. An exploration of radial flow on a rotating blade in retreating blade stall. *Journal of the American Helicopter Society*, *58*(2), pp: 1–10.

[51] Raghav, V.; Komerath, N. Velocity measurements on a retreating blade in dynamic stall. *Experiment of Fluids* , 2014, *55*, 1669.

[52] Gibertini G., Mencarelli A., Zanotti A. Oscillating aerofoil and perpendicular vortex interaction. *Proceefdings of the Institution of Mechanical Engineers, Part G: Journal of Aerospace Engineering*, 2014. *228*(6), pp: 846–858.

[53] Chaderjian N. M. Navier-Stokes simulation of UH-60A rotor/wake interaction using adaptive mesh refinement. *In Proceedings of the 73rd Annual Forum of the American Helicopter Society*. NASA Ames Research Center Moffet Field, CA, USA. May 2017. Available at https://core.ac.uk/download/pdf/141519767.pdf

[54] Leishman, J.G. *Principles of Helicopter Aerodynamics*; Cambridge University Press: New York, NY, USA, 2006; p. 158–160.

[55] He, C.J. *Development and application of a generalized dynamic wake theory for lifting rotors*. Doctor thesis, Georgia Institute of Technology, 1989.

[56] Peters, D.A., He, C.J. Finite state induced flow models, Part II: Three-dimensional rotor disk. *Journal of Aircraft*, 1995.*32*(2), pp: 323–333.

[57] Yang, Z., Sankar, L.N., Smith, M. J., Bauchau, O. Recent improvements to a hybrid method for rotors in forward flight. *Journal of Aircrft*, 2002.*39* (5), pp: 804–812.

[58] Komerath, N. M., Schreiber, O. A. Implementation and validation of a wake model for low-speed forward flight. *NASA Technique report*. Sep. 1987.

[59] Chen, R., Yuan, Y., Thomson, D. A review of mathematical modelling techniques for advanced rotorcraft configurations.*Progress in Aerospace Sciences*, 2021.*120*, pp: 1–18.

[60] Theodorsen, T., Mutchler, W. General theory of aerodynamic instability and the mechanism of flutter. 1935.

[61] Van der Wall, B. G., Leishman, J. G. The influence of variable flow velocity on unsteady airfoil behaviour. *18th European Rotorcraft Forum*, Sep. 1992. Avignon, France.

[62] Jose, A. I., Leishman, J. G., Baeder, J. D. Unsteady Aerodynamic Modeling with Time Varying Free Stream Mach Numbers. *Journal of the American Helicopter Society*, 2006. *51* (4), pp: 299–318.

[63] Leishman, J. G. Rotorcraft aerodynamics. *Encyclopedia of Aerospace Engineering*, 2010. pp: 1–15

[64] Leishman, J. G, Beddoes, T.S. A Semi-Empirical model for dynamic stall. *Journal of the American Helicopter society* 1989, *34*(3), pp: 3–17

[65] Leishman, J. G. State-space model for unsteady airfoil behavior and dynamic stall. In *30th Structures, Structural Dynamics and Materials Conference*, 1989, April. pp. 1319.

[66] Thwaites, B. *Incompressible Aerodynamics*, Oxford University Clarendon Press, 1960.

[67] Woods, L.C. *The Theory of Subsonic Plane Flow*, Cambridge University Press, 1961.

[68] Harris, C.D. Two-dimensional aerodynamic characteristics of the NACA 0012 airfoil in the Langley 8 foot transonic pressure tunnel. *Technical Memorandum 19810014503* 198. NASA Langley Research Center Hampton, VA, United States

[69] Ellington, C. P., Van Den Berg, C., Willmott, A. P., Thomas, A. L. Leading-edge vortices in insect flight. *Nature*, 1996. *384*(6610), pp: 626–630.

[70] Lee, M., Ho, C. M. Lift force of delta wings. *Appl Mech Rev*, 1990. *43* 9, pp: 209–221

[71] Gardner, A. D., Merz, C. B., Wolf, C. C. Effect of sweep on a pitching finite wing. *Journal of the American Helicopter Society*, 2019. *64*(3), pp: 1–13.

[72] Beem, H. R., Rival, D. E., Triantafyllou, M. S. On the stabilization of leading-edge vortices with spanwise flow. *Experiments in fluids*, 2012, *52*(2), pp 511–517.

[73] Wong, J. G., Rival, D. E. Determining the relative stability of leading-edge vortices on nominally two-dimensional flapping profiles. *Journal of Fluid Mechanics*, 2015, *766*, pp: 611– 625

[74] Garmann, D., Visbal, M. Three-Dimensional Flow Structure and Aerodynamic Loading on a Low Aspect Ratio, Revolving Wing. *42nd AIAA Fluid Dynamics Conference and Exhibit.*, June, 2012. New Orleans, Louisana, USA.

[75] Wojcik, C. J., Buchholz, J. H. Vorticity transport in the leading-edge vortex on a rotating blade. *Journal of Fluid Mechanics*, 2014. *743*, pp 249–261

[76] Carr, Z. R., DeVoria, A. C., Ringuette, M. J. Aspect-ratio effects on rotating wings: circulation and forces. *Journal of Fluid Mechanics*, 2015. *767*, pp: 497–525.

[77] Lee, Y. J., Lua, K. B., Lim, T. T. Aspect ratio effects on revolving wings with Rossby number consideration. *Bioinspiration and biomimetics*, 2016. *11*(5), 056013.

[78] Smith, D. T., Rockwell, D., Sheridan, J., Thompson, M. Effect of radius of gyration on a wing rotating at low Reynolds number: a computational study. *Physical Review Fluids*, 2017. *2*(6), 064701, pp: 1–23.

[79] Jardin, T., David, L. Coriolis effects enhance lift on revolving wings. *Physical Review E*, 2015. *91*(3), pp 1–4. Available at https://hal.archives-ouvertes.fr/hal-01131328/document

[80] Jardin, T. Coriolis effect and the attachment of the leading edge vortex. *Journal of Fluid Mechanics*, 2017. *820*, pp: 312–340.

[81] Wu J.Z., Wu J. M. Vorticity dynamics on boundaries. *Advanced in applied mechanics*, 1996. *32*, pp: 119–275.

[82] Panah, A. E.,Akkala, J.M., Buchholz, J.H.J. Vorticity transport and the leading-edge vortex of a plunging airfoil. *Exp. Fluids*, 2015. 56, 160, pp: 1–15.

[83] Buchholz, J. H., Thurow, B. S., Wabick, K. J., Johnson, K. C., Berdon, R. J. L. Three-dimensional Vortex Dynamics in Unsteady, Separated Flows. Report. March, 2019. The University of Iowa Iowa City United States. Available at https://apps.dtic.mil/sti/pdfs/AD1097229.pdf

[84] Piziali, R. A. 2-D and 3-D oscillating wing aerodynamics for a range of angles of attack including stall. *NASA Technical Memorandum 4632*, Ames Research Center, Moffet Field, CA, USA. September, 1994.

[85] Schreck, S. J., Hellin, H. E. Unsteady vortex dynamics and surface pressure topologies on a finite pitching wing. *Journal of Aircraft*, 1994.*31*(4), pp: 899–907.

[86] Tang, D. M., Dowell, E. H. Experimental investigation of three-dimensional dynamic stall model oscillating in pitch. *Journal of aircraft*, 1995, *32*(5), pp: 1062–1071.

[87] Coton, F. N., Galbraith, R. M. An experimental study of dynamic stall on a finite wing. *The Aeronautical Journal*, 1999.*103*(1023), pp: 229–236.

[88] Szafruga, J., Ramaprian, B., Szafruga, J., Ramaprian, B. LDA measurements in the three-dimensional flow over an oscillating rectangular wing. In *28th Fluid Dynamics Conference*, 1997. pp. 1935–1946.

[89] Le Pape, A., Pailhas, G., David, F., Deluc, J. M. Extensive wind tunnel tests measurements of dynamic stall phenomenon for the OA209 airfoil including 3D effects. 2007. Available at https://dspace-erf.nlr.nl/xmlui/bitstream/handle/20.500.11881/204/Extensive%20wind%20tunnel%20tests%20measurements%20.PDF?sequence=1

[90] Bross, M., Rockwell, D. Flow structure on a simultaneously pitching and rotating wing. *Journal of fluid mechanics*, 2014.*756*, pp: 354–383.

[91] DiOttavio, J., Watson, K., Cormey, J., Kondor, S., Komerath, N. Discrete structures in the radial flow over a rotor blade in dynamic stall. In *26th AIAA Applied Aerodynamics Conference*, August, 2008. Honolulu, Hawaii, USA. 7344, pp: 1–10.

[92] Raghav, V., Komerath, N. Dynamic Stall Life Cycle on a Rotating Blade in Steady Forward Flight. *Journal of the American Helicopter Society*, 2015. *60*(3), pp:1–12.

[93] Mulleners, K., Kindler, K., Raffel, M. Dynamic stall on a fully equipped helicopter model. *Aerospace Science and Technology*, 2012.*19*(1), pp: 72–76. Available at https://core.ac.uk/download/pdf/30993227.pdf

[94] Gardner, A. D., Richter, K. Influence of rotation on dynamic stall. *Journal of the American Helicopter Society*, 2013. *58*(3), pp 1–9.

[95] Letzgus, J., Keßler, M., Krämer, E. CFD-simulation of three-dimensional dynamic stall on a rotor with cyclic pitch control. In Proceedings of *41st European Rotorcraft Forum*, September 2015. Munich, Germany. Available at https://dspace-erf.nlr.nl/xmlui/bitstream/handle/20.500.11881/3604/ERF2015_0093_paper.pdf?sequence=1&isAllowed=y.

[96] Schwermer, T., Gardner, A. D., Raffel, M. Dynamic stall experiments on a rotor with high cyclic setting in axial inflow. In *American Helicopter Society 73rd Annual Forum*, May, 2017. Fort Worth, Texas, USA. pp. 9-11.

[97] Letzgus, J., Gardner, A. D., Schwermer, T., Keßler, M., Krämer, E. Numerical investigations of dynamic stall on a rotor with cyclic pitch control. *Journal of the American Helicopter Society*, 2019. *64*(1), pp: 1–14.

[98] Richez, F. Analysis of dynamic stall mechanisms in helicopter rotor environment. *Journal of the American Helicopter Society*, 2018. *63*(2), pp: 1–11.

[99] Gibertini, G., Zanotti, A., Colli, A. Dynamic Stall Inducted by Blade Vortex Interaction in Helicopter. In *45th European Rotorcraft Forum*. September, 2019. Warsaw, Poland. pp. 1–5.

[100] Ruan, Y., Hajek, M. Numerical Investigation of Dynamic Stall on a Single Rotating Blade. *Aerospace, 2021. 8*(4), 90, pp: 1–27.

[101] Lee, J. B., Yee, K. J., Oh, S. J., Kim, D. H. Development of an unsteady aerodynamic analysis module for rotor comprehensive analysis code. *International journal of aeronautical and space sciences*, 2009. 10(2), pp: 23–33.

[102] Modarres, R. Semi-Empirical Modelling of Two-Dimensional and Three-Dimensional Dynamic Stall. Doctoral thesis, 2016, Washington University in St. Louis.

[103] Schwamborn, D., Gerhold, T., Kessler, R. DLR-TAU Code-an overview. *1st ONERA/DLR Aerospace Symposium*, Paris, 21.-24. June, 1999.

[104] Mavriplis, D. J., Jameson, A. Multigrid solution of the Navier-Stokes equations on triangular meshes. *AIAA journal*, 1990, *28*(8), pp: 1415–1425.

[105] Anderson, W. K., Bonhaus, D. L. An implicit upwind algorithm for computing turbulent flows on unstructured grids. *Computers & Fluids*, 1994, *23*(1), pp: 1–21.

[106] Haselbacher, A., Blazek, J. Accurate and efficient discretization of Navier-Stokes equations on mixed grids. *AIAA journal*, 2000, *38*(11), pp: 2094–2102.

[107] Edwards, J. R., Chandra, S. Comparison of eddy viscosity-transport turbulence models for three-dimensional, shock-separated flowfields. *AIAA journal*, 1996, *34*(4), pp: 756–763.

[108] Menter, F. Zonal two equation k-ω turbulence models for aerodynamic flows. In *23rd fluid dynamics, plasmadynamics, and lasers conference*, Orlando, FL, USA. July 1993. 93-2906. pp: 1–21.

[109] Menter, F. R. Two-equation eddy-viscosity turbulence models for engineering applications. *AIAA journal*, 1994, *32*(8), pp: 1598–1605.

[110] Menter, F. R., Kuntz, M., Langtry, R. Ten years of industrial experience with the SST turbulence model. *Turbulence, heat and mass transfer*, 2003, *4*(1), pp: 625–632. Available at https://cfd.spbstu.ru/agarbaruk/doc/2003_Menter,%20Kuntz,%20Langtry_Ten%20years%20of%20industrial%20experience%20with%20the%20SST%20turbulence%20model.pdf

[111] Steger, J.L., Dougherty, F.C., Benek, J.A. A chimera grid scheme, ASME mini-symposium on advances in grid generation, 1982.

[112] Benek, J., Buning, P., Steger, J. A 3-D chimera grid embedding technique. In *7th Computational Physics Conference*. July 1985. (p. 1523).

[113] Dougherty, f. c. Development of a chimera grid scheme with applications to unsteady problems. Ph.D Dissertation, Stanford University). October 1985.

[114] Cougherty, F. C., Benek, J. A., Steger, J. L. On applications of chimera grid schemes to store separation. 1985.

[115] Bonet, J., Peraire, J. An alternating digital tree (ADT) algorithm for 3D geometric searching and intersection problems. *International Journal for Numerical Methods in Engineering*, 1991. *31*(1), pp: 1–17.

[116] Madrane, A., Heinrich, R., Gerhold, T. (2002, October). Implementation of the chimera method in the unstructured hybrid DLR finite volume TAU-Code. In *6th Overset Composite Grid and Solution Technology Symposium*, Ft. Walton Beach, Florida, USA. Oct 2002. *8*(10).

[117] Madrane, A., Raichle, A., Stuermer, A. (2004). Parallel implementation of a dynamic unstructured chimera method in the DLR finite volume TAU-code. Canada: N. p., July 2004.

[118] Klimchenko, V., Sridharan, A., Baeder, J. D. CFD/CSD study of the aerodynamic interactions of a coaxial rotor in high-speed forward flight. In *35th AIAA Applied Aerodynamics Conference*.Denver, Colorado, USA. June 2017, 2017-4454, pp: 1–22.

[119] Pointwise, Inc (2020). Pointwise (18.3R2) *Software*. July 2020. Retrieved from https://https://www.pointwise.com/support/release-notes-V183R2.html

[120] Caradonna, F.X.; Tung, C. Experimental and Analytical Studies of a Model Helicopter Rotor in Hover. In *6th European Rotorcraft and Powered Lift Aircraft Forum*, Bristol, UK, 16–19 September 1980; pp. 25:1–25:19.

[121] Oberkampf, W.L.; Trucano, T.G. Verification and validation in computational fluid dynamics. *Progress in Aerospace Science* , 2002, *38* (3), pp: 209– 272.

[122] Haller, G. Exact theory of unsteady separation for two-dimensional flows. *Journal of Fluid Mechanics*, 2004, *512*, pp: 257–311.

[123] Castillo, L.; Wang, X.; George, W.K. Separation criterion for turbulent boundary layers via similarity analysis. *Journal of Fluids Engineering*, 2004, *126*, pp: 297–304.

[124] Tobak, M.; Peake, D.J. Topology of three-dimensional separated flows. *Annual Review of Fluid Mechanics*,1982, *14*, (1), pp: 61–85.

[125] Potter, M.C., Foss, J.F. *Fluid Mechanics.* Great Lakes Press, Inc., Okemos, MI, USA, 1982.

[126] Wu, J. Z., Wu, J. M. Interactions between a solid surface and a viscous compressible flow field.*Journal of Fluid Mechanics*, 1993.*254*, pp: 183–211.

[127] JCR, H., Wray, A., Moin, P. Eddies, stream, and convergence zones in turbulent flows. *Center for turbulence research report CTR-S88*, 1988. pp:193–208.

[128] Chong, M. S., Perry, A. E., Cantwell, B. J. A general classification of three?dimensional flow fields. *Physics of Fluids A: Fluid Dynamics*, 1990. *2*(5), pp:765–777.

[129] Anderson Jr, J. D. *Fundamentals of aerodynamics*, 2010. Tata McGraw-Hill Education.

[130] Kaufmann, K.; Costes, M.; Richez, F.; Gardner, A.D.; Pape, A.L. Numerical investigation of three-dimensional static and dynamic stall on a finite wing. *Vertical Flight Society* 2015, 60(3), pp: 1–12.

[131] Visbal, M.R.; Garmann, D.J. High-fidelity simulations of dynamic stall over a finite-aspect-ratio wing. In Proceedings of the *8th AIAA Flow Control Conference*, Washington, DC, USA, 13–17 June 2016; p. 4243.

[132] Sujudi, D.; Haimes, R. Identification of swirling flow in 3D vector fields. In Proceedings of the 12th Computational Fluid Dynamics Conference, San Diego,CA,USA, 19–22 June 1996; p. 1715

[133] Chang, J.W.; Park, S.O. Measurements in the tip vortex roll-up region of an oscillating wing. *AIAA Journal* 2000, *38*(6), pp:1092–1095.

[134] Ozen, C.A.; Rockwell, D. Three-dimensional vortex structure on a rotating wing. *Journal of Fluid Mechanics* 2012, *707*, pp: 541–550.

[135] Costes, M.; Richez, F.; Le Pape, A.; Gavériaux, R. Numerical investigation of three-dimensional effects during dynamic stall *Aerospace Science and Technology*, 2015, *47*, pp: 216–237.

[136] Avanzi, F. Analysis of Dynamic Stall on a Pitching Airfoil with Spectral Proper Orthogonal Decomposition. Master's Thesis, Universita Degli Studi Di Padova, Padova, Italy, 2019.

[137] Wolfinger, M., Rockwell, D. Flow structure on a rotating wing: effect of radius of gyration. *Journal of Fluid Mechanics*, 2014, *755*, pp: 83–110.

[138] Starikovskiy, A., Meehan, K., Persikov, N., Miles, R. Static and dynamic stall control by NS SDBD actuators. *Plasma Sources Science and Technology*, 2019. *28* (5), 054001.

[139] Singhal A.; Castaneda, D.; Webb, N.; Samimy M. Control of dynamic stall over a NACA 0015 airfoil using plasma actuators. *AIAA Journal*, *56*(1), pp: 78–89.